UC Berkeley
UC Berkeley Electronic Theses and Dissertations

Title
Ion Distribution Functions in the Near-Sun Solar Wind

Permalink
https://escholarship.org/uc/item/7dn1h4rs

Author
McManus, Michael

Publication Date
2022

Peer reviewed|Thesis/dissertation

Ion Distribution Functions in the Near-Sun Solar Wind

by

Michael Dermot McManus

A dissertation submitted in partial satisfaction of the

requirements for the degree of

Doctor of Philosophy

in

Physics

in the

Graduate Division

of the

University of California, Berkeley

Committee in charge:

Professor Stuart D. Bale, Chair
Dr Davin Larson
Professor Jonathan Wurtele
Professor Michael Manga

Fall 2022

Ion Distribution Functions in the Near-Sun Solar Wind

Abstract

Ion Distribution Functions in the Near-Sun Solar Wind

by

Michael Dermot McManus

Doctor of Philosophy in Physics

University of California, Berkeley

Professor Stuart D. Bale, Chair

Parker Solar Probe (PSP), launched in late 2018, is a mission designed to sample the near-Sun environment and solar corona, and answer broad open questions concerning coronal energy flow and solar wind dynamics. The SPAN-Ion instrument is an on-board electrostatic analyzer responsible for measuring 3D ion velocity distribution functions (VDFs). In the first part of this thesis, we give an overview of SPAN-Ion, its intrinsic uncertainties, and discuss the effect of its finite field-of-view on moment measurements. We then move on to study magnetic switchbacks, rapid radial reversals of the magnetic field. While their role in young solar wind dynamics and precise generation mechanisms are still unclear, their ubiquity marks them out as an important early PSP observation. Using MHD invariants to probe their macroscale structure, we show that they are localised S-shaped folds in the magnetic field with internally backward propagating Alfvénic fluctuations, which has important implications for studies of small-scale turbulence using such invariants. Using fits to SPAN-Ion data, we then investigate alpha particle density, abundance, and velocity fluctuations inside and outside individual switchbacks, showing that there are no consistent compositional changes inside vs outside, but argue that these findings cannot yet be used to definitively rule in favour of one particular switchback generation mechanism (although they may be able to in the future). We also show that alpha particle speeds may be enhanced, decreased, or remain constant during a switchback, depending on the relative values of the alpha proton drift and the local wave phase speed, in contrast to the always positive proton velocity spikes. In the final part we study the alpha VDFs in more detail, focussing on characterising secondary alpha populations or alpha "beams". These have been essentially unstudied relative to their proton beam counterparts. We find they are generally more dense and slower moving than proton beams, and occur less frequently. We report time localised correlations between proton and alpha normalised heat flux, suggesting the existence of a common mechanism for producing beams in each species. We then perform a case study of an ion scale wave event, showing for the first time an active role being played by the alphas, specifically the alpha beam population, in driving solar wind plasma unstable and

locally generating right-handed fast magnetosonic waves. The predicted wave frequencies, polarisations, and times of occurrence agree remarkably well with the observations. Such wave events are important for understanding the mechanisms of energy exchange between waves and particles that may be responsible for in-situ heating of the solar wind.

Contents

List of Figures

Chapter 1

Introduction

In 1958 Eugene Parker introduced an elegant model of the solar wind [133] which explained two seemingly conflicting ideas: 1) The fact that while dust tails of comets were well explained by the effects of gravity and radiation pressure, their gaseous tails always streamed away from the Sun rather than behind the comet and pointed to the existence of a constant corpuscular flux being emitted by the Sun, and 2) As pointed out by Chapman [33] in 1957, the very high electron thermal conductivity of the corona should mean that the Earth is constantly bathed in the static atmosphere of the Sun that extends far beyond Earth's orbit. Parker pointed out that a static model of the solar atmosphere could not be maintained by the low pressures of the interstellar medium, and, using an isothermal, steady, spherically symmetric model, showed that the solar wind accelerates outwards from sub-sonic to super-sonic speeds, driven by the temperature at the base of the corona. The temperature in the model needed to explain the solar wind densities and velocities observed at 1AU (measurements of which were rapidly becoming available in the early 60s) was very high, on the order of 10^6 K [132], over an order of magnitude greater than the temperature of the photosphere, the Sun's surface. This became known as the *coronal heating problem*. While there have of course been decades of refinements to Parker's original model and scores of theories put forward to explain how exactly the mechanical, convective energy beneath the Sun's surface is transferred up into the corona seemingly in violation of the second law of thermodynamics, this problem remains open and is the holy grail of solar physics.

1.1   The Parker Solar Probe Mission

Parker Solar Probe (PSP) [53] is a spacecraft launched on the 12th of August, 2018, designed to measure and study the near-Sun solar wind and, for the first time, make in situ measurements of the solar corona. Planned as a 7 year mission, PSP will complete 24 orbits of the Sun, using 7 Venus gravity assists to lower its perihelion distance from $35R_S$ in Encounter 1 down to $9.8R_S$ for the last three orbits. For comparison, the previous closest in situ solar wind measurements were made by the Helios 2 spacecraft [148], which reached a distance of

0.3 AU or approximately $64R_S$. PSP's orbit lies fairly close to the ecliptic plane, meaning it is not usually sampling fast wind from polar coronal holes, but rather wind from mid-latitude coronal holes, coronal hole extensions, streamer belt wind, as well as the heliospheric current sheet (HCS).

The mission has three overarching scientific goals, defined as [53]:

1. **Trace the flow of energy that heats the solar corona and accelerates the solar wind.**

2. **Determine the structure and dynamics of the plasma and magnetic fields at the sources of the solar wind.**

3. **Explore mechanisms that accelerate and transport energetic particles.**

Item 1 encompasses the coronal heating problem. Theories of coronal heating can broadly be categorised into those involving heating by various forms of wave dissipation, and heating via magnetic reconnection events, although other theories exist (the literature is vast, see [5] for an overview and [191, 134] for reviews). Item 1 is however more broad than just being a restatement of the coronal heating problem, it also includes tracing the energy flow that results in the large variety of non-thermal features seen in both the ion and electron solar wind velocity distribution functions (VDFs), and determining how these energy flows affect the properties of the solar wind in the heliosphere as a whole.

Item 2 is concerned with the *sources* of the solar wind. Traditionally the solar wind was considered divisible into "fast wind" and "slow wind", although current understanding is that these really refer to "fast wind-like" and "slow wind-like" properties, as wind speed is not really the distinguishing feature but rather quantities like Aflvénicity, inter-species drift speeds, temperature anisotropies, elemental compositions, collisionality, etc. PSP's close in situ measurements mean we are able to use Potential Field Source Surface (PFSS) models to map the spacecraft's connectivity back to the source surface, which, together with coronal imaging, allow us to link the properties of the observed wind to their source regions. In addition, PSP will be able to determine the inherent burstiness/intermittency of the various solar wind sources, something that is not able to be done at 1AU because any temporal and spatial features have been washed out and are unable to be resolved.

Finally, item 3 is concerned with solar energetic particles (SEPs). There are two main classes of SEP events. Large scale, gradual events achieve particle energisation and acceleration via shocks generated by coronal mass ejections (CMEs), and are broad in longitudinal extent. Short, impulsive events are associated with magnetic reconnection in solar flares, and are narrowly extended in longitude. Again, simply by virtue of being much closer, PSP is able to far better spatially resolve the origin sites of SEP events, as particle scattering, cross-field diffusion, and multiple origin sites all conspire to make SEP events at 1AU difficult to interpret. In addition, PSP aims to shed light on the origin of the *seed* populations of high energy particles, the "suprathermal tails" that are seen universally in all different wind types (even away from any shocks), and in all ion species [61, 37, 51].

1.1.1 Instruments

The four instrument suites on board PSP to allow it to achieve its science objectives outlined above are:

- **FIELDS**: The FIELDS instrument suite [14] consists of two fluxgate magnetometers, one search coil magnetometer, and 5 electric antennas, which are together capable of measuring electric and magnetic fields, electron plasma density, spacecraft potential, and radio emissions.

- **ISOIS**: *Integrated Science Investigation of the Sun* [120] consists of two high energy particle instruments EPI-Lo and EPI-Hi capable of measuring energetic protons, electrons, and heavy ions, over a (combined) energy range of 20 keV - 200 MeV for ions and 25 keV - 6 MeV for electrons.

- **WISPR**: *Wide field imager for Parker Solar Probe* [175] is a white light telescope for imaging the solar corona and inner heliosphere.

- **SWEAP**: *Solar Wind Electrons, Alphas and Protons Investigation* [84] consists of a Faraday cup - Solar Probe Cup (SPC) [31] for measuring protons and alphas, two electrostatic analysers SPAN-A/B for electrons [179], and SPAN-Ion for protons, alphas, and heavier ions [101].

Given the extreme environments PSP experiences during its encounters, the body of the spacecraft and the instruments (except for the FIELDS antennas and SPC) lie in the umbra of the Thermal Protection Shield (TPS), a 4.5 inch thick carbon-carbon composite shield designed to withstand temperatures up to about 1400 degrees Celsius. While the temperature of the corona reaches millions of degrees, the very low densities (~ 1000 cm^{-3}) mean that the TPS only needs to withstand temperatures in the thousands. During its encounters, PSP experiences an irradiance from the Sun up to 475 times greater than that at Earth, energetic particles impinging on the spacecraft causing radiation damage, and is immersed in a cosmic dust profile that prior to launch was poorly understood. Because of this, a great deal of effort was put into the design of the TPS and modelling of the worst case particle fluxes PSP might experience [95].

1.2 Outline

In this thesis I present some early results from the PSP mission with an emphasis on measurements made by the SPAN-Ion instrument. In Chapter 2 I discuss Electrostatic Analysers (ESAs), SPAN-Ion instrument particulars, and various aspects of the instrument uncertainty. The next two Chapters are concerned with magnetic switchbacks (abrupt reversals of the radial magnetic field). To give some context, while switchbacks were known about and had received some study in the literature previous, few people were expecting the sheer number

of them that appeared in the measurements sent down after Encounter 1, instantly marking them as a core feature of the near-Sun solar wind and sparking a flurry of interest and research. In Chapter 3 I present a paper I wrote for the PSP First Results special issue using MHD invariants to probe switchback geometry. Chapter 4 expands upon this with a paper I wrote that discusses potential generation mechanisms and switchback fluctuation geometries using SPAN-Ion measurements. In Chapter 5, having improved upon the alpha particle fits I made for the analysis in Chapter 4, I present a paper I have written (to be submitted) that highlights a rarely studied aspect of alpha particle VDFs - alpha beams, in particular their statistical properties and relation to proton beams. In Chapter 6 we present a detailed case study of an ion scale wave event, modelling the plasma with double bi-Maxwellians for both the protons and alphas, identifying the wave modes generated and highlighting the roles of each species in driving the plasma locally unstable. Finally, in Chapter 7 I summarise our findings, putting them in context with recent research and outline potential avenues for future work. In particular, I highlight how with data from later encounters we are closer to resolving the question in Chapter 4 regarding where switchbacks originate.

Chapter 2

The SPAN-Ion Instrument

2.1 SPAN-Ion Overview

In this section we give a brief overview of the operating principles behind Electrostatic Analysers (ESAs), followed by a more detailed description of SPAN-Ion specifics and moment calculations. There are many excellent resources that cover ESA theory and operation in-depth, the interested reader may consider [166, 46, 187, 79], and of course the SPAN-Ion instrument paper [101].

2.1.1 Electrostatic Analysers

Figure 2.1 shows a cartoon schematic of a generic top-hat ESA. The design consists of two hemispherical plates separated by a small distance situated above an annular ring of segmented microchannel plates (MCPs), individually referred to as anodes. Incoming particles enter the aperture A and have their trajectories curved due to a voltage V applied between the plates that sets up a radial electric field. For a given applied voltage V, only those particles within an energy range dE of E will successfully travel from A to impact one of the measurement anodes (marked in grey) without colliding with either hemisphere; filtration of incoming particle energy E is thus achieved by sweeping through a range of voltages V. Top-hat ESAs are designed such that dE/E, the ratio of the width of the acceptance band in energy to the energy E, is a constant. The measurement anodes record the azimuthal angle ϕ of incoming particles. ϕ angles are therefore measured simultaneously - there is no stepping through of successive ϕ's. Filtration of an incoming particle's θ angle can be achieved in several different ways. Some missions use the spacecraft's spin to sweep through θ (as was done with the SWOOPS instrument on Ulysses [16] and 3dp on Wind [100]), while SPAN-Ion, because PSP is a non-spinning spacecraft, utilises deflector plates to apply external voltages that select which θ values are allowed into the aperture (these are the gold curved plates seen in the picture on the right of figure 2.1). Note that because the energy range of incident particles is being filtered by an applied voltage V, it is the energy per unit charge E/q, not the absolute energy E, that is being measured in a top-hat ESA. In
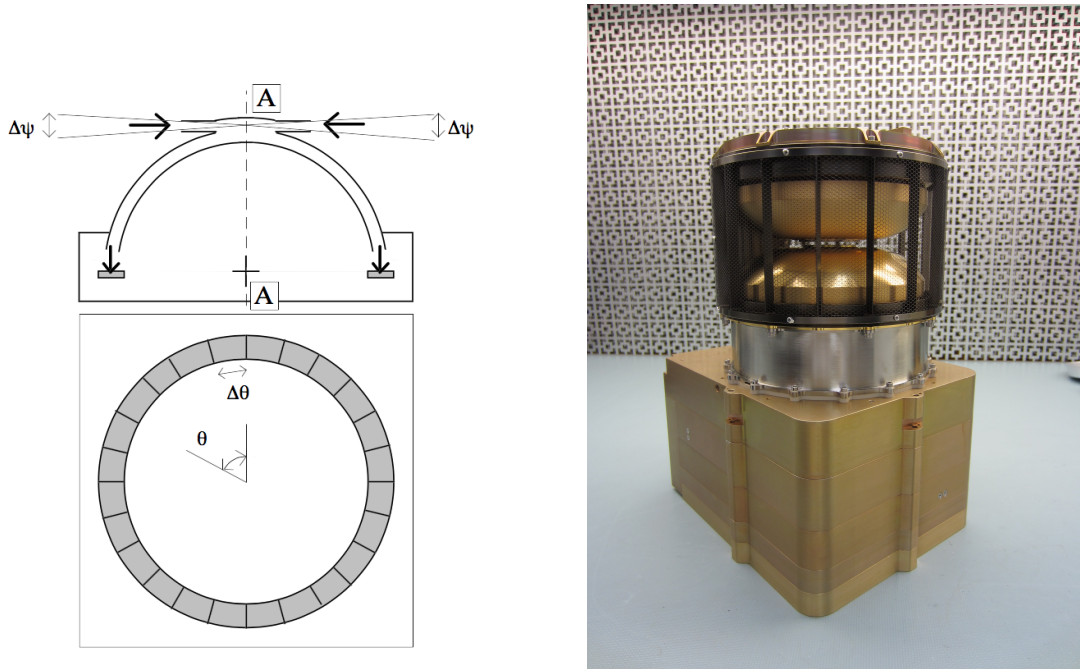
Figure 2.1: Left: Cartoon schematic of a typical ESA, showing the cross-section (in the instrument's plane of symmetry) of curved hemispherical places and an arrangement of the measurement anodes (from [135]). Right: The SPAN-Ion instrument (from [101]).

addition, there is no way to measure particle mass m and therefore no way to distinguish between particle species. In order to achieve mass per unit charge discrimination, an extra time-of-flight (TOF) stage is added between the exit aperture of the hemispheres and the detector anodes. A large (relative to the particle's thermal energy) voltage is applied to the exit particles, and the time between a particle passing through "START" and "STOP" thin carbon foils is measured. This time will be directly proportional to the square root of the mass per charge and can therefore be used to distinguish between different particles species.

2.1.2   SPAN-Ion

The SPAN-Ion ESA is primarily based on legacy technology used on the STATIC instrument on the MAVEN mission [121]. In figure 2.2 we show a more detailed schematic of SPAN-Ion with the electrostatic deflectors and hemispheres above the TOF stage, and the path (in blue) that an ion being measured takes through the instrument. The electrostatic deflector plates external to the hemispheres select for particle elevation angle θ as shown, and are controlled by voltages V_{D1} and V_{D2} ranging from 0 to 4 kV. The dashed lines either side represent the Faraday cage used to prevent field leakage and can be seen in the right panel of figure 2.1. The ions enter the aperture at the top of the hemispheres as shown, and the hemisphere voltages V_A, V_S select for E/q. Upon exiting the hemispheres the ions are accelerated by
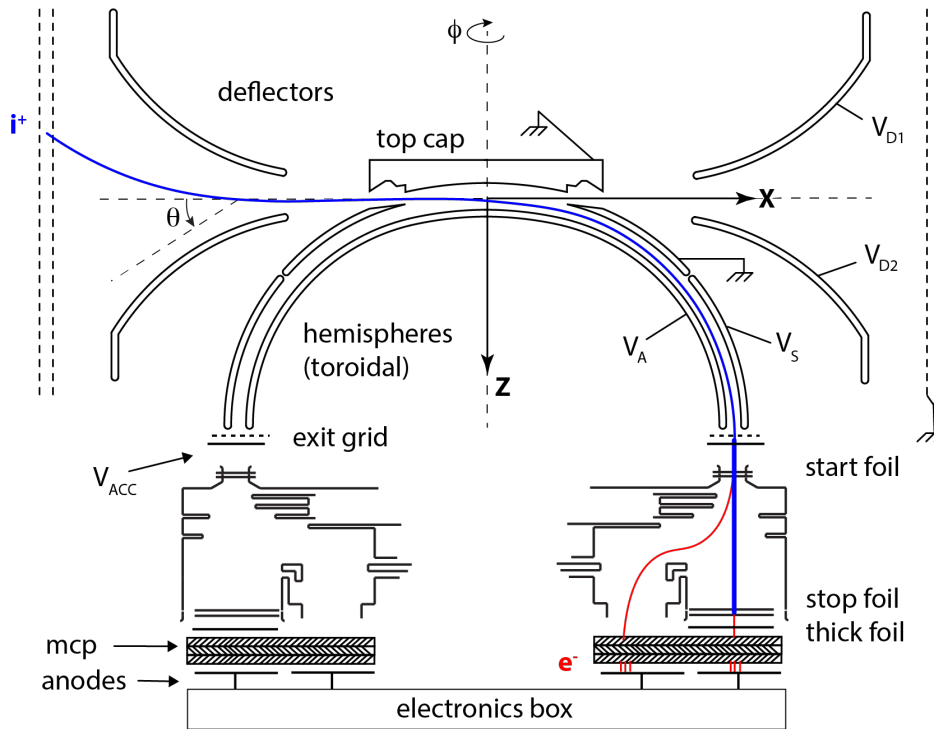
Figure 2.2: Cross-sectional schematic of SPAN-Ion showing the path of an entrant ion (blue) through the deflector plates, hemispheres, and TOF stage to be measured at the anodes. From The Solar Probe ANalyzer - Ions on Parker Solar Probe, Livi et al. 2022.

a -15kV voltage V_{acc} into a thin ($< 1\mu$g cm^{-3}) carbon foil. Secondary electrons produced by this collision are guided by a relatively small potential onto the MCPs above an inner set of "START" anodes (path shown in red). The cloud of electrons generated by the MCP triggers a START pulse on this inner anode. The accelerated ion (blue) continues through the start foil until it impacts the STOP foil, producing a STOP pulse on an outer STOP anode in a similar way. The time between the START and STOP pulses ($\lesssim 200$ ns) is then used to determine the particle's m/q using a dedicated mass look-up table.

Sweeps and Data Products

SPAN-Ion conducts two types of sweeps through velocity space - "full sweeps" and "targeted sweeps". A full sweep is a (relatively) coarse grained sampling of velocity space that is designed to capture the majority of the VDF, while a targeted sweep is a fine-grained sampling centred around the region with the highest counts (this region is determined dynamically by the instrument's processing unit after each full-sweep). The precise E/q and θ values

swept through are programmable and controlled by look-up tables, which map out the set of voltages V_A, V_S, V_{D1}, V_{D2} as functions of time. In general though, for both full and targeted sweeps, E/q starts at its largest value, θ values are swept through from positive to negative elevation, E/q is stepped down to its next value, and θ is then swept back up in the opposite direction (see figure 5 in [101]). Full and targeted sweeps each take 218.45 ms to complete. A full sweep consists of stepping through 8 deflector values and 32 energy steps, corresponding to a θ range from $\sim -60°$ to $+60°$ and a logarithmically spaced E/q range from 60 eV to 20 keV. Together with the 8 anodes, each of width 11.25°, a full-sweep measurement is therefore represented by an $8 \times 32 \times 8 = 2048$ element array of count values.

For encounters 2 through 4, 16 full sweeps were summed together to make up one proton channel (denoted "SF00") measurement, resulting in a baseline cadence of $16 \times 0.21845 \times 2 = 6.99$ s (the factor of 2 takes into account the time taken for targeted sweeps). For the alpha channel ("SF01") 32 full sweeps were summed together, resulting in a cadence of 13.98 s. This was changed after E4 to be the same number of full sweeps for both the SF00 and SF01 channels, putting the proton and alpha data products on the same time basis, convenient for data analysis.

Thermal Protection Shield and Field of View

The location of SPAN-Ion aft of the thermal protection shield (TPS) results in partial obstruction of the instrument's full field of view (FOV). In particular, the ion flux reaching anode 0 is significantly blocked, especially at smaller θ values. As the mission progresses, PSP's tangential velocities during encounter perihelia will increase, resulting in the bulk solar wind flow moving further into SPAN-Ion's FOV, and, necessarily, further out of SPC's FOV. This complementarity between SPC and SPAN-Ion was part of the overall mission design, as well as having the added benefit of redundancy in the particle measurements. In section 2.3 we discuss the effect of this on SPAN-Ion's moment measurements.

2.1.3   Plasma Moments

ESAs are designed to measure VDFs, so the fundamental expression is the one relating the counts $N(\mathbf{u})$ measured in the volume element centred at $\mathbf{u}$, and the distribution function evaluated at the same location in velocity space $f(\mathbf{u})$. For the subsequent discussion we follow both [166] and [79]. Intuitively, $N(\mathbf{u})$ will be proportional to the time spent counting particles in the volume element, the size of the volume element, the value of the distribution function $f(\mathbf{u})$, and the flux entering the instrument from this volume element. We can therefore write

$$N(\mathbf{u}) = \int dt \int d^3\mathbf{v}(\mathbf{v} \cdot \mathbf{A})\mathcal{G}(\mathbf{u}, \mathbf{v})f(\mathbf{v}), \qquad (2.1)$$

where $\mathbf{v} \cdot \mathbf{A}$ represents the particle flux through the entrance aperture with surface area vector $\mathbf{A}$, the time integral represents the measurement time during which counts are accumulated, the velocity integral is the integral over the volume element under consideration, and $\mathcal{G}(\mathbf{u}, \mathbf{v})$

is the instrument response function (equation 2.1 essentially *defines* $\mathcal{G}$). We make two simplifying assumptions. First, that any time dependence in $f(\mathbf{v})$ is small and can be neglected, in which case $\int dt \to t_{acc}$, the amount of time spent accumulating counts from the volume element, and second, that $f(\mathbf{v})$ is essentially constant over the region of velocity space in which the instrument response function G is non-zero, so that $f(\mathbf{v}) \approx f(\mathbf{u})$ and can be taken outside the integral. These two assumptions are equivalent to the statement that the instrument is fit for purpose and well-suited to measure the plasma it is intended to. Finally, the fact that for top-hat ESAs dE/E, and therefore dv/v, is a constant (as mentioned in section 2.1.1), means that $\mathcal{G}(\mathbf{u}, \mathbf{v})$ can only depend on the directions and not the magnitudes of $\mathbf{u}$ and $\mathbf{v}$, so is invariant under scalings. We can therefore substitute $\mathbf{v}' = \mathbf{v}/u$ into equation 2.1 to get

$$N(\mathbf{u}) = t_{acc}u^4 f(\mathbf{u}) \int d^3\mathbf{v}'(\mathbf{v}' \cdot \mathbf{A})\mathcal{G}(\mathbf{u}, \mathbf{v}') \tag{2.2}$$

$$\equiv t_{acc}u^4 f(\mathbf{u})G(\mathbf{u}). \tag{2.3}$$

The quantity $G(\mathbf{u})$ is known as the *geometric factor* and is experimentally measured during calibration. The way this is done is to send a beam into the instrument that is very narrow in velocity space relative to the region over which the response function $\mathcal{G}(\mathbf{u}, \mathbf{v})$ is non-zero. This allows us to approximate $f(\mathbf{v})$ in equation 2.1 as a delta function $f(\mathbf{v}) = n\delta(\mathbf{v} - \mathbf{V}_b)$, where n is the density of the beam (measured using a Faraday cup). Equation 2.1 then becomes

$$N(\mathbf{u}) = t_{acc}\mathcal{G}(\mathbf{u}, \mathbf{V}_b)V_{bn}, \tag{2.4}$$

where V_{bn} is the component of $\mathbf{V}_b$ normal to the instrument aperture. In this case then, the measured counts $N(\mathbf{u})$ (or flux, dividing by t_{acc}) will be directly proportional to $\mathcal{G}(\mathbf{u}, \mathbf{V}_b)$. Repeating this for a number of different beam velocities $\mathbf{V}_b$ builds up a picture of $\mathcal{G}(\mathbf{u}, \mathbf{V}_b)$ and the geometric factor $G(\mathbf{u})$ is then obtained via the integral in equation 2.2 (which becomes a sum over the number of calibration measurements you perform).

Since in practice SPAN-Ion is not sampling a continuous variable $\mathbf{u}$ but rather a discrete set of points in velocity space, we index each measurement point by (i, j, k), representing the (θ, ϕ, E) values respectively, and equation 3 becomes:

$$N_{ijk} = f_{ijk}v_k^4 t_{acc}G_j. \tag{2.5}$$

Note that while G can in principle exhibit dependence on all three variables, in practice for top-hat ESAs the ϕ (anode) dependence is dominant and so we simply write G_j.

Having obtained the expression relating counts measured by the instrument to the distribution function, it is straightforward to compute moments of f_{ijk}. For density n, we

have

$$n = \int f(\mathbf{v}) d^3\mathbf{v}$$

$$= \sum_{ijk} f_{ijk} d^3\mathbf{v}_{ijk}$$

$$= \sum_{ijk} \frac{N_{ijk}}{v_k^4 t_{\mathrm{acc}} G_i} v_k^3 \frac{dv_k}{v_k} d\Omega_{ij}$$

$$= \sum_{ijk} \frac{N_{ijk}}{v_k} W_{ijk} \tag{2.6}$$

where $d\Omega_{ij}$ represents the differential angular element and W_{ijk} essentially contains all instrumental quantities (recall that dv_k/v_k is a constant by design and therefore an intrinsic property of the ESA). Higher order moments like velocity and the pressure tensor are computed similarly, with the requisite powers of velocity:

$$nV_x = \sum N_{ijk} W_{ijk} \cos\theta_i \cos\phi_j$$

$$nV_y = \sum N_{ijk} W_{ijk} \cos\theta_i \sin\phi_j$$

$$nV_z = \sum N_{ijk} W_{ijk} \sin\theta_i$$

$$nP_{xx} = \sum N_{ijk} v_k W_{ijk} \cos^2\theta_i \cos^2\phi_j$$

$$nP_{yy} = \sum N_{ijk} v_k W_{ijk} \cos^2\theta_i \sin^2\phi_j$$

$$nP_{yy} = \sum N_{ijk} v_k W_{ijk} \sin^2\theta_i$$

$$nP_{xy} = \sum N_{ijk} v_k W_{ijk} \cos^2\theta_i \cos\phi_j \sin\phi_j$$

$$nP_{yz} = \sum N_{ijk} v_k W_{ijk} \cos\theta_i \sin\theta_i \sin\phi_j$$

$$nP_{xz} = \sum N_{ijk} v_k W_{ijk} \cos\theta_i \sin\theta_i \cos\phi_j$$

$$\vdots$$

Note that the power of v_k that appears in these summation expressions is one less than the power that appears in the integral definitions.

2.2 Moment Uncertainties

Having given an outline of the operation of SPAN-Ion and top-hat ESAs in general, we now move on to discuss potential sources of uncertainty in the SPAN-Ion measurements. In

particular we shall focus on "intrinsic" sources of error, that is, uncertainties inherent to the instrument itself and the nature of the measurement, and not things that can potentially be improved via further calibration. The three main issues we will discuss are:

(a) *Statistical Uncertainty.* From the expression for the number of particle counts N_{ijk} in an element of phase space, $N_{ijk} = f_{ijk}v_k^4 t_{\mathrm{acc}}G_j$, each measurement can be considered the outcome of a Poisson process with rate $\lambda = f_{ijk}v_k^4 G_j$, which therefore has an intrinsic uncertainty of $\delta N_{ijk} = \sqrt{N_{ijk}}$. We retain Poisson rather than Gaussian statistics here because although the counts in individual bins can become quite high at higher densities (some bin counts measure in the several 1000s as of PSP Encounter 8), the field of view of SPAN-Ion and the dynamic range of the instrument are such that most of the 2048 bins actually have $N_{ijk} < 10$.

(b) *Quantisation Noise.* In addition to this statistical measurement uncertainty, there is a systematic error introduced by a pseudo-log compression scheme applied to the raw counts, which is implemented on-board the spacecraft to reduce bandwidth requirements during data downlinks.

(c) *Partial Moments.* Finally, a systematic error is introduced due to the truncation of the VDF from the finite field of view of SPAN-Ion. This is mainly relevant in the instrument's ϕ or azimuthal direction, which corresponds most closely to the y-axis in instrument coordinates. As mentioned, the orientation of the instrument in combination with PSP's planned trajectory means that this will become less and less of an issue as the mission goes on, and the higher tangential speeds of the spacecraft will bring the solar wind VDFs further into the instrument's field of view.

We first consider the impact of (a) and (b) on moment uncertainties, and then discuss (c) in the next section.

2.2.1 Density Uncertainties

As mentioned, the Poisson uncertainty on a single count measurement N_i is simply $\delta N_i = \sqrt{N_i}$ (for brevity from here onwards we collapse the subscripts ijk to a single index i running from 1 to 2048). The compression scheme in (b) rounds each individual count N_i to their nearest element in the array `clog_19_8` that is less than or equal to N_i, where `clog_19_8` is given by

$$\texttt{clog\_19\_8} = [\,0, 1, 2, \ldots, 31,$$
$$32, 34, \ldots, 62,$$
$$64, 68, \ldots, 124,$$
$$\ldots$$
$$507904\,].$$

For example then any number in the range 64-67 will be mapped to 64, with an average error of 1.5, while any number less than or equal to 32 will have 0 error. Figure 2.3 shows Poisson
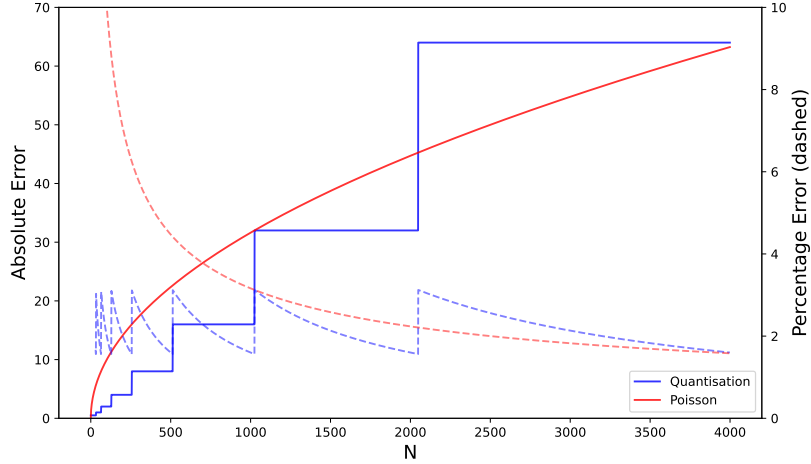
Figure 2.3: Comparison of quantisation (blue lines) vs Poisson (red lines) uncertainty as a function of bin count N. Corresponding percentage errors are shown on the right hand axis.

uncertainty in red and quantisation noise in blue as a function of bin count N_i. We can see that the Poisson uncertainty is much larger than quantisation noise up until $N_i \sim 2000$, although they are almost equal in the vicinity of $N_i = 1024$. As of E6, at the highest bin count number recorded was 1216. The quantisation percentage error is seen to not exceed roughly 3% (except for in the lowest count bins).

Writing the expression for moment density as

$$n = \sum_i N_i W_i^n \tag{2.7}$$

where W_i^n denotes the moment weights for density, we can add the Poisson and quantisation uncertainties in quadrature and compute the overall uncertainty δn as

$$\delta n^2 = \sum_i \delta N_i^2 W_i^2 \tag{2.8}$$

$$= \sum_i \left(N_i + \delta N_q^2 \right) W_i^2 \tag{2.9}$$

where δN_q is the quantisation error. This expression is not a simple function of the density (2.7) and so it's difficult to make precise statements about the behaviour of δn. However it is clear that the error is not a constant but will scale with the overall density, and that there will be a transition from initially Poisson dominated to quantisation dominated once the density

(and therefore counts) gets large enough. The precise range of the transition will depend on instrument specifics, in particular how coarse the compression scheme being used is and the typical densities being measured. It is in fact possible to observe this transition with a large enough data set (so that a large range of plasma parameters are observed). Figure
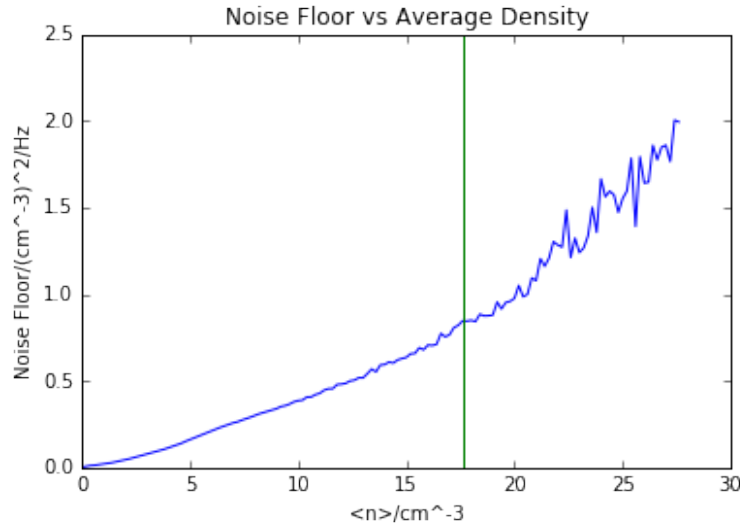
Figure 2.4: Plot illustrating the strong density dependence of the density power spectra noise floor (taken to be indicative of the density measurement uncertainty) on the measured density, using WIND 3dp data from 1996-2014.

2.4 is a plot made using Wind 3dp [100] (the ESA on the Wind spacecraft) data. Density measurements from the years 1996-2014 were binned into 10 minute intervals, and density power spectra plotted. At high frequencies the power spectra flatten out, representing the "noise floor" of the measurements, and this can be read off and used as a proxy for the measurement uncertainty δn^2 (see for instance the discussion in the appendix of [36]). This is then plotted vs the interval's average density. A clear proportionality between the level of the noise floor and the measured density is seen. In addition, as we predicted there is a transition from roughly linear scaling to something more than linear that occurs at higher densities of around 17 cm^{-3}, represents the transition to quantisation noise becoming dominant.

The main point here is that "noise floors" are usually considered to be a static, intrinsic property of space plasma instruments, but we can clearly see that for ESAs, because of the statistical nature of the measurement process, noise floors become strongly dependent on the plasma density. This applies not just to density but to the higher order moments as well, as we now show.

2.2.2 Velocity Uncertainties

In a similar way we can compute the uncertainties in the velocity moment components. Writing

$$nV_x = \sum_i N_i W_i^x \equiv A_x,\tag{2.10}$$

where W_i^x is the moment weight corresponding to V_x, we add the fractional errors in quadrature so that

$$\left(\frac{\delta V_x}{V_x}\right)^2 = \left(\frac{\delta n}{n}\right)^2 + \left(\frac{\delta A_x}{A_x}\right)^2.\tag{2.11}$$

The first term is easily computed from (2.9) and the second is $\sum_i \left(N_i + \delta N_q^2\right)(W_i^x)^2/A_x^2$. Figure 2.5 shows eq. 2.11 applied to real SPAN-Ion measurements (i.e. counts spectra),
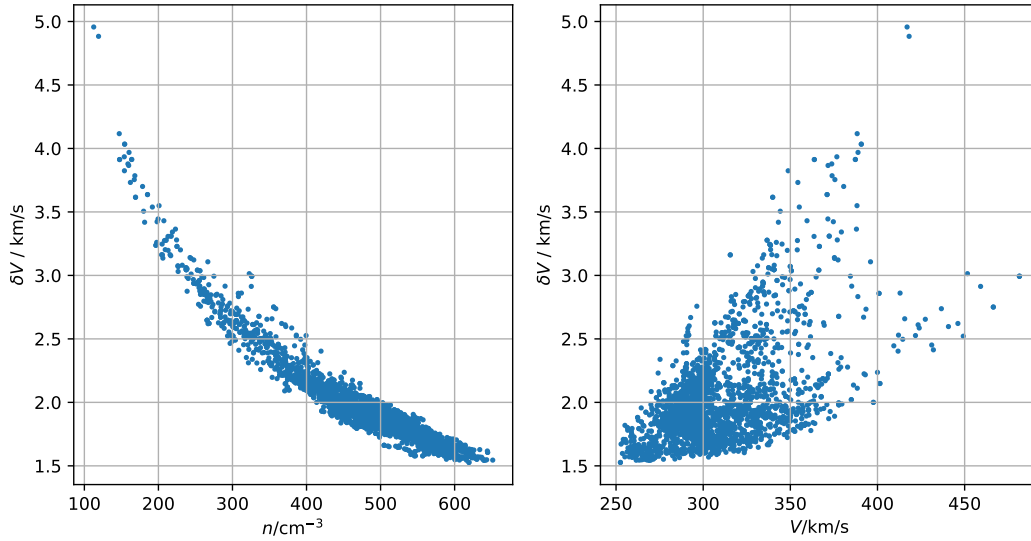
Figure 2.5: Velocity moment uncertainties δV expressed as a function of density (left) and velocity (right).

with data taken during PSP E4 from 20-01-28/09:56:27 to 20-01-28/21:43:33. We can see clearly see the $\delta V \sim 1/n$ and $\delta V \sim V$ scaling we expect from eq. 2.11, however the uncertainties are much better ordered as a function of density than solar wind speed. Again, we note that both the absolute and fractional uncertainties are not static but rather depend on solar wind parameters, however from the right hand figure we can see that a worst case fractional error $\delta V/V$ is around 1%.

It should be kept in mind that, while giving a useful idea of the size of moment uncertainties, this analysis is idealised in the sense that it represents the best case, lower bound

uncertainties, produced by the nature of the measurement and its subsequent compression. In practice there are a multitude of other sources of uncertainty that will be additive to this, for example:

1. Variations in micro-channel plate (MCP) efficiencies ϵ from anode to anode: Only a certain proportion ϵ of particles incident on an MCP are registered as counts (for SPAN-Ion this number is of the the order of 50% for the START anodes and 23% for the STOP anodes [101]), and this number can vary from anode to anode.

2. Dead-time corrections: After a particle impact there is a finite amount of time during which another count cannot be registered (this is the time taken for the electronics to amplify the signal and register it as a count). If count rates are very high, this effect can be significant and the measured count rate can severely underestimate the true count rate [135].

3. "Cross-talk" between anodes: Secondary electrons can "migrate" from an anode to its neighbour, registering as simultaneous counts on both anodes (see the discussion in section 4 of [101]).

2.3   Partial Moments

As mentioned in section 2.1.2, the location of SPAN-Ion on the spacecraft and its orientation with respect to the TPS mean that the FOV is partially blocked, giving rise to what we term "partial moments", as the full VDF is not always in the FOV. We now discuss the effect that this restriction has on the measurements, with particular emphasis on the y-components of the velocity vector and the temperature tensor, as these are the most significantly affected.

2.3.1   Simulation

To elucidate the effects of the truncated FOV, we set up a toy simulation of the instrument with logic as follows:

1. Start with an ideal bi-Maxwellian distribution function $f(\mathbf{v})$ with a given density n, parallel and perpendicular temperatures $T_\parallel, T_\perp$, and velocity $\mathbf{v}$.

2. Impose the FOV restrictions (that is, truncate that part of the VDF outside the FOV).

3. Convert $f(\mathbf{v})$ into counts, and quantise them, giving us a counts spectra.

4. "Measure" this counts spectra by taking its moments.

These "measured" moments can then be compared to the *true* values in $f(\mathbf{v})$ to determine the effect the finite FOV is having on the measurements. We can define a FOV parameter ϵ as

$$\epsilon = \frac{n_m}{n_{\text{true}}}, \tag{2.12}$$
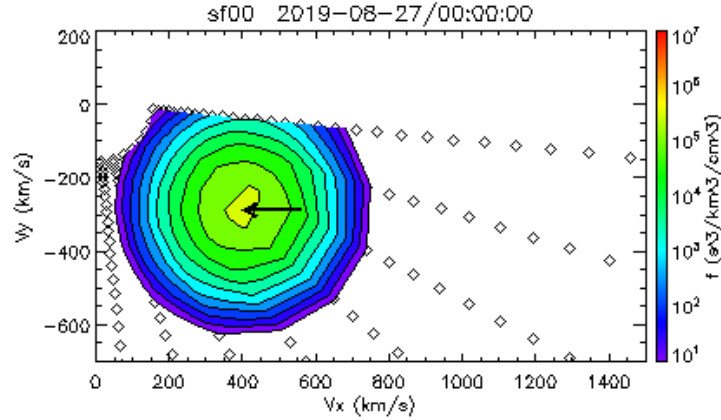
Figure 2.6: Ideal isotropic Maxwellian used to investigate errors in density and velocity moments due to the finite FOV, with parameters $n = 200$ cm^{-3} and $T = 60$ eV.

where n_m is the *measured* moment density and n_{true} is the true density of the input bi-Maxwellian. ϵ therefore captures how much of the VDF is within SPAN-Ion's FOV. This simulation is easily extended to account for core and beam populations, as well as individually testing the effect of including statistical noise or quantisation (we don't add either in the discussion that follows as we want to solely focus on the effect of the FOV).

2.3.2   Density Errors

We now carry out the simulation steps described above for an ideal isotropic Maxwellian with fixed parameters $n = 200$ cm^{-3}, $\theta = 0°$, and $T = 60$ eV, and allow longitudinal angle ϕ and wind speed V to vary over the range $[70°, 200°]$ and $[200, 700]$ km/s respectively. This VDF is shown in figure 2.6 (for the specific case $\phi = 145°$, $V = 500$ km/s). The resulting distribution of ϵ is shown in figure 2.7 (a). The lightest yellow region represents ϵ values of effectively 1, i.e. the VDF fully in SPAN-Ion's FOV. We can see the expected drop off in ϵ as a function of ϕ in both directions (although we are only really concerned with larger ϕ values in actual measurements). The drop off in ϵ at lower V values represents the VDF coming up against the lower bound of the energy range (top left in figure 2.6). The "serrated" edge on the right hand side of the distribution in (a), around $V \sim 650$ km/s, is due to the larger spacing of measurement points in velocity space at higher energies (consider the spacing of the diamonds in figure 2.6). For a fixed temperature, at some point the spacing between measurement points will become somewhat commensurate with the width of the distribution function, and the density will begin to be underestimated and the VDF not properly resolved. The apparent bumpiness is due to the VDF passing over and in-between the measurement points as ϕ is changed. The colder the beam, the lower the speed V at which this effect becomes important. Figure 2.7 (b) shows the distribution of solar wind measurements taken during E3 in terms of these variables, with the modal measurement
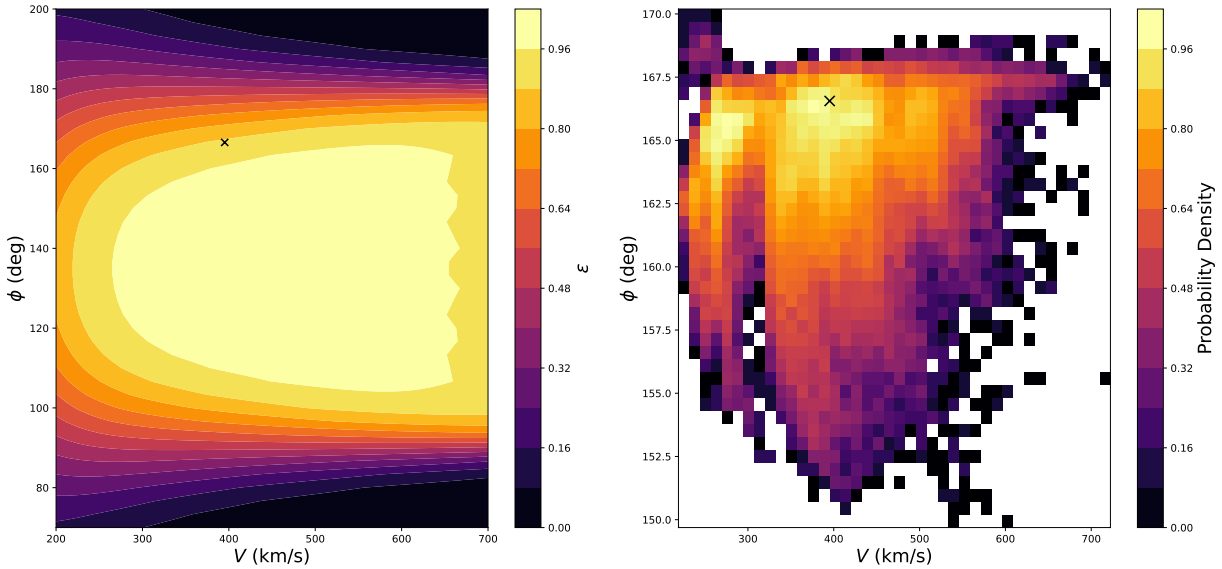
Figure 2.7: (a) Distribution of ϵ values as a function of ϕ angle and V, the total wind speed, for the simulation described in section 2.3.1. Black cross indicates the modal E3 measurement. (b) 2D histogram of E3 solar wind velocity measurements as a function of ϕ and V, with mode marked by a black cross.

marked by the black cross (reproduced on plot (a) as well), which gives an idea of where a typical encounter's solar wind measurement lies in the ϕ-V plane. While an ϵ value around 0.95 doesn't sound like a significant deviation or underestimate of the density, we will see it can have a surprisingly large effect on the velocity measurements. As mentioned, figure 2.7 (a) is made for an isotropic Maxwellian with $T = 60$ eV. If repeated for a Maxwellian with a larger temperature, the departure from $\epsilon \approx 1$ will start at smaller values of ϕ, as the distribution will be wider in velocity space and start moving appreciably outside the FOV more quickly. We point out that trying to take this temperature dependence into account by parametrising ϵ in terms of ϕ and the dimensionless sonic Mach number $M_s = V/w$, where w is the thermal speed, is not a useful thing to do because the mapping from M_s to ϵ is not one to one - two VDFs with the same M_s can have different ϵ values.

2.3.3 Velocity Errors

In figure 2.8 we show the differences between the measured velocity moment components and their true values, $\Delta V_i = |V_i^m - V_i^{\text{true}}|$, as functions of ϕ and V, and for the same ideal Maxwellian as before. Both the errors in the V_x and V_z components are essentially negligible over the range of solar wind velocities expected. As expected from the geometry seen in figure 2.6, the y-component V_y is the most severely affected. The top right plot shows that the absolute error in V_y can become very large close to the edge of the FOV, and that errors
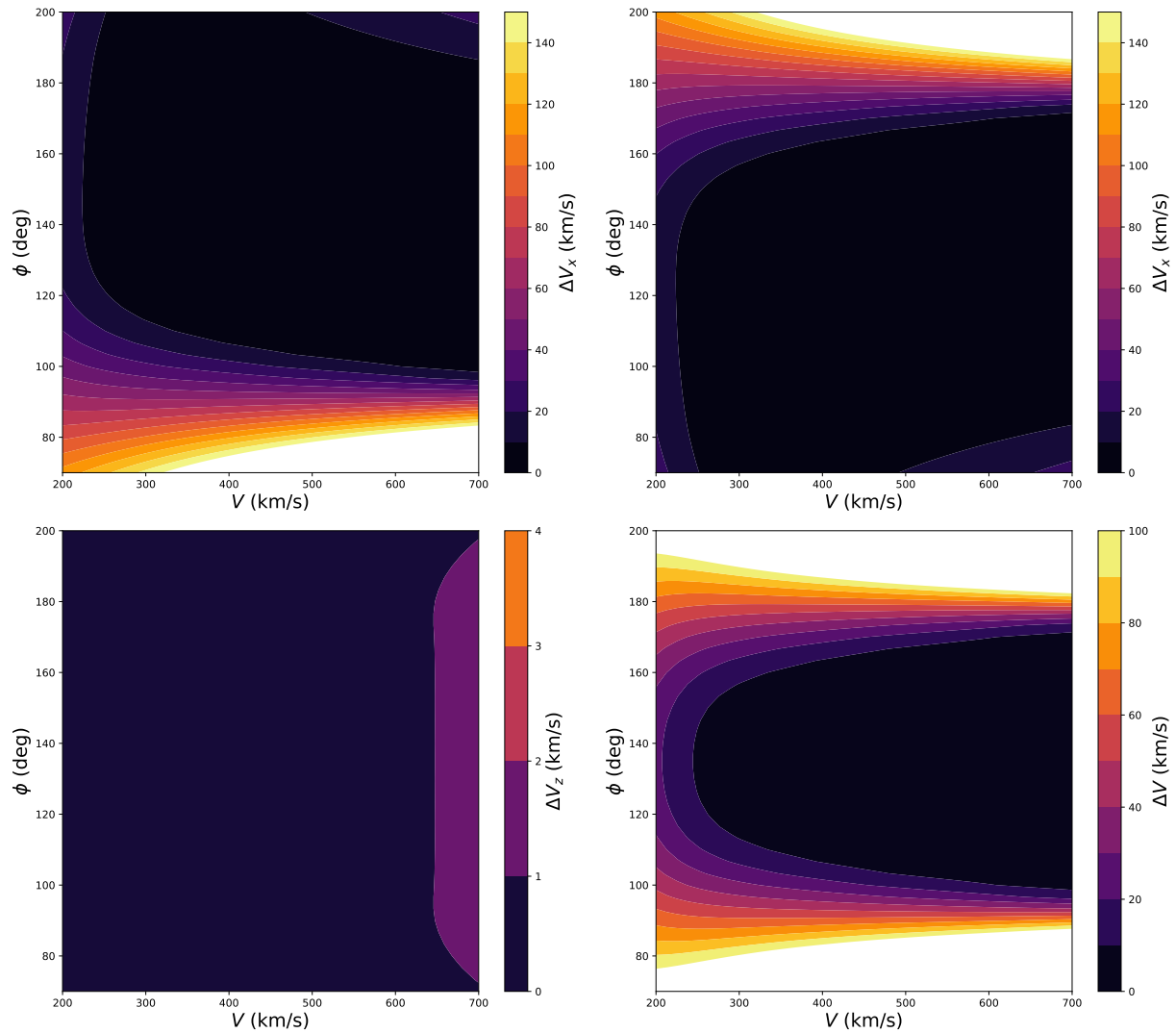
Figure 2.8: Measurement errors in velocity components V_x (top left), V_y (top right), V_z (bottom left), and speed V (bottom right), as a function of ϕ and wind speed V, for an ideal Maxwellian distribution function with $n = 200$ cm^{-3} and $T = 60$ eV. Note the different colour bar scales.

$\lesssim 60$ km/s are not atypical! The bottom right plot shows the magnitude of the vector difference $\Delta V = |\mathbf{V}^m - \mathbf{V}^{\text{true}}|$, which is poorly measured in the same regions of the ϕ-V plane as the y-component V_y is poorly measured. We point out however that the difference in *magnitudes* (not the vector difference), $dV = V^m - V^{\text{true}}$, is much smaller, almost always $\lesssim 10$ km/s. This is because $\mathbf{V}^m$ is roughly a rotation away from $\mathbf{V}^{\text{true}}$, since the finite FOV really only affects one component, V_y.

Sub-Alfvénic Intervals

We now extend the definition of ϵ slightly and discuss its use in the context of applying it to actual SPAN-Ion solar wind measurements (which include complications from beams and temperature anisotropies), as well as discuss the measurement and physical significance of the V_y component. If we first *fit* the actual measured counts spectra to derive a set of bi-Maxwellian parameters, and use these as the input to step 1 in section 2.3.1 above, then we can define

$$\epsilon \equiv \frac{n_m}{n_{\text{fit}}}, \tag{2.13}$$

where n_{fit} is the total fitted density, and n_m is the measured moment density produced by step 4, i.e. the amount of the VDF captured by the instrument ($0 \leq \epsilon \leq 1$). (In the discussion that follows we will use superscript "meas" to indicate real SPAN-Ion solar wind moment measurements, and sub/superscript m to mean those attained via inputting bi-Maxwellian parameters into step 1 of the simulation in 2.3.1.) ϵ again tells us how "in-the-FOV" the solar wind VDF is. From the point of view of the community, such a single-valued parameter would be used as a binary quality flag in the data, telling a user whether or not the SPAN-ion measurements can be trusted at a specific time.

Because this FOV parameter is a derived quantity produced *after* fits have been made to the raw measurements, a necessary prior is that the fit to the data is "good", even once failed/bad fits have been discarded. In other words, in order to get something useful from ϵ one must assume that the distribution is at least far enough in the FOV for a decent fit to be made in the first place. If one imagines an extreme example where the solar wind is almost completely out of the FOV (say only a small part of the tail of the VDF is visible), which may happen during cruise phase, then certainly a fit can be performed and ϵ computed, but ϵ will essentially be meaningless (as will be the fitted values).

Because of this, it may be desirable in the future for a more low-level parameter similar to ϵ that can be computed in linear time (i.e. without fitting), using data just found in either the L2 (raw counts) or L3 (moments) SPAN data files. One can envision several different schemes, for instance checking if there is a measurable peak in `EFLUX_vs_PHI`, or if the moment flow angle is above some critical angle away from the heat shield direction ($\phi = 180°$), etc. The necessary prior in the case of a peak in `EFLUX_vs_PHI` would be the less restrictive "the VDF has a peak", whereas the prior in computing ϵ as defined above could be framed as "the VDF has a *Gaussian* peak [which can then be fit to]".

For concreteness of our discussion we focus on two intervals of E8, interval A from 2021-04-28/12:00:00 to 2021-04-28/13:00:00, and interval B from 2021-04-29/06:49:00 to 2021-04-29/08:49:00. These intervals are of interest because they are the first time in the mission that PSP was clearly immersed in and measuring sub-Alfvénic flow, solar wind where the Alfvén Mach number $M_A = u/v_A$ is less than 1, where u is the solar wind speed and v_A the Alfvén speed. Intervals A and B are shown in figures 2.9 and 2.11 respectively. For both of these intervals, bi-Maxwellian fits to both the core and beam parts of the proton distribution have been performed. The left hand plot in fig. 2.10 shows an example of a proton VDF during
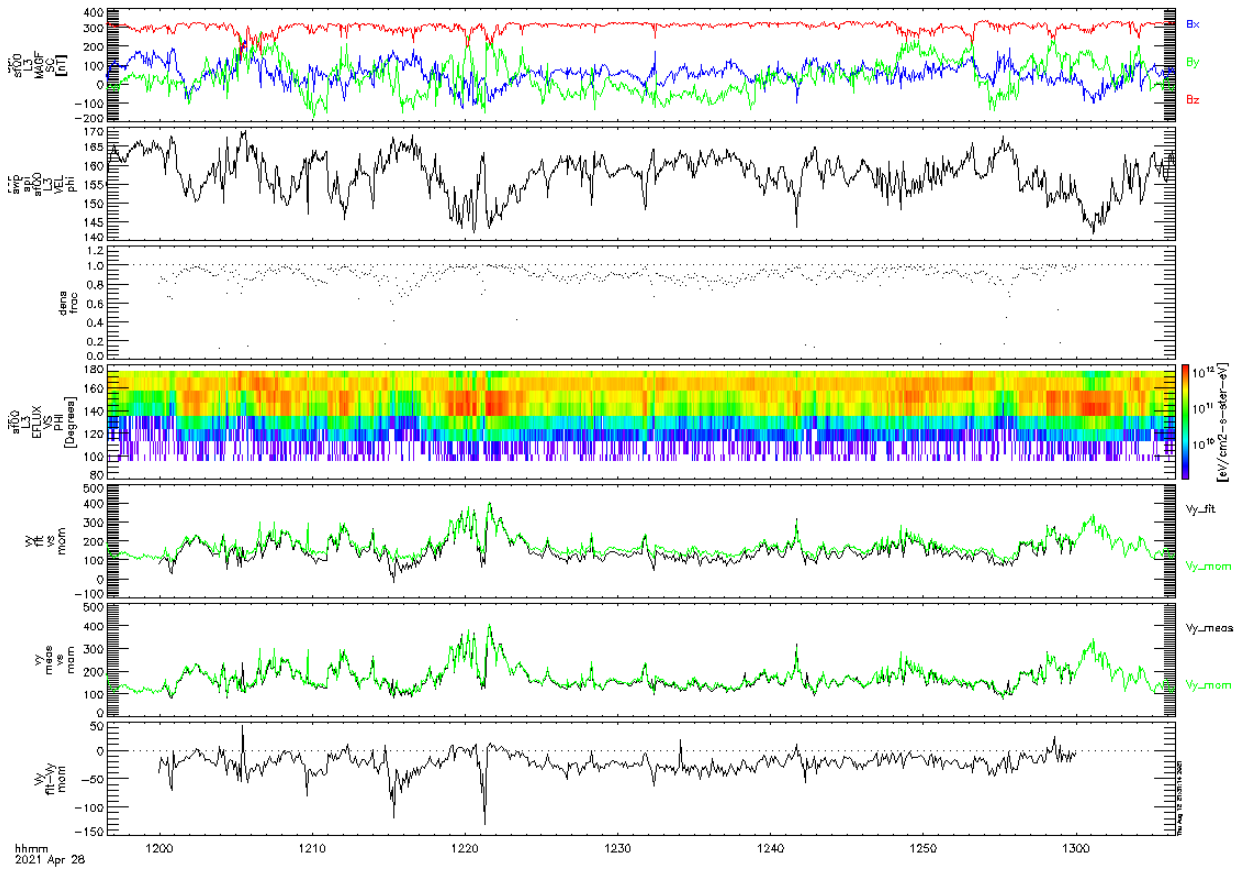
Figure 2.9: The first sub-Alfvénic interval during Encounter 8. Panels are (from top to bottom): magnetic field vector components in the spacecraft frame, measured ϕ angle of the solar wind flow, measured density fraction of the fit $\epsilon = n_{\mathrm{m}}/n_{\mathrm{fit}}$, particle energy flux as a function of ϕ, V_y^{fit} (black) and V_y^{meas} (green) overlaid, $V_y^{\mathrm{fit,m}}$ (black) and V_y^{meas} (green) overlaid, and difference between V_y^{meas} and V_y^{fit}.

this first interval, as viewed in the instrument's y-x plane. The VDF is highly anisotropic, with a large $T_\perp \sim 110$ eV, and no (or very negligible) beam component. This lack of a

beam, "bare core" type of distribution is quite unusual in the SPAN-Ion measurements from encounters 1 through 6, however it has appeared in proximity to the HCS in both E7 and E8. This raises the possibility that one source of proton beam generation is due to Alfvénic outflows/exhausts from reconnection events near the HCS [1] [138].

The large $T_\perp$ at this time is clearly causing a relatively large proportion of the VDF to be occluded. Using the simulation, we can compute what SPAN-Ion *would* observe as the measured moment density n_m, given the fit parameters. We then calculate the ratio $\epsilon = n_m/n_{\text{fit}}$, and plot this in the second panel in figure 2.9. By comparison with panels 2 and 4 (flow ϕ angle and particle energy flux as a function of ϕ) we can see that the distribution is most in the field of view ($\epsilon \approx 1$) at smaller ϕ, as expected, and falls to as low as $\epsilon \approx 0.6$.

As discussed above, using the azimuthal angle ϕ alone as a measure of how in the FOV the distribution is inadequate. Examining figure 2.10 we can see that it will also depend on the temperatures and the direction of the magnetic field (consider two distributions with the same velocity **v** but one much hotter than the other, the hotter one will lie more outside the FOV). For typical, almost radial magnetic fields, it is $T_\perp$ that determines how much of the VDF is outside the FOV, but if **B** significantly departs from radial, for instance during magnetic switchbacks, $T_\parallel$ becomes important. The ratio ϵ encapsulates all this information into a single number and is therefore useful for assessing the effect of the FOV limitations. Looking ahead to future programs of joint fitting SPC and SPAN-Ion distributions, or having a single data product that smoothly interpolates between the two sets of measurements, ϵ will be a useful single-valued quality flag to determine how well SPAN-Ion measurements can be trusted. It could also conceivably be separated into ϵ_{core} and ϵ_{beam}, to help identify times when the core is in SPAN-I's FOV and the beam in SPC's FOV, which can happen during switchbacks.
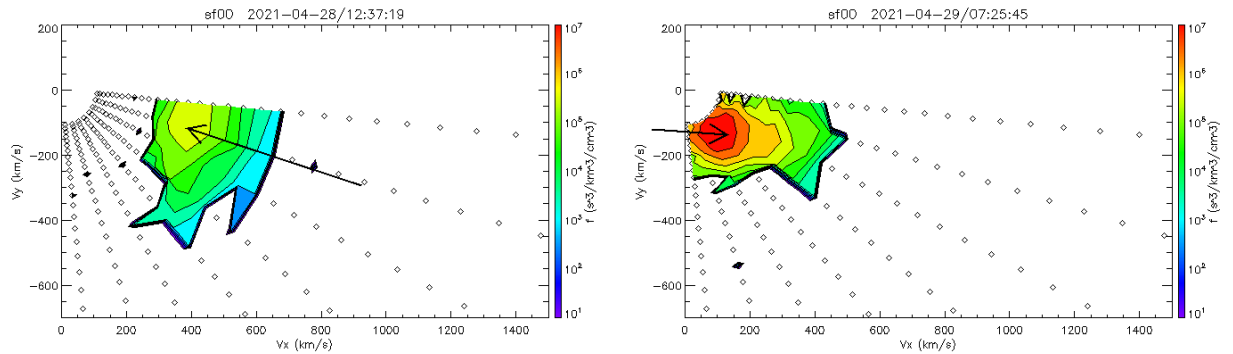
Figure 2.10: Proton VDFs from the sub-Alfvénic intervals A (left) and B (right), shown in the instrument's x-y plane. The arrow is the magnetic field scaled to the length of the Alfvén speed, with the tip centred at the moment velocity.

---

[1]We say one potential source because proton beams are ubiquitously observed in polar coronal hole wind which doesn't pass anywhere near the HCS [129].

From fig. 2.10 it is clear the velocity y-component is the one most affected by the VDF truncation, with the effect that the moments systematically overestimate V_y (note the sign of V_y has been flipped between figure 2.9 and figure 2.10). This effect can be seen in panel 5, which shows the y-component of the moment velocity, as actually measured by SPAN-Ion, in green, overlaid with the y-component of the proton velocity fits, in black. The moment curve is consistently above the fit curve, and the largest discrepancies occur when ϵ is furthest from 1. This tells us that (i) the fits are "working" in the sense that they are effectively filling in the part of the VDF outside the FOV and counteracting the systematic error in V_y^{meas}, and (ii) they therefore provide a *better* upper bound on the true V_y compared to the moments. The discrepancies between fit and moment can be very large, as much as 100 km/s, as seen in the bottom panel of $V_y^{\text{fit}} - V_y^{\text{meas}}$, which is a similar magnitude to the differences seen in the top right panel of our simulated velocity measurements in figure 2.8).

Compare this now to interval B, shown in figure 2.11. The density fraction ϵ hugs $\epsilon = 1$ far more closely than in interval A, meaning the VDF is well inside the FOV, despite both intervals having very similar V_y values! ϵ remains essentially 1 even through changes in ϕ (panel 2) and energy flux (panel 4). The VDF on the right in figure 2.10 backs this up, where we can see the full core of the distribution (darkest red) fully in the field of view, due to the fact that it's more isotropic and at a lower temperature. Practically speaking this means if one is interested in measuring bulk tangential velocities during this particular period, there is no real difference between using moments and fits, as can be seen from the overlays in panel 5 and the differences in panel 7 (the differences are so small as to be within the moment uncertainties described previously). For interval A on the other hand, fits must be used.

Accurate determination of V_y from SPAN-Ion data is extremely important due to its relation to angular momentum measurement. The V_y component is the one closest to the tangential direction (there is a 20° rotation offset about the $\hat{R}$ direction). Angular momentum flux is a notoriously difficult quantity to measure (see the discussion in [141] and these concerns in relation to PSP in [50]). Data from early encounters appeared to show [83] tangential flows V_T an order of magnitude higher than those expected from the canonical Weber-Davis model [177], an unexpected result which would seriously challenge our understanding of solar wind dynamics. These measurements were made using SPC however, which is intrinsically less well-suited to measuring non-radial flow, and a thorough understanding of tangential flow measurements using SPAN-Ion is thus essential. Its relevance to these sub-Alfvénic flow periods is that, assuming the co-rotation predicted by Weber-Davis, V_T will be largest and therefore easiest to measure at the Alfvén critical point, and the uncertainty on angular momentum flux L will therefore be minimised.

Finally, in figure 2.12 we plot histograms of FOV ϵ values for encounters 3, 4 and 7. There is a clear trend of higher ϵ values in later encounters, which we would expect as PSP's tangential speeds increase in successive orbits. All three distributions are centred firmly above or around $\epsilon \sim 95\%$, however as we showed above in the first example E8 interval, it doesn't take much of a departure from $\epsilon = 1$ to produce a very large difference between
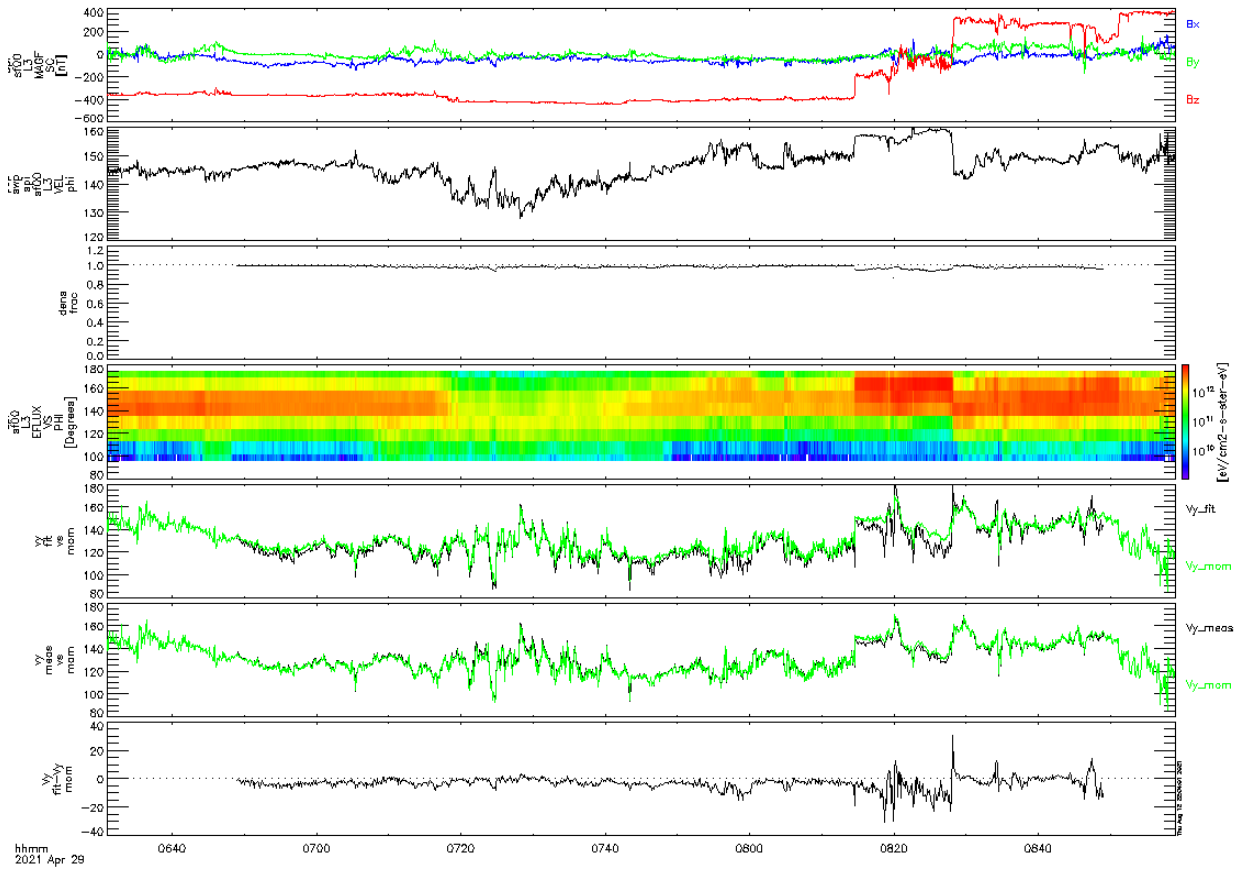
Figure 2.11: The second sub-Alfvénic interval of Encounter 8. Panels are as described in fig. 2.9

V_y^{fit} and V_y^{meas}. ϵ is therefore more useful as a relative parameter when studying individual intervals rather than something to use to draw broad conclusions about an encounter as a whole.

2.3.4   Temperature errors

We now consider the effects of the FOV on the measurement of the temperature tensor **T**. For this, we use an ideal bi-Maxwellian with parameters $n = 400$ cm^{-3}, $T_\perp = 60$ eV, $R = T_\perp/T_\parallel = 2$, $\theta = 5°$ and $\mathbf{B} = (200, 0, 0)$ nT, shown in figure 2.13. We choose this magnetic field **B** so that the off-diagonal components of **T** vanish in the SPAN-Ion instrument frame and make it easy to assess the impact of the FOV on the moment measurements. The results are shown in figure 2.14, where we again plot 2D contour maps of the errors in each component ΔT_{ij} as a function of ϕ and wind speed V.
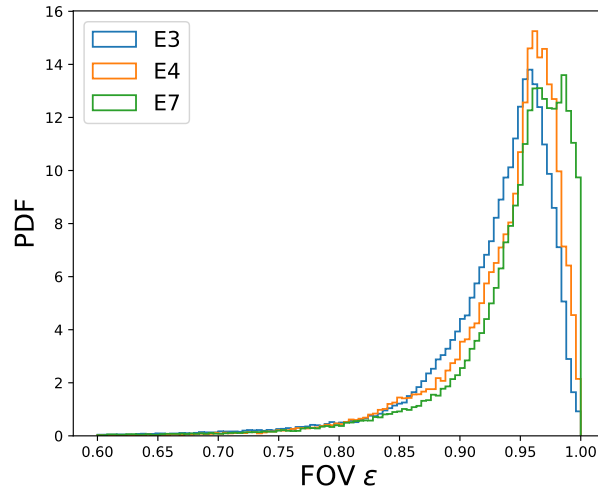
Figure 2.12: Histograms of the field of view parameter ϵ for E3, E4 and E7.

We can see that over the expected region of the ϕ-V plane where the solar wind velocity usually lies, the errors in T_{xx} and T_{zz} are both small enough as to be fairly negligible, $\lesssim 4$ eV in both cases. The errors in the T_{yy} component on the other hand are very large, approaching ~ 30 eV near the edge of the FOV, which is a fractional error of $\sim 50\%$! The off-diagonal components (which should all be 0 for this bi-Maxwellian) all remain small over the region where we expect solar wind measurements, although the y-components T_{xy} and T_{yz} have larger maximum errors than T_{xz} (note the different colourbar scales).

We may also be interested in how much the truncated FOV affects the diagonalisation of **T**. To test this, we diagonalise the measured **T**, take the eigenvector corresponding to $T_{\parallel}$, $\mathbf{e}_{\parallel}$, and compute the angle this vector makes to the known **B** field, given by $\alpha = \cos^{-1}(\mathbf{e}_{\parallel} \cdot \hat{\mathbf{B}})$. This gives an indication of how much the truncation in the y-direction is causing **T** to be "skewed", resulting in a misalignment between $\mathbf{e}_{\parallel}$ and **B**. The results are shown in figure 3.4. The misalignment angle α can be quite large, up to 9° close to the edge of the FOV. Interestingly, the influence of the FOV seems to extend further into the ϕ-V plane (in comparison to **V** and **T**, figures 2.8 and 2.14), giving a misalignment of $\alpha \lesssim 2°$ to 3° even when the VDF is fairly well inside the FOV, and α also seems to be very sensitive to the truncation of the VDF at low energies. Given that this is an idealised simulated measurement and we are getting several degrees of misalignment, we conclude that α is quite a sensitive quantity and it does not take much for the symmetry axis of **T** to deviate from **B**.

Mitigating the FOV Effect

As discussed above and shown in figure 2.14, it is clear that the y-components of the temperature tensor (T_{yy}, T_{xy}, T_{yz}) are the problem components (as was the case with the velocity
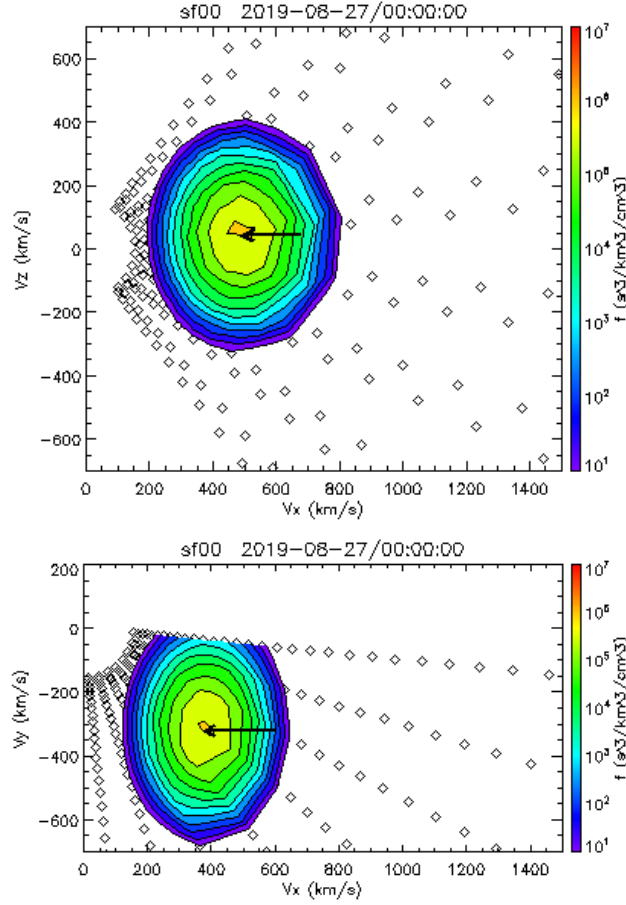
Figure 2.13: Ideal bi-Maxwellian used in the simulation measurements of the temperature tensor, which has parameters $n = 400$ cm^{-3}, $T_\perp = 60$ eV, $R = T_\perp/T_\parallel = 2$, $\theta = 5°$ and $\mathbf{B} = (200, 0, 0)$ nT. Top panel shows the VDF in the x-z plane (summed over ϕ), and the bottom panel the VDF in the x-y plane (summed over θ).

moments). Unlike the velocities however, it is possible to work around this restriction some-what by taking advantage of some reasonable assumptions. The idea is straightforward - the temperature tensor $\mathbf{T}$ involves the measurement of 6 numbers, $T_{xx}, T_{yy}, T_{zz}, T_{xy}, T_{yz}, T_{zx}$, but in practice for solar wind ion VDFs we are usually only really interested in two numbers, the parallel and perpendicular temperatures $T_\parallel$ and $T_\perp$, obtained via diagonalisation of $\mathbf{T}$. The assumption needed is that the solar wind VDF is gyrotropic and well-described by two temperatures. Therefore, if this is the case, there should be enough degrees of freedom to eliminate any y-components from the equations and calculate $T_\perp, T_\parallel$ using only the x and z-components of $\mathbf{T}$, as we now show.

Let $\mathbf{T}$ be the temperature tensor as measured in the SPAN-Ion instrument frame, $\tilde{\mathbf{T}}$ the
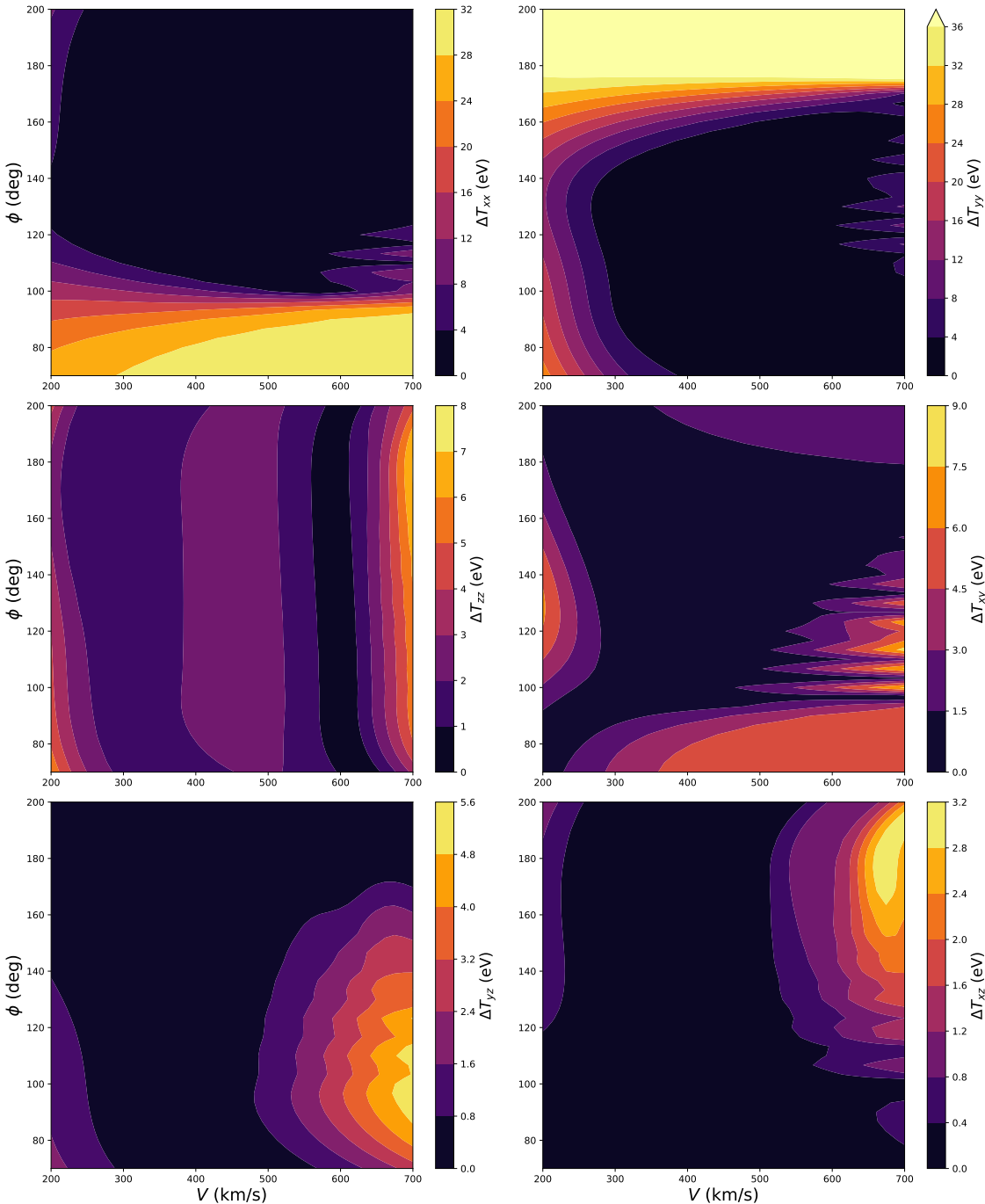
Figure 2.14: Measurement errors in the individual components of the temperature tensor **T** for the ideal bi-Maxwellian distribution function shown in figure 2.13, as a function of angle ϕ and wind speed V. Note the different colour bar scales.
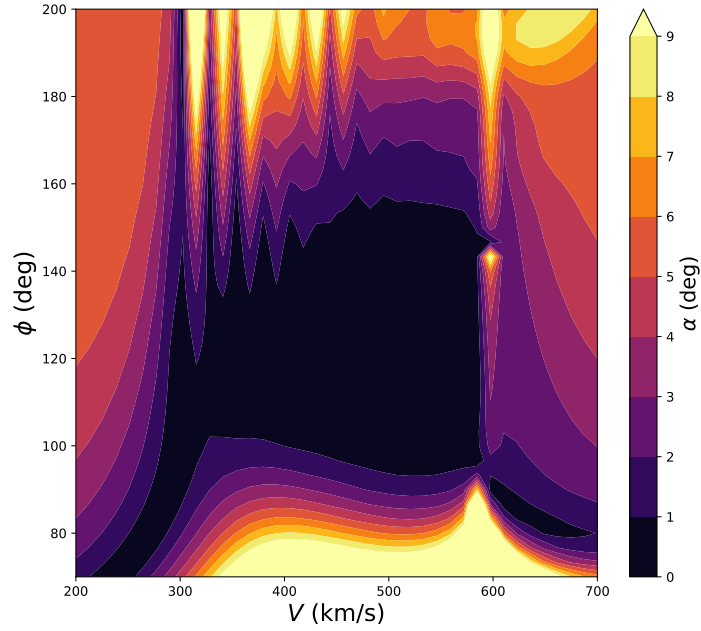
Figure 2.15: 2D contour plot of the angular difference between the direction of **B** as inferred from diagonalising the temperature tensor **T**, and the true direction of **B**, as a function of angle ϕ and wind speed V, for the ideal bi-Maxwellian shown in figure 2.13 and used in figure 2.14.

temperature tensor in the magnetic field frame, with x-axis aligned along the direction of **B**, and **R** the rotation matrix taking us from **T** to $\tilde{\mathbf{T}}$. We have then

$$\mathbf{T} = \begin{pmatrix} T_{xx} & T_{xy} & T_{xz} \\ T_{yx} & T_{yy} & T_{yz} \\ T_{zx} & T_{zy} & T_{zz} \end{pmatrix}, \tag{2.14}$$

$$\tilde{\mathbf{T}} = \begin{pmatrix} T_\parallel & 0 & 0 \\ 0 & T_\perp & 0 \\ 0 & 0 & T_\perp \end{pmatrix}, \tag{2.15}$$

$$\mathbf{R} = \begin{pmatrix} a & b & c \\ d & e & f \\ g & h & i \end{pmatrix}, \tag{2.16}$$

and

$$\mathbf{R}\mathbf{T}\mathbf{R}^T = \tilde{\mathbf{T}}. \tag{2.17}$$

Since equation 2.17 represents an over-constrained set of 6 linear equations, the plan is to invert equation 2.17, write out the equations explicitly, and solve only those not involving the
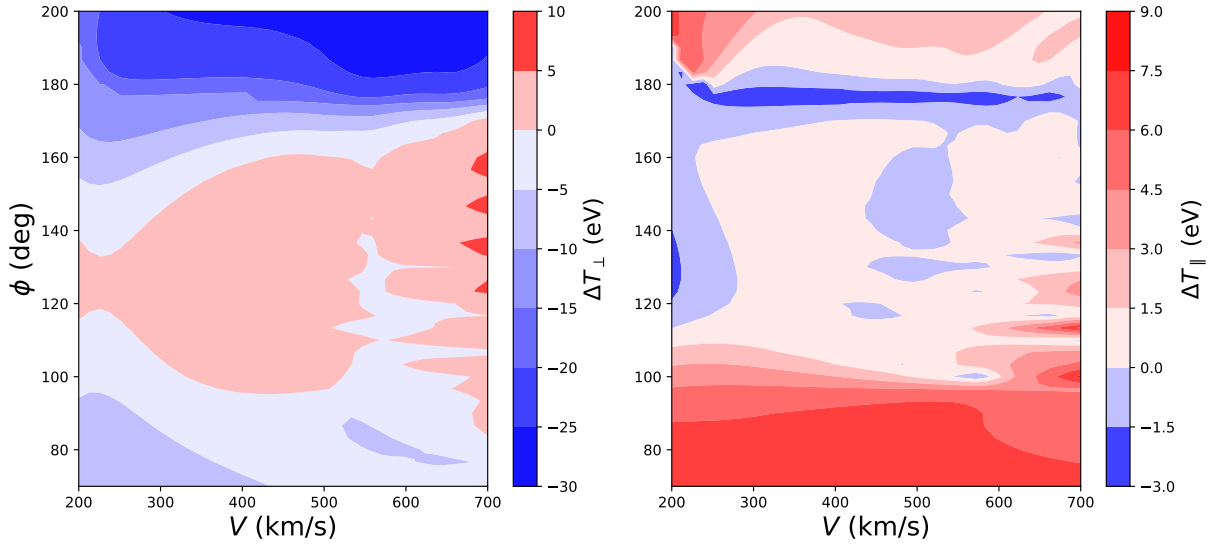
Figure 2.16: Comparison between determinations of $T_\perp$ and $T_\parallel$ made using direct diagonalisation of the temperature tensor, and via the component elimination method described in the text - computing them without using any of the y components of $\mathbf{T}$.

y-components of $\mathbf{T}$. Since $\mathbf{R}$ is a rotation matrix, $\mathbf{R}\mathbf{R}^T = \mathbf{I}$ and so $\mathbf{T} = \mathbf{R}^T\tilde{\mathbf{T}}\mathbf{R}$. Expanding this out and keeping only x and z components we have

$$T_{xx} = a^2 T_\parallel + (d^2 + g^2)T_\perp \tag{2.18}$$

$$T_{xz} = ac T_\parallel + (df + gi)T_\perp \tag{2.19}$$

$$T_{zz} = c^2 T_\parallel + (f^2 + i^2)T_\perp. \tag{2.20}$$

We can choose any two of these equations to solve for $T_\perp$ and $T_\parallel$. We choose (T_{xx}, T_{zz}), which avoids the (physically unlikely) corner case of T_{xz} being exactly zero and $\mathbf{B}$ being aligned with one of the coordinate axis directions, making the equations non-invertible. Writing

$$\begin{pmatrix} T_{xx} \\ T_{zz} \end{pmatrix} = \begin{pmatrix} a^2 & d^2 + g^2 \\ c^2 & f^2 + i^2 \end{pmatrix} \begin{pmatrix} T_\parallel \\ T_\perp \end{pmatrix}, \tag{2.21}$$

we can simply invert this equation to obtain $(T_\parallel, T_\perp)$. We now apply this method to our simulation to test if it really does constitute a better method of measuring $T_\parallel$ and $T_\perp$ and therefore mitigates the impact of the finite FOV on the temperature moments. Defining

$$\Delta T_\perp = |T_\perp^c - T_\perp^{\text{true}}| - |T_\perp^d - T_\perp^{\text{true}}| \tag{2.22}$$

$$\Delta T_\parallel = |T_\parallel^c - T_\parallel^{\text{true}}| - |T_\parallel^d - T_\parallel^{\text{true}}|, \tag{2.23}$$

where T_i^{true} represents the "true" value of the parallel and perpendicular temperatures of the bi-Maxwellian VDF fed into the simulation, T_i^d the value obtained via straightforward

diagonalisation of $\mathbf{T}$, and T_i^c that obtained via the component elimination method just described (and $i = (\|, \perp)$). Negative values of ΔT_i therefore represent a *better* measurement and a reduction of the error in the moment. In figure 2.16 we plot 2D contour plots of $\Delta T_\perp$ and $\Delta T_\|$ as a function of V and ϕ for an ideal bi-Maxwellian with parameters $n = 400$ cm^{-3}, $\theta = 5°$, $T_\perp = 60$ eV, $T_\| = 24$ eV, and $\mathbf{B} = (200, -60, 30)$ nT. The right plot of $\Delta T_\|$ shows that there is no significant change in either direction in the measurement of $T_\|$, which is intuitively what we would expect from the orientation of the VDF in figure 2.13 - the parallel temperature is not really affected by the FOV restriction. The darker red contours around $\phi \lesssim 90°$ represent a region where the method is not working as well as direct diagonalisation. The reason for this is that once the VDF has swung around to such low ϕ values and is hitting the bottom edge of the FOV, it is then the T_{xx} component which is the poorly measured one, not T_{yy}. The left plot of $\Delta T_\perp$ shows that, when the VDF is entirely within the FOV (centre of ϕ-V plane), there is not much of a difference between the two methods, as would be expected (if anything the component method seems to perform worse by a few eV). In this region directly diagonalising $\mathbf{T}$ gives a good measurement of $T_\perp$. Importantly however, near the edge of the FOV, we see that the component elimination method is working as desired and does significantly better at extracting $T_\perp$ from $\mathbf{T}$, by as much as $10 - 15$ eV! This represents a very large improvement considering $T_\perp = 60$ eV, and the component elimination method should be used in these regions of the ϕ-V plane.

Intuitively this method is very simple. If we consider figure 2.13, we are using the fact that despite the VDF being cut off in the y-direction, SPAN-Ion clearly *has* measured $T_\perp$ and $T_\|$ (in the case of the pictured VDF, it has measured $T_\perp$ in the $y - z$ plane). $\mathbf{T}$ therefore does contain this information, but directly diagonalising $\mathbf{T}$ mixes all the components together, including the poorly measured y ones. The method works by simply ignoring the bad components before diagonalising.

2.4 Field Alignment of the VDF

We conclude this chapter with a brief discussion of the issue of field alignment of the measured VDFs. While non-gryotropic VDFs certainly do occur in the heliosphere (for instance at comets [60], high Mach-number shocks [55] or near discontinuities in the solar wind [6]), the VDFs making up the bulk solar wind are generally expected to be gyrotropic. This is because any asymmetry in the VDF with respect to the magnetic field direction will quickly gyrotropise under the influence of the Lorentz force, on a timescale given by the cyclotron frequency, $\omega_p^{-1} = m/qB$ (this is the justification of our assumption in the previous section). As an example, in the three days around perihelion for E7, the median proton gyroperiod is $T_g = 0.28s$, an order of magnitude shorter than the SPAN-Ion measurement cadence of 3.5s, precluding the possibility of SPAN-Ion being able to measure any non-gyrotropy present in the particle VDFs. We should point out however that it may be possible in the future to tease out signatures of non-gyrotropy using SPAN-Ion's highest cadence archive measurements, which are at a cadence of 0.218s, comparable to T_g. This may particularly be

feasible when observing low phase space density features which may be gyro-phase bunched, such as those produced by velocity space diffusion [169].

Diagonalising the measured temperature tensor of a gyrotropic VDF will therefore give us the familiar $T_\parallel, T_{\perp,1}, T_{\perp,2}$, with $T_{\perp,1} \approx T_{\perp,2}$, and the eigenvector corresponding to $T_\parallel$ should point along the magnetic field direction. Assessing the symmetry direction of the measured VDFs in comparison with the magnetic field measurements from FIELDs is therefore a very useful diagnostic for SPAN-Ion, in that it will highlight any systematic misalignment errors that may be present. There are several things to consider when using the temperature tensor in this way to derive the direction of $\mathbf{B}$ however:

1. The more isotropic the distribution function becomes, the more the eigenvectors of the temperature tensor approach degeneracy, and the less well defined the inferred magnetic field direction will be. The best measurements of $\mathbf{B}$ from $f(\mathbf{v})$ will therefore be when prominent beams are present in the distribution.

2. As discussed in the previous section, the finite FOV affects the measurement of the temperature tensor as it does every other moment. In particular, SPAN-Ion's truncation of the VDF along the $\phi = 163.5°$ direction will break the gyrotropic symmetry of the VDF unless $\mathbf{B}$ happens to lie exactly perpendicular to this direction (which it rarely does). There is therefore no reason to expect good measurements of $\mathbf{B}$ derived from $f(\mathbf{v})$ if there is appreciable FOV occlusion.

3. All instruments on PSP have intrinsic pointing uncertainties. SPAN-Ion, along with ISOIS and WISPR have pointing accuracy requirements of $< 1°$ and so this potential source of systematic error is thought to be negligible.

4. $\mathbf{B}$ itself fluctuates during a SPAN-Ion accumulation time (3.5s). The amount it fluctuates should therefore be considered a lower bound on how well SPAN-Ion's $f(\mathbf{v})$ can be aligned with $\mathbf{B}$.

With these considerations in mind, to see how well SPAN's $f(\mathbf{v})$ is aligned with $\mathbf{B}$ we consider an interval on the day of E7's perihelion. The proton VDFs during this interval display very prominent ion beams and are well in the FOV, and the background magnetic field is very quiet. The interval is shown in figure 2.17, a distinctly quiet radial field period that occurs after a series of switchback patches and just before a crossing of the HCS. The second and third panels show the θ and ϕ components of $\mathbf{B}$ as measured by SPAN and FIELDS. It is clear that the θ values agree very well, and the ϕ slightly less so, with perhaps a slight systematic shift in the value of ϕ between the two measurements. The bottom two panels in figure 2.17 show histograms of the angular differences $\Delta\theta$ and $\Delta\phi$. Both distributions are very narrowly peaked. The median $\langle\Delta\theta\rangle = -0.6°$ confirms the excellent agreement in the θ direction, and $\langle\Delta\phi\rangle = 4.6°$ shows a small systematic offset in ϕ. Given the angular width of the anodes is $11.25°$, we consider this finite $\Delta\phi$ to be acceptable and that these two measurements are in satisfactory agreement.
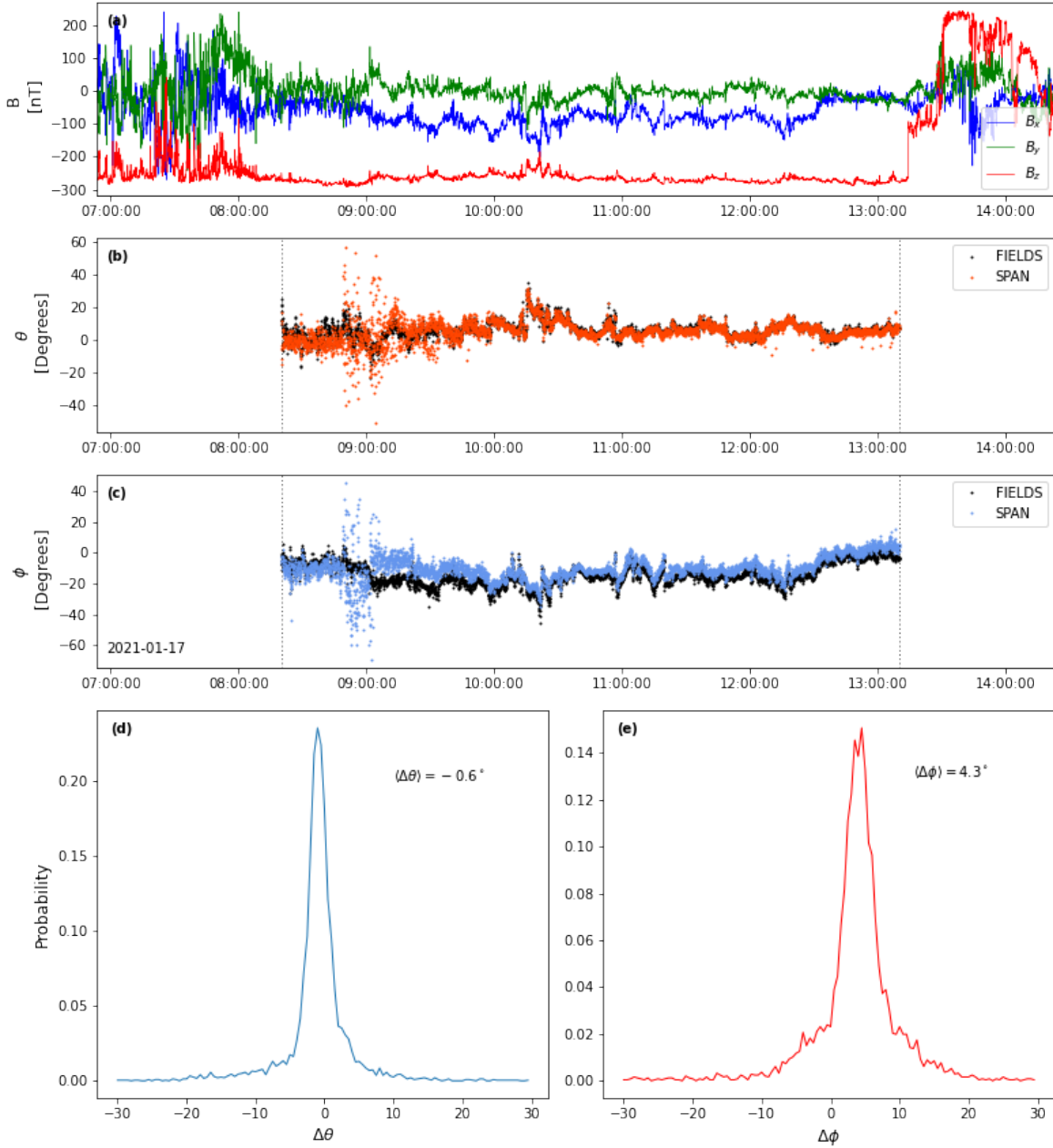
Figure 2.17: Interval from E7's perihelion used in computing **B** from SPAN-Ion's temperature tensor. Panels are: (a) Magnetic field in SPAN-Ion instrument coordinates, (b) θ component of **B** as measured by SPAN-Ion (red) and FIELDS (black), (c) ϕ component of **B** as measured by SPAN-Ion (blue) and FIELDS (black), (d) and (e) histograms of angular differences between FIELDS and SPAN-Ion in θ and ϕ respectively. $\langle \Delta\theta \rangle$ and $\langle \Delta\phi \rangle$ denote median values of each angular difference.
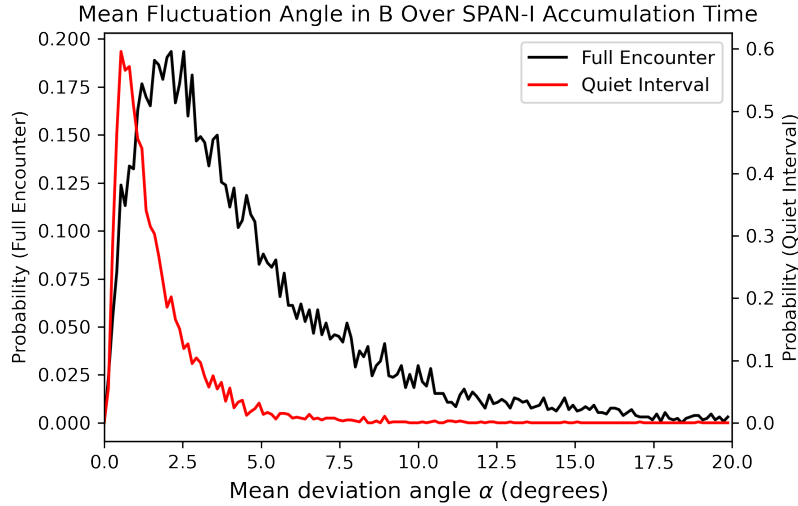
Figure 2.18: Histograms of the angular fluctuation in **B** during a single 3.5s SPAN-Ion measurement accumulation time, for the quiet interval in figure 2.17 (red), and for the full encounter (black).

The reason for a systematic offset in ϕ is most likely due to imperfect knowledge of the MCP efficiencies. Given that the peak of the VDF is almost always between anodes 1 and 2, a slight overestimate (say) of the efficiency of anode 1 would have the effect of slightly rotating the peak of the distribution towards anode 1, resulting in a systematic shift in measured ϕ. In future it may be possible through careful calibration to mitigate and reduce this by taking advantage of the fact that (as we shall discuss in Chapter 3) the bulk motion of the solar wind flow during Alfvénic fluctuations can be well understood as rotations about a fixed point in velocity space. Thus, if one is careful in choosing intervals where the fluctuations cause the distribution to rotate across ϕ with little to no change in θ, the incompressible nature of the fluctuations should mean that the density ρ doesn't change. Any *measured* change in ρ will then be due to incorrectly assigned MCP efficiencies. One can then attempt to "fit" to the MCP efficiencies in order to reduce the observed density fluctuations. In addition to this, there are small deviations in the instrument response that depend on anode which are not being taken into account here (see figure 6 in [101]).

Finally, to get an idea of how much **B** typically fluctuates during a SPAN-Ion accumulation time (point 4 above) and whether or not it's significant, we can use one of the higher cadence FIELDS data products. The 4 samples per cycle data product consists of 16 magnetic field measurements per SPAN-Ion accumulation time. For each SPAN-Ion measurement at time t_i, we calculate the mean of the angle $\alpha = \cos^{-1}(\hat{\mathbf{B}}_0 \cdot \hat{\mathbf{B}}(t))$ where $\hat{\mathbf{B}}_0$ is the unit magnetic field measured at time t_i and $\hat{\mathbf{B}}(t)$ consists of all FIELDS measurements with $t_i < t < t_{i+1}$. Results are shown in the histograms in figure 2.18. (The full encounter black curve is composed of 1000 randomly chosen SPAN-Ion measurements from each day

of the encounter.) The relative quietness of the interval in figure 2.17 compared to the rest of the encounter is clearly seen, with median deviation $\alpha = 1.3°$ compared to $\alpha = 3.6°$. We also note the large right hand tail of the full encounter distribution; there are a a significant number of measurement intervals where the magnetic field is fluctuating 7° or more. As mentioned, by definition these represent lower bounds on the uncertainty in the direction of **B** derived from any given VDF measurement. Such large fluctuations in **B** will mean significant smearing of the VDF over adjacent SPAN-Ion phase space bins, and, together with greater FOV occlusion either side of perihelion, will result in much larger disagreements $\Delta\theta, \Delta\phi$ than those obtained in figure 2.17.

This issue of velocity space "smearing" and its effect in particular on $T_\perp$ and $T_\parallel$ was addressed in [113], using measurements from SWE, Wind's Faraday Cup instrument [131]. The authors developed fitting routines that incorporated the on-board high cadence magnetic field measurements, as opposed to down-sampled averaged field vectors. While their technique wouldn't be applicable to the temperature tensor method described above (because moments are computed independently of **B**), it would be completely applicable were we deriving the direction of **B** via first fitting the counts spectra with a bi-Maxwellian, and then computing its principle axes. The essence of the method when applied to SPAN-Ion is simply to restore the implicit time dependence of phase space elements $\mathbf{v}(\theta_i, \phi_j, E_k) \to \mathbf{v}(\theta_i(t), \phi_j, E_k(t))$ where t indexes the substeps as energy E_k and angle θ_i are swept through. Then, wherever a dot product appears in the bi-Maxwellian, you ensure each element of **v** is dotted with the "correct" (in time) value of $\mathbf{B}(t)$. The authors noted significantly improved values of the temperature anisotropies as a result of this technique, thus showing the smearing effect to be reduced.

2.5 Summary

In this chapter we have discussed the general operating principles of ESAs, and given details of SPAN-Ion's energy and angle measurement ranges, TOF stage, and relevant data products. There followed an overview of how the distribution function and its moments are calculated from the raw counts measurements, and a discussion of the *intrinsic* uncertainties inherent in these expressions due to statistical (Poisson) and quantisation (compression) noise. We showed that for the pseudo-log compression applied to the SPAN-Ion counts spectra, Poisson noise is usually dominant, and the percentage error due to compression doesn't exceed $\approx 3\%$. It was also shown that these intrinsic errors result in scaling dependencies in the density and velocity uncertainties ($\delta n \sim n$ and $\delta V \sim 1/n$). This is able to be observed in real measurements, where the level of the noise-floors in density power spectra is seen to strongly depend on the density of the plasma itself, a fact not usually appreciated in discussion of power spectra noise floors. We then moved on to discuss partial moments, or the effect that the finite FOV of SPAN-Ion has on the density, velocity, and temperature measurements. As expected, the y components of both the velocity and the temperature tensor are most severely affected, however we presented a workaround method for extracting good measurements of $T_\perp$

and $T_\parallel$ from the temperature tensor $\mathbf{T}$, presuming the VDF is gyrotropic and well described by two temperatures only. Finally, we concluded with an examination of how well SPAN's VDF measurements are aligned with $\mathbf{B}$, which is useful as a tool for diagnosing potential systematic errors in the instrument. After selecting what should be an ideal measurement interval for SPAN, we showed that measurements of $\mathbf{T}$ were very well aligned with $\mathbf{B}$ in the θ direction, while a small systematic offset in $\phi \approx 4°$ appears to be present.

Chapter 3

Cross Helicity Reversals In Magnetic Switchbacks

Michael McManus, Stuart Bale, Trevor Bowen, Alfred Mallet, Davin E. Larson, Christopher H. K. Chen, Benjamin D. G. Chandran, Thierry Dudok de Wit, J. C. Kasper, Michael Stevens, Phyllis Whittlesey, Roberto Livi, Kelly E. Korreck, Keith Goetz, Peter R. Harvey, Marc Pulupa, Robert J. MacDowall, David M. Malaspina, Anthony W. Case, J. W. Bonnell

3.1 Abstract

We consider 2D joint distributions of normalised residual energy $\sigma_r(s,t)$ and cross helicity $\sigma_c(s,t)$ during one day of Parker Solar Probe's (PSP's) first encounter as a function of wavelet scale s. The broad features of the distributions are similar to previous observations made by HELIOS in slow solar wind, namely well correlated and fairly Alfvénic, except for a population with negative cross helicity which is seen at shorter wavelet scales. We show that this population is due to the presence of magnetic switchbacks, brief periods where the magnetic field polarity reverses. Such switchbacks have been observed before, both in HELIOS data and in Ulysses data in the polar solar wind. Their abundance and short timescales as seen by PSP in its first encounter is a new observation, and their precise origin is still unknown. By analysing these MHD invariants as a function of wavelet scale we show that MHD waves do indeed follow the local mean magnetic field through switchbacks, with net Elsasser flux propagating inward during the field reversal, and that they therefore must be local kinks in the magnetic field and not due to small regions of opposite polarity on the surface of the Sun. Such observations are important to keep in mind as computing cross helicity without taking into account the effect of switchbacks may result in spurious underestimation of σ_c as PSP gets closer to the Sun in later orbits.

3.2 Preface

In this chapter we reproduce a paper I wrote that appeared in the special issue dedicated to PSP early results, *Astrophysical Journal Supplement Series - Results from Parker Solar Probe: Ushering a New Frontier in Space Exploration* (Volume 246, Number 2) [122]. At this early stage of the mission (we use data from PSP's first encounter E1), the SPAN-Ion moments and fitting routines were still under active development, so we use particle measurements made by SPC. In addition, a configuration error in SPAN-Ion's energy table during E1 meant that the energy range was incorrectly set to be too narrow, severely truncating the measurements of the ion VDFs (in addition to the normal angular FOV occlusion expected during these early encounters).

While there was a great deal of excitement at the time regarding the sheer number of magnetic switchbacks seen in the magnetic field measurements first sent back by PSP, switchbacks were not the initial motivation for this study. Rather, the aim had been to examine the radial evolution of the MHD invariants cross-helicity σ_c and residual energy σ_r, compare them to earlier measurements made by Helios and Wind at 0.3AU and 1AU respectively, and use them to characterise the type of wind we were seeing in E1. However, the appearance of the negative cross-helicity measurements immediately stood out, and so the emphasis shifted to using frequency representations of σ_c and σ_r to probe the ion scale Alfvénic fluctuations, showing that they travel "backwards" in switchbacks due to the folding of the magnetic field. This then led very naturally on to the work we discuss in Chapter 3, where we study the ion motion in switchbacks in greater detail and make full use of the SPAN-Ion measurements.

3.3 Introduction

Parker Solar Probe (PSP) [53] was launched in August 2018 with the aim of shedding light on the plasma and magnetic field environments of the inner heliosphere and the longstanding problem of coronal heating. It completed its first of a series of 24 encounters on November 11th 2018, during which at perihelion it was a distance of $35R_S$ from the Sun.

One of the more notable observations reported from the first encounter has been the preponderance of so called magnetic "switchbacks", large traversals of the mainly radial magnetic field, often temporarily reversing the sense of the field. Prior to Parker Solar Probe, magnetic switchbacks had been observed both in near-Sun (0.3AU) HELIOS data [73], and over the solar poles by Ulysses [15]. Both studies involved fast solar wind streams. After reprocessing HELIOS data, [73] found that large velocity spikes are ubiquitous in near-Sun fast solar wind, occurring about 5% of the time and with magnitudes of order $0.5v_A$ above the background solar wind speed. The velocity spikes they observed were almost always positive speed enhancements, were highly Alfvénic in all three components (thus by necessity accompanied by large magnetic field traversals), and showed no statistically meaningful difference in plasma parameters inside versus outside the spikes (making it unlikely that

the observed field geometry was due to HELIOS crossing large coronal loops). The authors speculated that they may be the Alfvénic fluctuations that travel ahead of jets generated by reconnection events in the corona [81, 165], and are thus signatures of transient events at the Sun's surface that have survived to relatively large distances. The spikes or switchbacks seen by PSP in its first two encounters are qualitatively different than these in two ways; they are shorter in timescale (presumably due to being at smaller heliocentric distances and having better measurement cadences able to resolve sharper spikes), and they are the first direct observation of them in slow as opposed to fast solar wind, marking them to be a universal feature of the solar wind.

Earlier work by [15] reported magnetic field inversions at high heliographic latitudes that lasted on the order of several hours, and used cross helicity as a sensor of wave propagation direction to deduce that the inversions they saw were not intrinsically different magnetic sectors but rather due to fold-like structures in the magnetic field. In this work we use wavelet representations of the dimensionless MHD transport ratios cross helicity, σ_c, and residual energy, σ_r, in a similar way to probe the geometry of the short timescale magnetic switchbacks seen by PSP in encounter 1 over a wide range of scales. We deduce that they too are due to localised folds in the magnetic field and not regions of different magnetic polarity.

Several other sensors can be used to elucidate local magnetic field topology. Electron strahl pitch angle distributions, as measured by the SPAN instrument on PSP [179, 101], are used by [178] to follow the magnetic field through switchbacks. [129] showed that the relative proton core-beam drift becomes negative (that is, the beam appears to be moving more slowly than the core in the spacecraft frame), whenever the local field switches back on itself, and [188] used the alpha-proton differential velocity to show the same thing within the context of pressure balance structures. Our technique has the advantage of being somewhat less complex than these methods, requiring less detailed analysis of the particle distribution functions (only the perturbed bulk velocity moments are needed). It is worth mentioning that the wavelet method of analysing MHD transport ratios employed here is a very versatile one, and can be used to identify other structures in the solar wind. [190] use a similar technique to identify and catalog small-scale flux ropes (SFRs) during and around PSP's first encounter.

This clear dependence of plasma properties on the local magnetic field is reflected in the plasma turbulence as well. Turbulent power is concentrated at near perpendicular angles θ_{BV} between the magnetic field and flow direction, and the magnetic field spectral index is a smoothly increasing function of θ_{BV} [71, 142, 35]. This dependence of spectral index on θ_{BV} was only revealed when sufficient care was used to examine the mean field at small enough (i.e. localised) scales, via a wavelet method.

Throughout the solar wind we see Alfvénic turbulence, and there are numerous models of how this turbulence behaves both at 1AU [21, 104] and in the inner heliosphere [167, 32, 136]. The relationship between σ_c and σ_r, as useful invariants to characterise the state of the MHD turbulence, has been well studied ([29], [30] and references therein). Fast wind at short heliocentric distances is very Alfvénic and equipartitioned ($\sigma_c \sim 1, \sigma_r \sim 0$), but a second population with $\sigma_c \sim 0, \sigma_r \sim -1$ appears as heliocentric distance increases, representing the presence of intermittent magnetic structures. The importance of negative residual energy

and intermittency and how it causes the magnetic field spectrum to steepen was highlighted in [26] and [36]. Slow wind does not show such marked radial evolution, with broader (σ_c, σ_r) distributions in general.

In section 2 we outline the data set and methods used, section 3 contains results and discussion, and we briefly summarise the conclusions in section 4.

3.4 Data and Methods

We use particle measurements of proton density ρ and velocity $\mathbf{v}$ made by PSP's onboard Faraday cup, Solar Probe Cup (SPC) [84], and magnetic field measurements made by the FIELDS fluxgate magnetometer [14]. We consider a 1 day interval from encounter 1, Nov 5th 2018.

The encounter 1 measurement cadence for SPC proton moments is approximately 0.87s, while the magnetometer measurement frequency was approximately 293Hz. The magnetometer data was downsampled to match SPC's measurement cadence, and an approximately 2.6s timing offset corrected for. Large unphysical spikes were also removed, and any data gaps linearly interpolated over. Figure 1 shows particle and magnetic field data for this interval.

Throughout the analysis we make use of wavelet transform representations of various quantities. A wavelet transform of a discrete time series $x(t_i)$ is defined as [162, 1]

$$W(s,t) = \sum_{i=0}^{N-1} x(t_i)\psi\left(\frac{t_i - t}{s}\right) \tag{3.1}$$

where $W(s,t)$ is the wavelet coefficient at scale s and time t, $\psi(t,s)$ the wavelet function and $\{t_i\}$ the set of measurement times. We use a Morlet wavelet [44] as our wavelet function (written here unnormalised),

$$\psi(t) = \pi^{\frac{1}{4}} e^{-\frac{1}{2}t^2} e^{i\sigma t}, \tag{3.2}$$

where σ is an adjustable parameter taken here to be 6 that represents the frequency of the wavelet. We convert from dilation scale s to physical (spacecraft) frequency f using

$$f = \frac{\sigma}{2\pi\Delta t s} \tag{3.3}$$

where Δt is the measurement cadence. In this work we use 24 logarithmically spaced wavelet scales s, from $s_{\min} = 2$ to $s_{\max} = 5792.62$.

First, we compute a scale and time dependent local mean magnetic field $\mathbf{B}_0(s,t)$ as

$$\mathbf{B}_0(s,t) = \sum_{i=0}^{N-1} \mathbf{B}(t_i)\left|\psi\left(\frac{t_i - t}{s}\right)\right|, \tag{3.4}$$

where the kernel $|\psi|$ is normalised to unity at each scale s, similar to [71], [142]. This convolution of $\mathbf{B}(t)$ with $|\psi|$ can be intuitively understood as a smoothing of $\mathbf{B}(t)$ over a
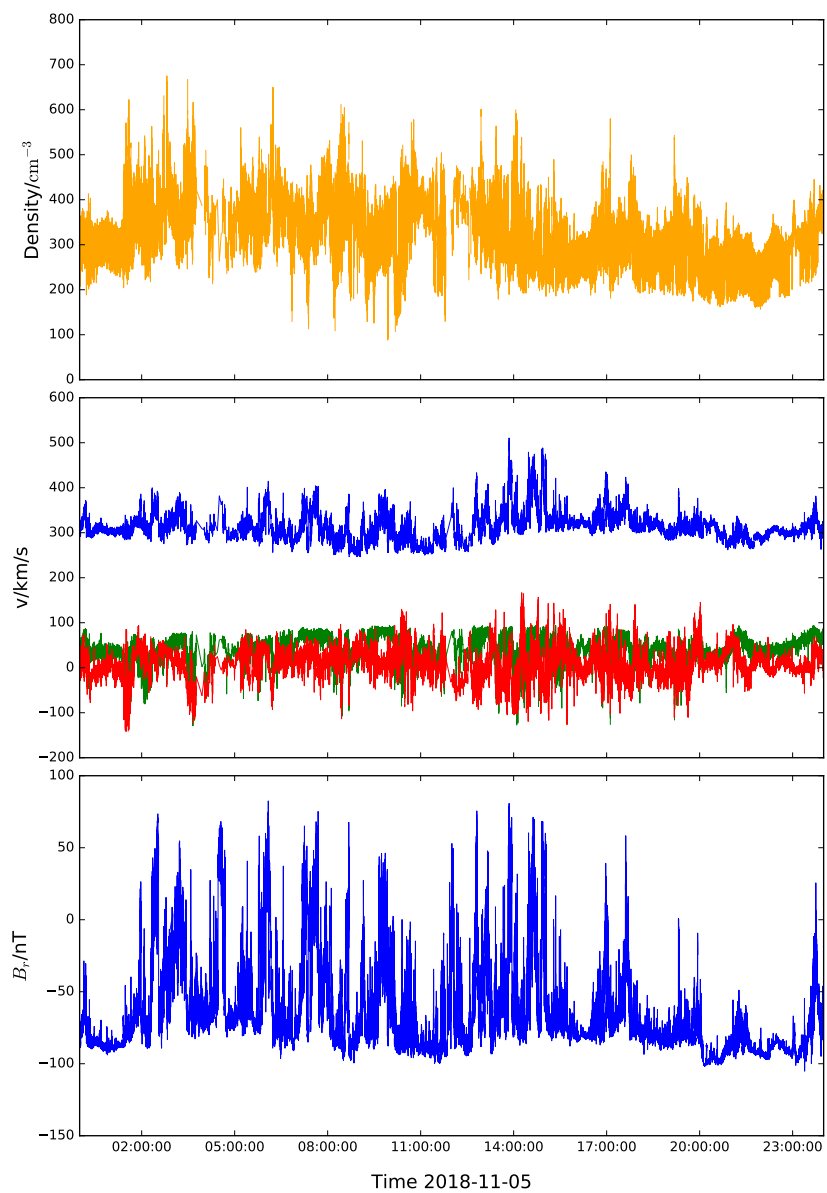
Figure 3.1: Time series of the encounter 1 interval. Top panel shows proton density, middle panel shows proton velocity moments in RTN coordinates from SPC (blue, green, red being radial, tangential, normal respectively), and the bottom panel shows radial component of the magnetic field.
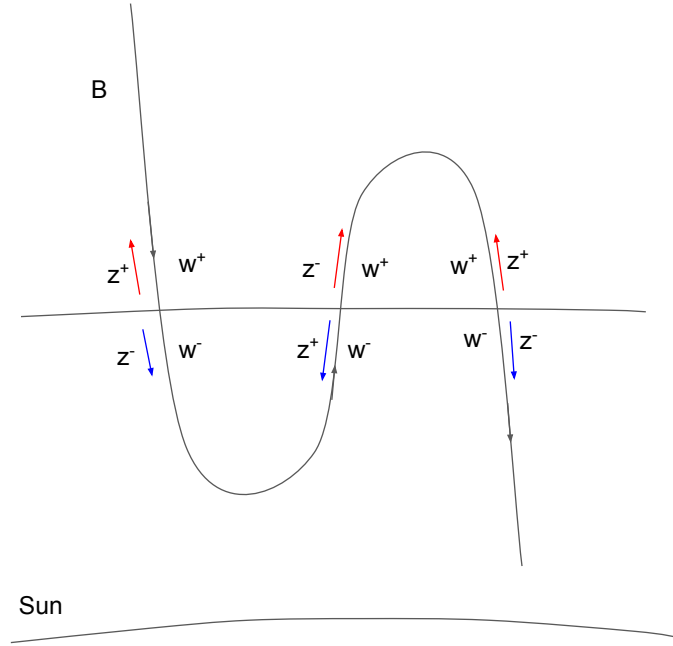
Figure 3.2: Schematic of a possible topology of a magnetic switchback, showing the redefinition of $\delta\mathbf{w}_\perp^\pm$ in terms of $\delta\mathbf{z}_\perp^\pm$ when B_r changes sign.

window whose size is determined by the width of the Morlet wavelet's Gaussian envelope, $|\psi|$, which in turn is set by the scale length s. We then apply the wavelet transform 3.1 to the time series $\mathbf{v}(t)$ and $\mathbf{b}(t)$, which gives us the scale and time dependent fluctuations $\delta\mathbf{v}(s,t)$ and $\delta\mathbf{b}(s,t)$ (since the wavelet transform has no zero frequency component). With 3.4 a local parallel field direction is defined, from which we can calculate the wavelet representations of the perpendicular fluctuations $\delta\mathbf{v}_\perp(s,t)$ and $\delta\mathbf{b}_\perp(s,t)$, and the perpendicular Elsasser variables

$$\delta\mathbf{z}_\perp^\pm(s,t) = \delta\mathbf{v}_\perp(s,t) \pm \delta\mathbf{b}_\perp(s,t). \tag{3.5}$$

Here $\delta\mathbf{b}_\perp(s,t)$ is measured in Alfvén units. To convert we use a scale and time dependent density $\rho(s,t)$ computed using equation 3.4 applied to density,

$$\rho(s,t) = \sum_{i=0}^{N-1} \rho(t_i) \left| \psi\left(\frac{t_i - t}{s}\right) \right|. \tag{3.6}$$

It is usual in the solar wind literature [20, 19, 146] to define $\delta\mathbf{z}_\perp^\pm$ in such a way that $\delta\mathbf{z}_\perp^+$ and $\delta\mathbf{z}_\perp^-$ always refer to outward and inward going waves respectively, regardless of the direction of the background magnetic field. Since $\mathbf{z}_\perp^+$ and $\mathbf{z}_\perp^-$ wave packets travel anti-parallel/parallel to $\mathbf{B}_0$ respectively, a scheme of magnetic "rectification" is usually employed, flipping $\mathbf{B}_0$ as necessary. While this is useful when dealing with large scale magnetic sectors of different
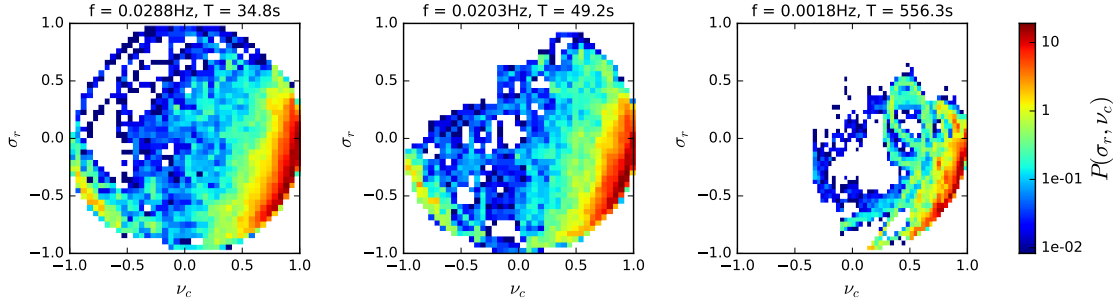
Figure 3.3: Joint probability distribution histograms of σ_r vs ν_c for one day of encounter 1 (2018-11-05) at three different wavelet scales, from left to right: $T = 35$s, $T = 49$s, $T = 556$s.

polarity, it will be much clearer in the following discussion to leave the definition of $\delta \mathbf{z}_\perp^\pm$ as is in equation 3.5, and define two new variables, $\delta \mathbf{w}_\perp^\pm$, to represent strictly outgoing $(+)$ and ingoing $(-)$ waves respectively:

$$\delta \mathbf{w}_\perp^\pm (s,t) = \begin{cases} \delta \mathbf{z}_\perp^\pm (s,t) & \text{if } \operatorname{sgn}\left(B_{0r}(s,t)\right) = -1 \\ \delta \mathbf{z}_\perp^\mp (s,t) & \text{if } \operatorname{sgn}\left(B_{0r}(s,t)\right) = 1 \end{cases} \tag{3.7}$$

where $B_{0r}(s,t)$ is the radial component (in RTN coordinates) of the scale dependent mean magnetic field defined in equation 3.4. Physically this is equivalent to the usual method of rectifying the field. The cartoon in Figure 3.2 illustrates these definitions for a situation where PSP observes a field polarity reversal in an overall radially inward background field. For illustration we have drawn this as an S-shaped bend, but a priori the exact field geometry is unknown.

   To define switchback times, we first compute the time average over the entire interval of the radial component of the background magnetic field, $\langle B_{0r}(s_{\max}, t)\rangle_t$, at the largest wavelet scale $s_{\max}$. We define the overall sense of the background magnetic field to be $\eta \equiv \operatorname{sgn}(\langle B_{0r}(s_{\max}, t)\rangle_t)$. At each wavelet scale then, we can define a magnetic inversion or switchback to be when $B_{0r}(s,t)$ changes sign, relative to this largest scale background magnetic field direction. In other words, when $B_{0r}(s,t) = -\eta$.

   With these definitions in hand we can compute the normalised residual energy

$$\sigma_r(s,t) = \frac{|\delta \mathbf{v}_\perp(s,t)|^2 - |\delta \mathbf{b}_\perp(s,t)|^2}{|\delta \mathbf{v}_\perp(s,t)|^2 + |\delta \mathbf{b}_\perp(s,t)|^2} \tag{3.8}$$

$$= \frac{2\delta \mathbf{z}_\perp^+(s,t) \cdot \delta \mathbf{z}_\perp^-(s,t)}{|\delta \mathbf{z}_\perp^+(s,t)|^2 + |\delta \mathbf{z}_\perp^-(s,t)|^2}, \tag{3.9}$$

which represents the imbalance between kinetic and magnetic fluctuations, or equivalently the alignment between the two Elsasser variables, and normalised cross helicity,

$$\sigma_c(s,t) = \frac{2\delta\mathbf{v}_\perp(s,t) \cdot \delta\mathbf{b}_\perp(s,t)}{|\delta\mathbf{v}_\perp(s,t)|^2 + |\delta\mathbf{b}_\perp(s,t)|^2} \tag{3.10}$$

$$= \frac{|\delta\mathbf{z}_\perp^+(s,t)|^2 - |\delta\mathbf{z}_\perp^-(s,t)|^2}{|\delta\mathbf{z}_\perp^+(s,t)|^2 + |\delta\mathbf{z}_\perp^-(s,t)|^2}, \tag{3.11}$$

representing the alignment between velocity and magnetic field fluctuations, or the imbalance between the flux of $\delta\mathbf{z}_\perp^+$ and $\delta\mathbf{z}_\perp^-$. By analogy we have the "rectified" cross helicity, constructed using $\delta\mathbf{w}_\perp^\pm$, which we will denote ν_c:

$$\nu_c(s,t) = \frac{|\delta\mathbf{w}_\perp^+(s,t)|^2 - |\delta\mathbf{w}_\perp^-(s,t)|^2}{|\delta\mathbf{w}_\perp^+(s,t)|^2 + |\delta\mathbf{w}_\perp^-(s,t)|^2} \tag{3.12}$$

(rectification does not affect σ_r). ν_c is therefore a sensor of ingoing vs outgoing Elsasser flux, with respect to the radial direction $\hat{\mathbf{r}}$, regardless of the direction of the mean magnetic field. It is helpful to think of σ_c as the fractional excess of fluctuations propagating anti-parallel to $\mathbf{B_0}$, and ν_c as the fractional excess of fluctuations propagating away from the Sun.

Equations 3.8, 3.10, and 3.12 impose the geometric constraint that

$$\sigma_c^2 + \sigma_r^2 \leq 1 \tag{3.13}$$

$$\nu_c^2 + \sigma_r^2 \leq 1, \tag{3.14}$$

i.e. points in (σ_c, σ_r) and (ν_c, σ_r) space are constrained to lie within a circle of radius 1. For a purely Alfvénic fluctuation, $\sigma_r = 0$ and $\nu_c = \pm 1$, with + representing an outgoing wave and − an ingoing one. Values of $|\nu_c| < 1$ represent either mixtures of ingoing and outgoing modes or mixtures of Alfvénic and non-Alfvénic fluctuations, two situations which cannot be distinguished by examining ν_c alone.

Finally, we define the inward and outward going Elsasser fluxes

$$e^+ = |\delta\mathbf{w}_\perp^+(s,t)|^2 \tag{3.15}$$

$$e^- = |\delta\mathbf{w}_\perp^-(s,t)|^2. \tag{3.16}$$

3.5   Results and Discussion

Figure 3.1 shows the day-long interval during encounter 1 used in this analysis. The solar wind speed is relatively low, $v_{\text{sw}} \approx 330$km/s (throughout encounter 1 PSP was connected mainly to the same equatorial coronal hole [8]), and the radial distance is $R = 0.17AU$. The bottom panel shows the radial component of the magnetic field. The overall sense of the magnetic field is radially inwards, but a forest of narrow, spiky switchbacks where B_r becomes positive are clearly visible. In Figure 3.3 we plot joint histograms of σ_r vs ν_c at three
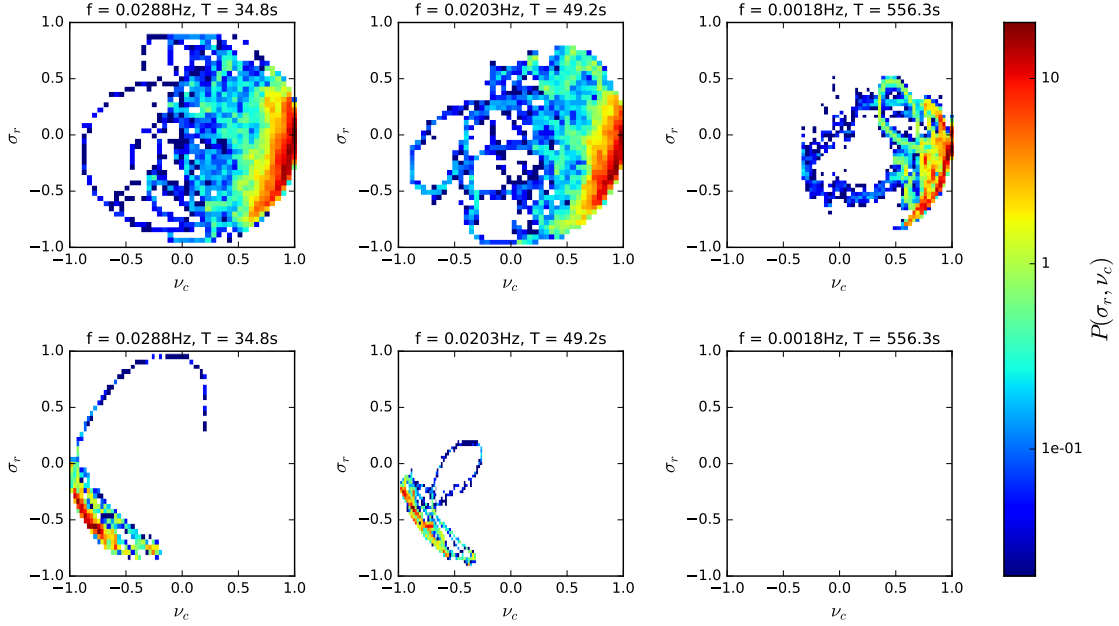
Figure 3.4: Joint probability distribution histograms of σ_r and ν_c at three different wavelet scales, from left to right: $T = 35$s, $T = 49$s, $T = 556$s, divided by θ_{Br}. Top row: only those times on when $\theta_{Br} > 160°$, corresponding to a mainly radial field. Bottom row: only times when $\theta_{Br} < 90°$, when the radial magnetic field has locally reversed.

different wavelet scales, two short ones (35s and 50s), and one relatively longer one (560s). These frequencies are all well above the SPC velocity moment noise floor, which in this case corresponds to a frequency $f \approx 0.12$Hz or scale $T \approx 8.3$s. All three histograms are strongly peaked in the bottom right quadrant, near the edge of the limiting circle, with maxima around $\nu_c \sim 0.9, \sigma_r \sim -0.3$, indicating highly aligned [180] and fairly Alfvénic fluctuations. Of interest is the clear signal of a "second population" at the two smaller scales, seen as a peak in the lower left quadrant with fewer counts and similar values of $\sigma_r \sim -0.3$ but with negative values of $\nu_c \sim -0.9$. No such population is seen at the longer 560s time scale (and indeed at any wavelet scale longer than this).

The physical origin of the negative cross helicity population can be easily understood. In Figure 3.4 we divide up the data according to θ_{Br}, the angle between the local magnetic field $\mathbf{B}_0(s, t)$ and the radial direction. The top row is histograms of σ_r vs ν_c but only including times for which $\theta_{Br} > 160°$ - a mainly radial field. The second row includes only times when $\theta_{Br} < 90°$, when the magnetic field has undergone a switchback.

The negative helicity population has clearly separated and is identifiable precisely with switchback intervals. This suggests that inside switchbacks MHD waves do indeed follow

the *local* magnetic field - the negative cross helicity values represent what was once majority outgoing waves becoming predominantly inward propagating inside a switchback (refer again to figure 3.2). This also implies that magnetic switchbacks are local kinks in the magnetic field and not due to small regions of opposite polarity at the surface of the Sun (in agreement with the conclusions in [178]). It is worth remarking here that by "inward propagating" we mean relative to the plasma frame, not the spacecraft frame, since the Alfvén velocity is much smaller than the solar wind speed. In addition, the range of wavelet scales over which we see the negative ν_c population, and the scale at which it disappears, tells us something about the characteristic scale of the switchbacks at 0.17AU. In these data, switchbacks appear to last on the order of $20 - 100s$, and their signature has completely disappeared at scales of $\approx 300s$ and longer (hence why the bottom right histogram in figure 3.4 is empty). This isn't to say switchbacks longer than this never occur. [182] present evidence that distributions of switchback deflections and residence times are power-law like, so the lack of a signature above 300s in our data set is more likely a finite sampling effect rather than a hard cutoff on the timescales of switchbacks. The conclusions reached here are also in agreement with [34], who applied an MHD mode decomposition technique and found that the dominant mode both inside and outside switchbacks is always the backward propagating shear Alfvén wave, implying inward propagating plasma frame waves during switchbacks and thus kinked magnetic field lines.

Joint probability distributions of σ_r and ν_c have been constructed many times before [29, 40, 19, 20] in a variety of solar wind conditions and heliospheric distances. In particular, [29] looked at slow wind using HELIOS 2 data at 0.32, 0.69, and 0.90AU. The features of their plots are broadly similar to ours (they remark there is little radial evolution in slow wind), but there is no sign of a negative cross helicity population similar to what is seen in figure 3.3. This is not because switchbacks have disappeared once you are at radial distances of 0.3AU or greater (indeed, they have been directly observed in HELIOS high speed solar wind data prior to PSP, [73]) but is a matter of scale. Given that the characteristic timescale of switchbacks at this radial distance of 0.17AU is on the order of tens of seconds, the hour long timescale used in [29] is, certainly at smaller heliospheric distances, far too long to observe the switchbacks. It is worth noting that [29] do observe a population of negative cross helicity at larger heliospheric distances but due to the large associated negative values of residual energy interpret it as being due to advected structures rather than inward propagating Alfvénic waves.

An alternative way of looking at this is shown in figure 3.5, where we plot (rectified) Elsasser power, $\log(e^-)$ vs $\log(e^+)$, at the same three wavelet scales and θ_{Br} regimes as in Figures 3.3 and 3.4. The diagonal dashed lines represent lines of constant cross helicity ν_c (from top left to bottom right, $\nu_c = -0.99, -0.8, 0.0, 0.8, 0.99$). Again, the negative cross helicity population is seen at the two shorter scales, but not the longer 560s time scale. Splitting the data up by θ_{Br} isolates the negative ν_c population to be due to switchbacks, when $\theta_{Br} < 90°$. Both the positive and negative ν_c distributions are strongly peaked along lines of constant ν_c.

Finally, in Figure 3.6 we show time series of B_r, and wavelet spectra of $\nu_c(f,t)$ and $\sigma_c(f,t)$
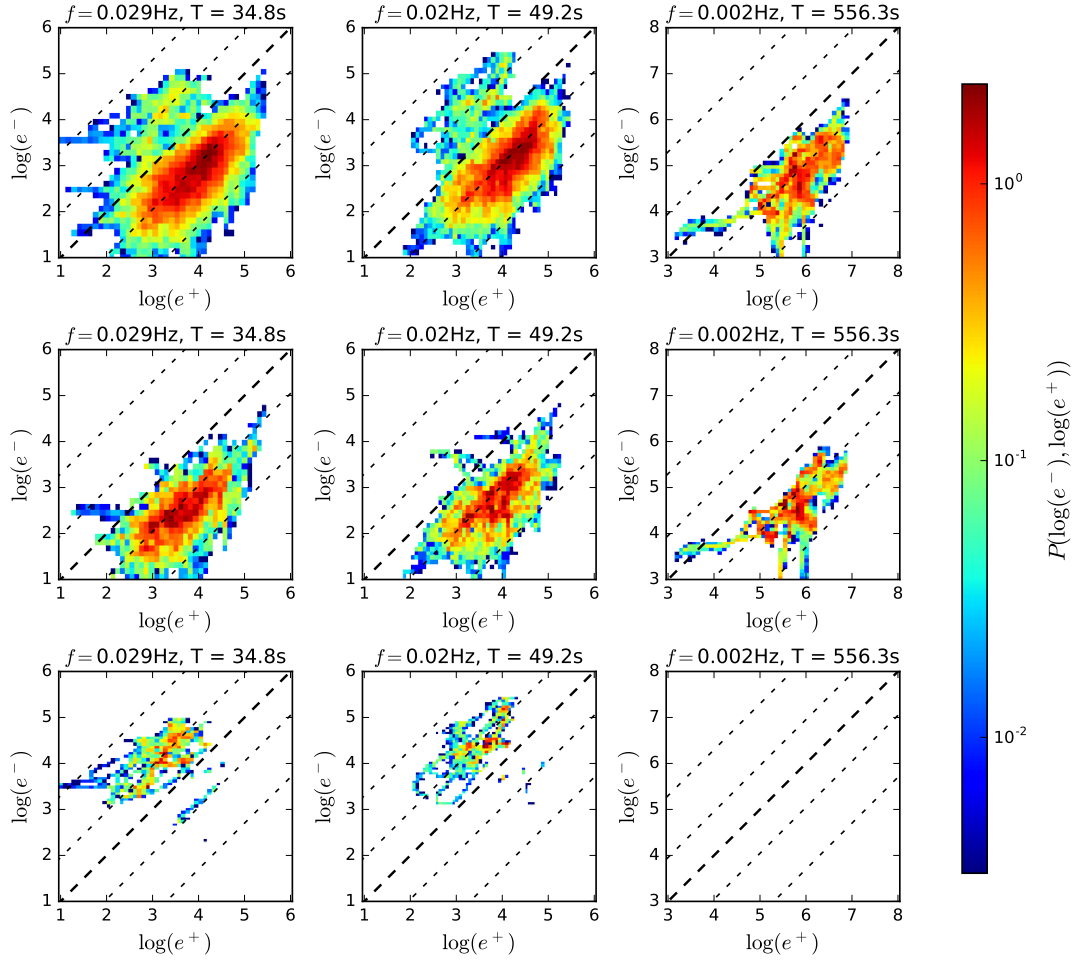
Figure 3.5: Joint probability distribution histograms of Elsasser power, $\log(e^-)$ vs $\log(e^+)$, at three different wavelet scales, $T = 35$s, $T = 49$s, $T = 556$s, and for the same regimes as in figure 3 (top row: all data, second row: $\theta_{Br} > 160°$, third row: $\theta_{Br} < 90°$). Dashed lines represent lines of constant positive (lower right) or negative (upper left) cross helicity.
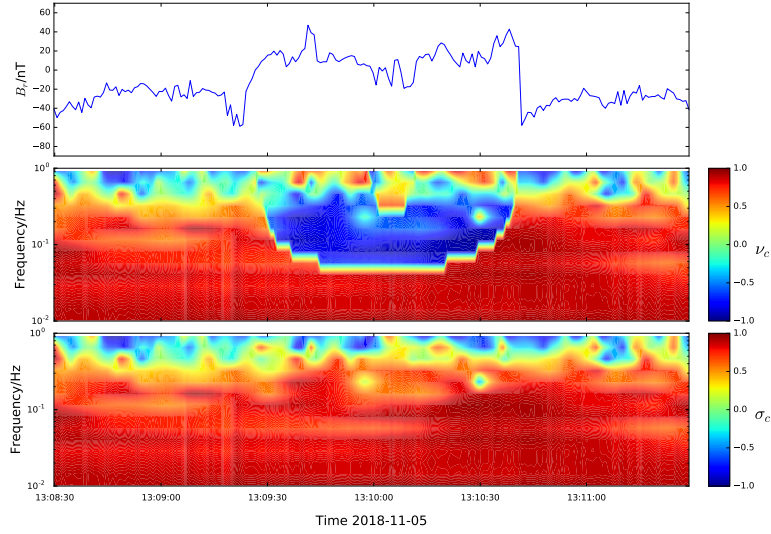
Figure 3.6: Behaviour of cross helicity through a magnetic switchback. Top panel shows the radial magnetic field. Middle panel shows the wavelet spectrum of rectified cross helicity, $\nu_c(f, t)$, as a function of frequency and time. Bottom panel shows the wavelet spectrum of cross helicity $\sigma_c(f, t)$.

through a single switchback. The reversal in sign of ν_c is clearly visible, further supporting the interpretation that the MHD waves are following local field lines at their own scale through the switchback. The region of the spectrogram with negative ν_c does not extend to all lower frequencies (the "stepped" appearance of the feature in the ν_c spectrogram is a visual artifact - it is effectively the cone of influence of the edge-like feature in the magnetic field). At frequencies $f \lesssim 4 \times 10^{-2}$ Hz, the local mean field no longer sees a field reversal because it has been smoothed over a time window that is sufficiently long compared to the time scale of the switchback. Writing $\mathbf{B}(s, t) = \mathbf{B}_0(s, t) + \delta\mathbf{B}(s, t)$, one can think of the switchback as having moved from the local mean field into the fluctuations at some sufficiently large scale, and so $\nu_c = \sigma_c$ at low frequencies.

Regarding the use of ν_c and σ_c effectively as probes of wave propagation direction, of course from Figure 3.6 one can come to the same physical conclusion by examining the behaviour of either ν_c or σ_c. One advantage however of ν_c over σ_c is that it gives us statistical information on the characteristic timescales of these events, whereas σ_c does not.

3.6 Conclusion

We have considered the 2D joint distributions of normalised residual energy $\sigma_r(s,t)$ and normalised rectified cross helicity $\nu_c(s,t)$ during one day of PSP's first encounter as a function of scale, s. The broad features of the distributions are similar to previous observations in the slow solar wind at small heliocentric distances [29], with highly correlated and Alfvénic fluctuations ($\nu_c \sim 0.9$, $\sigma_r \sim -0.3$), but at shorter scales a second population with $\nu_c < 0$ is observed.

We interpret this to be due to the presence of magnetic switchbacks, and confirm this by splitting the data up according to θ_{Br}, the angle between the scale dependent local mean magnetic field and the radial direction and observing the second population to only appear during switchback times. We conclude that MHD waves are following the *local* magnetic field inside switchbacks, even when it undergoes a large traversal. Predominantly outward propagating flux briefly becomes inward propagating during the field reversal. This also implies that these are local kinks in the magnetic field, and not due to regions of opposite polarity at the Sun's surface. Our analysis provides a useful way to distinguish between these scenarios using only in situ data. σ_c, as a measure of correlation between $\delta\mathbf{v}_\perp$ and $\delta\mathbf{b}_\perp$ is unaffected by the local mean field direction, showing that the switchbacks are just as Alfvénic as the surrounding wind and so switchbacks are in some sense an intrinsic part of it. Propagation direction, as encoded by ν_c, *is* sensitive to the local mean field direction - that is it follows it. This interpretation is further confirmed by directly looking at Elsasser flux inside and outside switchbacks, and a case study following $\nu_c(f,t)$ as a function of time through a single switchback. Computing averaged values of rectified cross helicity without taking into account the reversal effect of switchbacks may result in underestimation of ν_c, an effect which may become more important in later PSP orbits, depending on how the distribution of switchbacks change closer to the Sun.

Finally, a wavelet representation of rectified cross helicity $\nu_c(s,t)$ is seen to be a useful tool for directly observing the inward travelling flux during a large polarity reversing switchback, as well as providing statistical information about the characteristic time scales of switchbacks, which we observe to be in the range 20-100s during this interval.

Chapter 4

Density And Velocity Fluctuations of Alpha Particles in Magnetic Switchbacks

4.1 Abstract

Magnetic switchbacks, or sudden reversals in the magnetic field's radial direction, are one of the more striking observations of Parker Solar Probe (PSP) thus far in its mission. While their precise production mechanisms are still unknown, the two main theories are via interchange reconnection events and in situ generation. In this work density and abundance variations of alpha particles are studied inside and outside individual switchbacks. We find no consistent compositional differences in the alpha particle abundance ratio, $n_{\alpha p}$, inside vs outside, nor do we observe any signature when separating the switchbacks according to $V_{\alpha p}/V_{pw}$, the ratio of alpha-proton differential speed to the wave phase speed (speed the switchback is travelling). We argue these measurements cannot be used to rule in favour of one production mechanism over the other, due to the distance between PSP and the postulated interchange reconnection events. In addition we examine the 3D velocity fluctuations of protons and alpha particles within individual switchbacks. While switchbacks are always associated with increases in proton velocity, alpha velocities may be enhanced, unchanged, or decrease. This is due to the interplay between V_{pw} and $V_{\alpha p}$, with the Alfvénic motion of the alpha particles vanishing as the difference $|V_{pw} - V_{\alpha p}|$ decreases. We show how the Alfvénic motion of both the alphas and the protons through switchbacks can be understood as approximately rigid arm rotation about the location of the wave frame, and illustrate that the wave frame can therefore be estimated using particle measurements alone, via sphere fitting.

4.2 Preface

In this chapter we reproduce a paper I published in *The Astrophysical Journal*, Volume 933, Number 1, with the addition of figures 4.6 and 4.7, and relevant discussion. At this stage of the mission, full fitting (and moment) routines for SPAN-Ion had been developed by myself and other members of the SPAN team at Berkeley. In particular, I had done a lot of work on fitting the alpha particle SF01 spectra, to take into account the small number of protons that were leaking in and mistakenly being counted as alpha particles.

Building on the work presented in Chapter 2, this paper focusses on two main things. The first is a discussion and an attempt to answer the question of whether switchbacks are generated in situ as the solar wind travels outwards, or whether they are generated by processes in the corona such as interchange reconnection. The second expands on previous work by [116, 115] and [62], among others, regarding a geometrical picture that can be used to understand Alfvénic fluctuations in the solar wind. Regardless of how they got there, switchbacks can essentially be regarded as single, very large amplitude spherically polarised Alfvén waves, and so they served as ideal testbeds for the geometrical model in [116, 115], where different ion species in the solar wind all rotate around the "wave frame" in velocity space, and this then explains the magnitudes and signs of their respective velocity fluctuations seen in time series measurements. The quality of SPAN-Ion alpha particle measurements allowed us to directly observe the spherical polarisation of the alpha particles for the first time, and use them to deduce the location of the wave frame purely from particle measurements and independently of the protons. This should be contrasted with previous work on the topic of the wave frame and the behaviour of heavier ions, which used more statistical approaches [125].

4.3 Introduction

One of the more striking results of Parker Solar Probe's (PSP, [53]) mission thus far is the ubiquity, in the near-Sun solar wind, of magnetic switchbacks - large, sudden rotations of the magnetic field, accompanied by spikes in the radial solar wind velocity. While switchbacks have previously been observed both in the inner heliosphere using Helios measurements [23, 73], and at 1AU and beyond [80, 129], these recent PSP observations have sparked renewed interest in their nature and origins.

4.3.1 Properties

Switchbacks (hereafter SBs) are long, thin [93, 72], S-shaped [122] magnetic structures, most likely oriented along the magnetic field direction [93]. They are mostly Alfvénic in nature, with constant magnitude $|\mathbf{B}|$ field corresponding to the condition of spherical polarisation. The Alfvénic correlations between $\mathbf{B}$ and $\mathbf{v}$ mean that the field rotations of SBs are accompanied by large positive spikes in the proton velocity, regardless of the underlying polarity

of the magnetic field [116]. They don't occur continuously but rather appear in "patches" [11, 182], separated by periods of quiet, steady flow and radial magnetic field. The proton core temperature appears unchanged within individual SBs [186, 112], however the patches themselves appear to be overall hotter than the quiet interstitial periods [183, 10].

4.3.2   SB Formation Theories

The question of what mechanisms are responsible for switchback generation is still an open one. Several ideas have been put forward, generally coming in two main flavours; the first involves generation via magnetic reconnection. [52] postulate that due to large scale equatorial circulation of the photospheric magnetic field, open magnetic field lines are dragged across closed loops at lower latitudes, causing interchange reconnection events which launch S-shaped kinks into the corona. [189] describe a similar idea but with the reconnection occurring significantly higher up in the corona and launching fast magnetosonic type modes both up and down the open field lines.

An alternative idea is that switchbacks naturally form in the solar wind as it expands and travels outwards. Magnetic field fluctuations decay more slowly with radial distance R than the mean magnetic field does, resulting in normalised amplitudes of Alfvénic fluctuations increasing as a function of R. This means that out of the bath of initially small amplitude, linear Alfvén waves known to be present at the base of the corona, the normalised fluctuation amplitudes grow as the plasma travels outwards until they eventually become large enough to cause the field to switch back on itself. [105] develop an analytical model of such large-amplitude Alfvén waves in an expanding solar wind and make several testable predictions for the properties of the SBs produced, and similar results have been found via MHD simulations [153, 152]. in situ generation of SBs then very naturally explains the observation that the SB filling fraction increases as a function of radius [9, 124, 103], something that is difficult to explain for theories involving a purely low coronal origin. It would also explain switchback "patches" as corresponding to wind that has undergone greater expansion in transit; [10] provide strong evidence that at least some of the patches observed by PSP so far are due to superradially expanded wind originating from the boundaries of supergranules at the solar surface.

Recent analysis of Ulysses, Helios and PSP data by [159] however suggests that the scaling of SB occurrence as a function of radial distance R in fact depends on the size or duration of the switchback, with shorter duration SBs decaying with R and longer ones persisting. This, along with the non-uniform properties of SBs (wide range of durations [182], some exhibiting compressibility while most do not [91], different types of discontinuity at the boundaries [96], etc) could be evidence that both types of generation mechanism are occurring, and we are seeing a combination of short-duration SBs naturally decaying via processes like parametric decay within a few tens of solar radii [160], while in situ generation is replenishing the population of longer duration SBs. At this stage this is still speculative and there are many open questions regarding the formation, evolution and eventual decay of SBs.

For completeness we mention that there are other potential SB generation mechanisms unrelated to the two just described. [149] suggest they may be associated with the onset of shear-driven turbulence at or above the Alfvén critical surface. Velocity shears between adjacent flux tubes can then potentially be large enough to trigger the onset of Kelvin-Helmholtz type instabilities and their associated vorticity roll-ups, producing the large deflections in **B** that we observe as SBs. [150] also postulate that SBs are produced by shear interactions between fast and slow streams above the Alfvén surface (when ram pressure becomes dominant), in particular pointing out that this should occur in the super-Parker spiral type magnetic fields produced by footpoint motion across the leading edges of coronal holes.

In this paper we focus on one small piece of the picture, namely the behaviour of alpha particles inside vs outside individual switchbacks, and whether or not this can help distinguish between any potential generation mechanisms.

4.4 Methods

4.4.1 Data

For this study we focus on PSP's third and fourth encounters (E3 and E4) from Aug 27th to Sep 8th, and 2019 and Jan 23rd to Feb 3rd, 2020, respectively. We use data from the FIELDS magnetometers [14] for high resolution magnetic field **B** measurements and downsample to match particle measurement cadences as needed. 3D ion velocity distribution function (VDF) measurements are taken from the SPAN-Ion electrostatic analyser [101, 84], with proton and alpha counts spectra produced at cadences of 7s and 14s respectively. To the proton channel spectra we fit a bi-Maxwellian to both the core and beam populations, with the proton beam constrained to lie along the magnetic field relative to the core velocity. The alpha channel contains a small (2%) contamination from the proton channel, which manifests as scaled down proton core and beam VDFs in the alpha channel. This was accounted for by taking the previously fitted proton parameters and reducing the density down to fit the extraneous protons. An additional single bi-Maxwellian was then fit to the alpha part of the spectrum and the core alpha particle VDF parameters extracted. The $\sim 2\%$ scaling factor is a free parameter in the fit; it was checked that there was no energy or angle dependence in the contaminant protons so that an overall scaling was sufficient. The uncertainties on the fitted alpha densities are approximately 10%.

We will on occasion require proton density measurements. For this we use quasi-thermal noise (QTN) estimates derived from extraction of the plasma line from FIELDS RFS spectra [147], and approximate $n_e = n_p + 2n_\alpha \approx n_p$, as the alpha abundance in PSP's early encounters is very low [185].

4.4.2 Switchbacks

Our dataset of SBs consists of 92 examples chosen by visual inspection from E3 and E4. Using SPAN-Ion data as the source of our ion measurements means we are constrained by the alpha particle 14s measurement cadence to selecting relatively longer SBs, and so cannot use quite as large an event database as in some previous studies [112]. Following [112] we split each SB into five distinct regions: Leading Quiet (LQ), the relatively quiescent period immediately preceding the switchback; Leading Transition (LT), the transition corresponding to the rotation of the magnetic field; Switchback (SB), the interior of the switchback structure; Trailing Transition (TT), the second transition, and finally the Trailing Quiet (TQ) region, the quiescent field immediately following the passing of the SB. In this work we are mainly interested in comparing the quiescent "background" conditions to the interior of the switchback, rather than the transition regions which represent the edges of the magnetic structure (and display a host of interesting physics, including signatures of reconnection [54] and wave activity [2, 91]). Figure 4.1 shows a prototypical example SB, with the five regions indicated with vertical dashed lines.
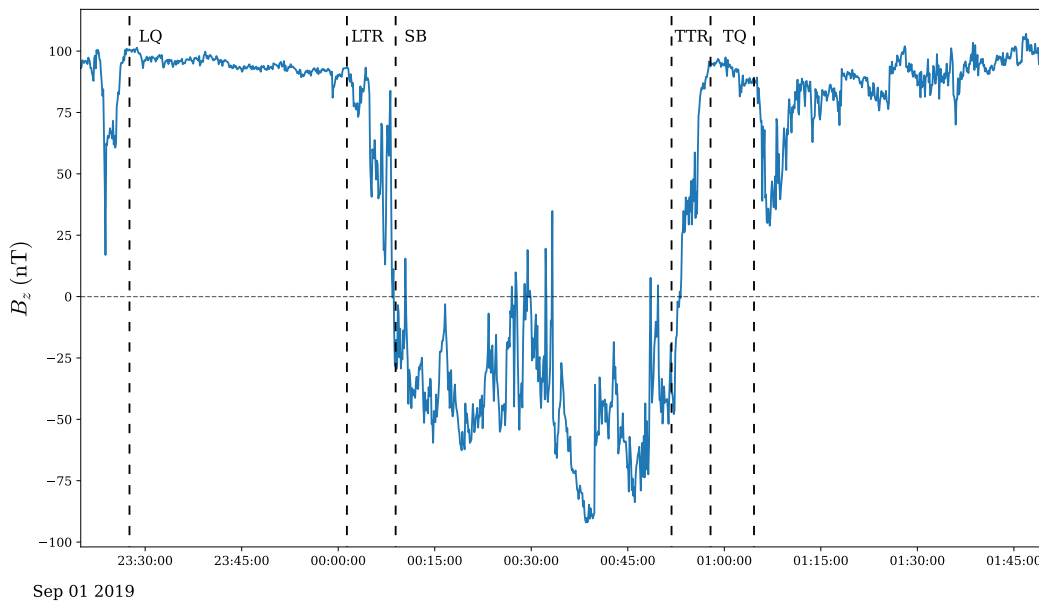
Figure 4.1: Z-component (in PSP spacecraft coordinates) of the magnetic field for a typical switchback, showing the demarcation of different regions: Leading Quiet (LQ), Leading Transition Region (LTR), Switchback interior (SB), Trailing Transition Region (TTR), and Trailing Quiet (TQ).
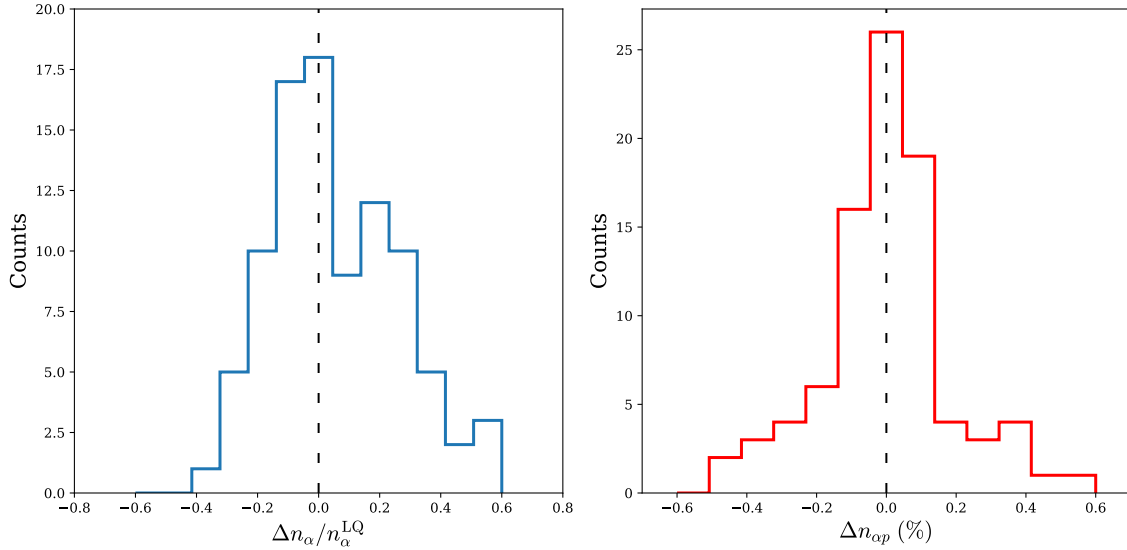
Figure 4.2: Histograms of fractional change in alpha density between switchback interiors
and their leading quiet regions (left), and the change in alpha abundance n_α/n_p between the
same two regions.

4.5 Results and Discussion

4.5.1 Density and Abundance Changes

The left plot in figure 4.2 shows a histogram of the fractional change in alpha number density
between SB interiors and their leading quiet (LQ) regions, $(n_\alpha^{\mathrm{SB}} - n_\alpha^{\mathrm{LQ}})/n_\alpha^{\mathrm{LQ}}$. While the spread
in fractional density changes is quite large, the mean (and median) of $\Delta n_\alpha/n_\alpha^{\mathrm{LQ}}$ are both very
close to zero (0.05 and 0.02 respectively). This is qualitatively very similar to the proton
fractional density changes in SBs reported both in observations and simulations (see Figure
4 of [96] and Figure 10 of [152] respectively).

   The histogram on the right in figure 4.2 shows the change in alpha abundance $\Delta n_{\alpha p} =
n_\alpha^{\mathrm{SB}}/n_p^{\mathrm{SB}} - n_\alpha^{\mathrm{LQ}}/n_p^{\mathrm{LQ}}$ between the same two regions (note that although one might have
$\langle \Delta n_p \rangle \approx 0$ and $\langle \Delta n_\alpha \rangle \approx 0$, a priori they need not be statistically independent). For proton
densities we do not use SPAN-Ion measurements of n_p, but rather estimates of n_p from
FIELDS QTN measurements as detailed in section 2. The large $\delta\mathbf{V}$ associated with SBs
often moves the proton VDF significantly out of SPAN-Ion's field of view (FOV), which
results in a large (unphysical) proton density decrease as measured by SPAN. While fitting
does mitigate the problem somewhat, it is often not enough to completely eliminate these
instrumental density decreases. Using SPAN-Ion measurements only would then appear to
show large spikes in the alpha abundance inside SBs compared to outside (not plotted here),
which as we have shown is not the case. As we will explain in the next section, the alpha
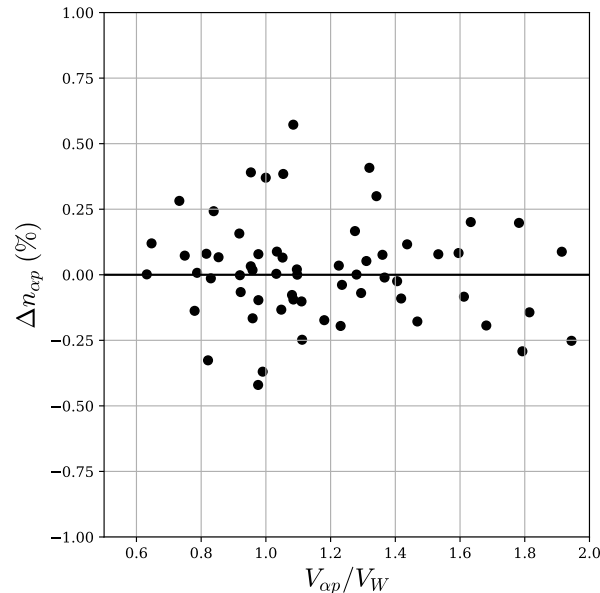
Figure 4.3: Scatter plot of change in alpha abundance in switchbacks vs alpha proton drift as a fraction of the local Alfvén wave phase speed. The distribution is symmetric showing no strong dependence.

particle VDFs tend to move much less in velocity space during SBs, and so the problem is much less significant and any motion that does occur can be properly captured by the fitting routines. Again, while the spread in the right histogram of figure 2 is relatively large, the distribution is clearly peaked about $\Delta n_{\alpha p} \approx 0$. We interpret these two figures then as showing there is no statistically significant change in either the alpha density or the alpha abundance inside SBs vs outside.

Lack of a compositional signature difference between the SB and LQ regions strongly suggests we are measuring the same plasma inside vs outside, in agreement with previous interpretations of SBs [188, 122, 112, 186]. We would certainly expect SBs generated in situ to not display any compositional differences in the plasma inside the SB compared to outside. However, these observations do not rule out coronal origins of SBs. SBs generated by interchange reconnection events further down in the corona may very well be expected to display compositional differences at the time they are generated. This is because the properties of plasma confined in closed magnetic loops is known to change (relative to open field lines) over the confinement time, due to processes like gravitational settling and the first ionization potential (FIP) effect [94, 143]. However the only way this would be measurable at PSP is if the alpha particles and the SB travel outwards together at exactly the same speed from their point of origin, preserving the compositional signature difference. While it has long been generally understood that alpha particles *do* travel faster than the protons at

approximately the local wave speed [161, 156, 115], giving rise to the phenomenon of alpha
particle "surfing" whereby alpha particles are less affected by the Alfvénic fluctuations, we
now show that this isn't always the case, and that expecting a compositional signature to
persist to PSP distances would require rather unphysical fine-tuning.

In fig. 4.3 we plot the change in alpha abundance $\Delta n_{\alpha p}$ vs the ratio of alpha-proton
drift speed to wave speed, $V_{\alpha p}/V_W$. $V_{\alpha p}$ is calculated as $|V_\alpha - V_{pc}|$ where V_α and V_{pc} are
the alpha and proton core velocities respectively, and V_W is computed by taking the normal
N-component of the equation

$$\delta \mathbf{V} = \pm V_W \frac{\delta \mathbf{B}}{|\mathbf{B}|}, \tag{4.1}$$

which serves to define the wave speed [62]. Plotting V_N vs $B_N/|\mathbf{B}|$ over the LQ region
associated with each SB and taking the gradient of a line of best fit then yields an estimate
of the local wave phase speed. (Note that equation 4.1 is effectively an empirical measurement
of the speed of Alfvénic fluctuations - it is not yet fully understood why V_W is usually less
than V_A in the solar wind [62, 127].)

From figure 4.3 we clearly see that alpha particles do not always travel at the local wave
speed; when considering short intervals such as these, there is a very wide range of $V_{\alpha p}/V_W$
values. There also does not appear to be any trend in $\Delta n_{\alpha p}$ with $V_{\alpha p}/V_W$. In particular,
there is no signature around $V_{\alpha p}/V_W \approx 1$, where one might expect such a compositional
signature to be were it present when the SB was generated; the spread in points around
$V_{\alpha p}/V_W \approx 1$ appears no different than the spread at other values. In retrospect however this
is not too surprising, for two reasons. First, even in the model of [189] where the interchange
reconnection is occurring relatively high up (compared to the photospheric reconnection
models of [52] and [42]), in coronal loops with scale height $\sim 6R_\odot$, the local Alfvén speed
is very high ($V_A \gtrsim 1000$ km/s), and the alpha particles are not expected to ever drift at
such high speeds ahead of the protons. Rather, the phenomenon of alpha particles surfing
at the Alfvén speed is only expected to kick in at greater radial distances, once the Alfvén
speed has decayed enough to be comparable to $V_{\alpha p}$ (and after which it may act as an
instability threshold preventing $V_{\alpha p} \gg V_A$ [170]). Thus, we wouldn't expect $V_{\alpha p}/V_W \approx 1$
to be possible at the site of interchange reconnection, and the alphas would not be able
to carry a compositional signature with the SB to be observed at PSP. Secondly, even if
the alpha particles could leave the interchange reconnection event at the same speed as the
SB, a PSP encounter with perihelion distance $\sim 30R_\odot$ still represents a travel distance of
several hundred Alfvén crossing times (using a typical SB length scale $l \sim 5 \times 10^4$ km [93]).
Therefore, barring some rather unphysical fine-tuning, any compositional signature would
have long since decayed away by the time the alpha particles reached PSP, and we would
expect to observe something like figure 4.3. In conclusion then, our results are all consistent
with in situ generation mechanisms of SBs, but cannot be used to rule out origin mechanisms
occurring further down in the corona or at the surface of the Sun.
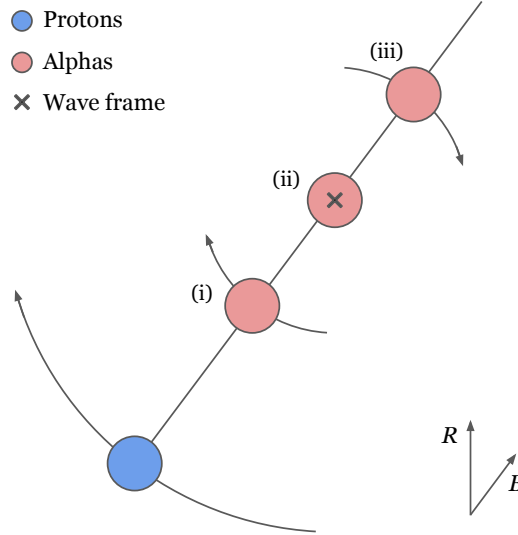
Figure 4.4: Cartoon showing the idealised expected alpha particle motion in velocity space during a SB in the three scenarios (i) $V_{\alpha p} < V_w$, (ii) $V_{\alpha p} \sim V_w$, (iii) $V_{\alpha p} > V_w$, corresponding to the rows of figure 4.5. R and B denote the radial and magnetic field directions respectively.

4.5.2 Alfvénic Motion of the Alphas

SBs are known to be highly Alfvénic and spherically polarised ($|\mathbf{B}| = $ constant), and we therefore expect the particle motion to be spherically polarised too. To see why, consider a particle at rest in the frame co-moving with the Alfvén wave. The magnetic field, being Galilean invariant, is still spherically polarised, and the wave being stationary means that energy is conserved in this frame (and that the electric field should almost vanish). A particle with perturbed velocity $\delta\mathbf{v}$ relative to this frame must therefore trace out a sphere in velocity space in order to conserve energy. Boosting back into the spacecraft frame we infer that the observed motion should be spherically polarised, centred at the wave frame velocity, with radius equal to the wave speed relative to whichever particle population we are considering. (For a more in-depth discussion of this see [115].) With this picture in mind, one can potentially expect three different types of alpha particle motion, depending on the relative magnitudes of $V_{\alpha p}$ and V_{pw}; these are sketched out in the cartoon in figure 4.4. In scenario (i) we have $V_{\alpha p} < V_{pw}$, and would expect to observe spherical polarisation of both the protons and alpha particles, with the alpha particles tracing out a sphere of smaller radius than the protons, approximately given by $V_{\alpha w} \approx V_{pw} - V_{\alpha p}$. In case (ii), the position of the alphas in velocity space roughly coincides with the wave frame, $V_{pw} \approx V_{\alpha p}$, and one would expect the protons to be spherically polarised but the alphas to be roughly stationary. In case (iii) we have $V_{\alpha p} > V_{pw}$, and so would again expect the protons and alphas to be spherically polarised, but importantly the alphas should move in anti-phase with the protons. This potential for
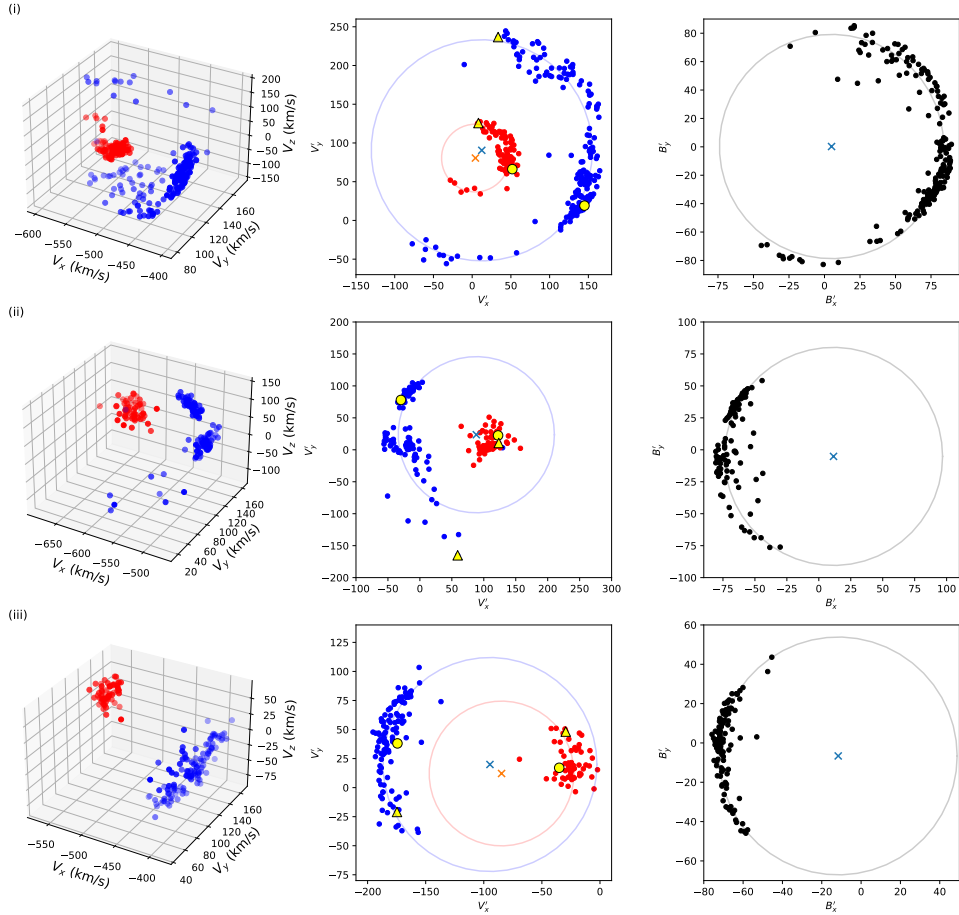
Figure 4.5: Three example SBs showing the different types of alpha-particle Alfvénic motion. First column is the 3D proton and alpha velocity measurements in instrument coordinates, in blue and red respectively, through the switchback. Middle column are these particle velocities projected onto the minimum variance magnetic field plane. Yellow circles indicate the start of the SB interval, yellow triangles the point of maximum deflection during the SB. Third column is the magnetic field measurements projected onto the same plane, with circles of best fit in grey (blue crosses mark the circles' centres).

alphas to move either in-phase or in anti-phase with protons during Alfvénic fluctuations depending on the relative values of $V_{\alpha p}$ and V_{pw} was first pointed out by [62] using Ulysses data. Understanding this in terms of spherical motion of each species in velocity space is exactly the model laid out in [115], the only difference here is that the cadence and quality of the SPAN-Ion measurements allow us to distinguish between the three cases over short timescales, and directly observe and measure the spherical polarisation of the alphas. In each row of figure 4.5 we show an example SB, illustrating the three main types of alpha

particle motion just described. The left column shows the 3D proton and alpha velocity
measurements (in blue and red respectively), in instrument coordinates. In all three cases
the proton motion (in blue) is spherically polarised as expected. Regarded as single large-
amplitude, low-frequency Alfvén waves, these switchbacks are not just spherically polarised
but to a good approximation arc-polarised as well [52], as first theoretically predicted by
[18] and observed many times in the solar wind since [99, 163, 144]. Their maximum and
intermediate principal component axes define a plane that is almost constant through the SB
interval, and the tip of the $\mathbf{B}$ field roughly traces out an arc on the sphere of $|\mathbf{B}| = $ constant.
If $\mathbf{e}_1, \mathbf{e}_2, \mathbf{e}_3$ are the orthonormal principal components of the magnetic field measurements
$\mathbf{B}_i$ for a single SB interval with eigenvalues $\lambda_1 \lesssim \lambda_2 \ll \lambda_3$, we can project the measurements
onto the plane defined by e_2 and e_3, which should be the plane in which they appear most
circular; this is shown in the third column of fig. 4.5. The fluctuations being Alfvénic means
we can project the velocity measurements onto the same plane; this is plotted in the second
column of fig. 4.5.

From the middle plot of the first SB example (taken from 2019-08-30/22:50:25 to 2019-
08-30/23:12:47), we can see that the alpha particle velocities in red are spherically polarised
as well, albeit with a smaller amplitude - they move on the surface of a smaller sphere.
To a good approximation, the alpha and proton velocities both subtend the same angle θ
that the magnetic field does, and appear to be rotating about a similar point in velocity
space. The yellow circle represents the start of the entire SB interval, and the yellow triangle
the point of maximum $\mathbf{B}$ field deflection during the SB. From these we can see that the
protons and alphas are moving in phase with each other. This corresponds to scenario (i),
$V_{\alpha p} < V_{pw}$, in figure 4.4. Circles of best fit to the proton and alpha motion are overlaid in
blue and red respectively, their centres marked with crosses. The proximity of the centres
of the alpha and proton circles shows good agreement between these two components of
the wave frame velocity. The third component can be estimated by calculating the (e_2, e_3)
plane that minimises the least square distance to the measured velocities for each species
separately (this is then the plane of arc-polarisation). For protons the sphere centre is $\mathbf{v}_{pw} = $
$(-543, 147, 16)$ km/s and for the alphas it is $\mathbf{v}_{\alpha w} = (-547, 152, 28)$ km/s (in instrument
coordinates), showing very good agreement in all three components. Because the alpha
fits are independent of the proton fits (they are not constrained to lie along the magnetic
field relative to the proton VDFs), fitting spheres in this way represents two independent
estimates of the wave frame velocity. Using equation 4.1 during the LQ region of this SB,
we estimate the local alpha and proton wave phase speeds as $V_{pw} \approx 148$ km/s and $V_{\alpha w} \approx 41$
km/s. This is in excellent agreement with the radii of the spheres of best fit in column 2,
which have radii of 143 and 44 km/s respectively. With $V_{\alpha p} \approx 114$ km/s in the LQ region we
also have $V_{\alpha p} < V_{pw}$ and $V_{\alpha p} + V_{\alpha w} \approx V_{pw}$ as expected. Comparing to the measured Alfvén
speed $V_A \approx 147$ km/s, for this SB we have that the proton phase speed and Alfvén speed are
almost equal, $V_{pw} \approx 0.99 V_A$. In time series of the particle velocities for SBs like this, the large
spikes in the proton velocity would also be seen in the alphas, albeit smaller in magnitude.
This is clearly seen in the summary plot in figure 4.6. The top two panels are scatter plots
of V_N vs B_N/B for protons (left) and alphas (right), illustrating how the wave velocity is
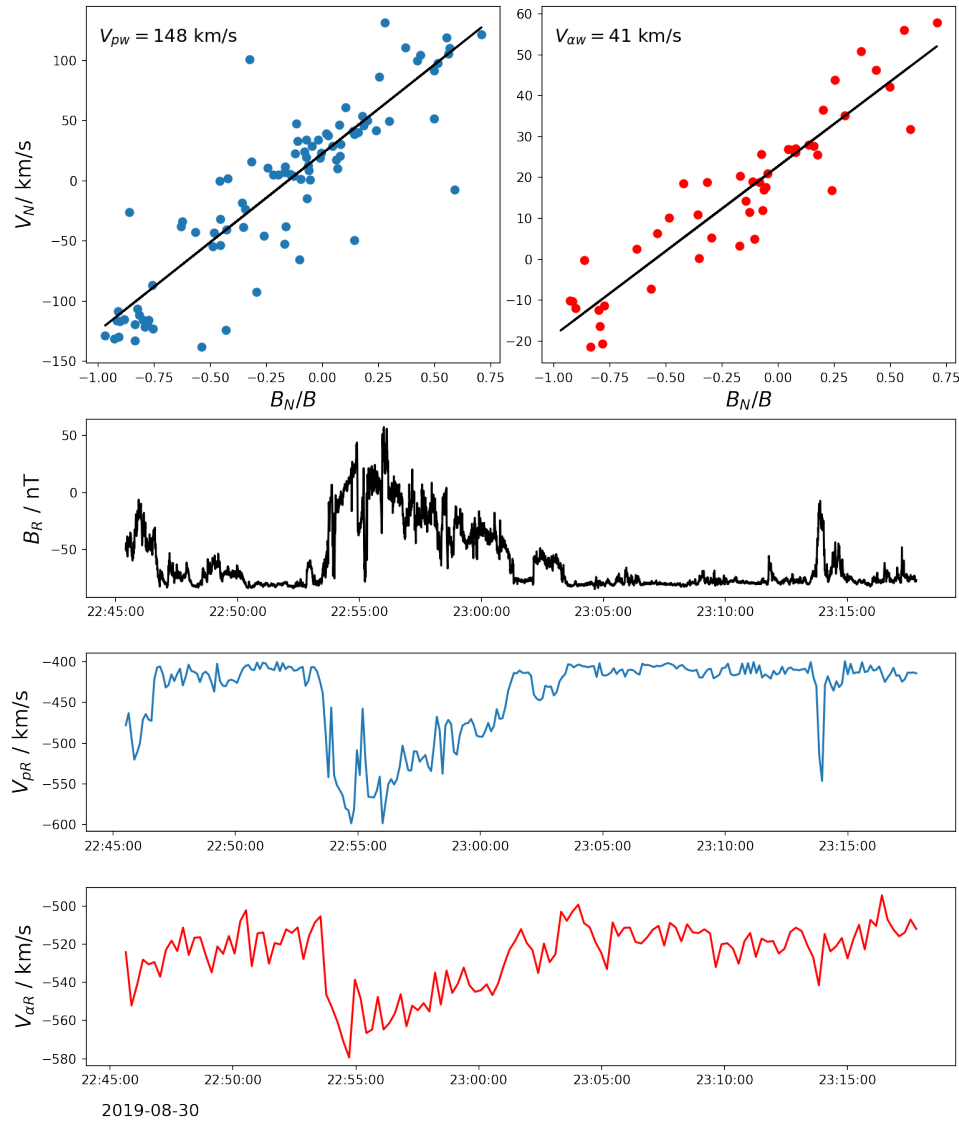
Figure 4.6: Summary plot of the first example switchback in figure 4.5 (top row) and discussed in the text. Top two panels are scatter plots of proton (left) and alpha (right) normal velocity V_N vs magnetic field normal component B_N/B, from which the wave speed can be calculated using equation 4.1. Three panels below are radial components of the magnetic field, proton velocity, and alpha velocity, showing highly Alfvénic correlations with the same sign between all three.
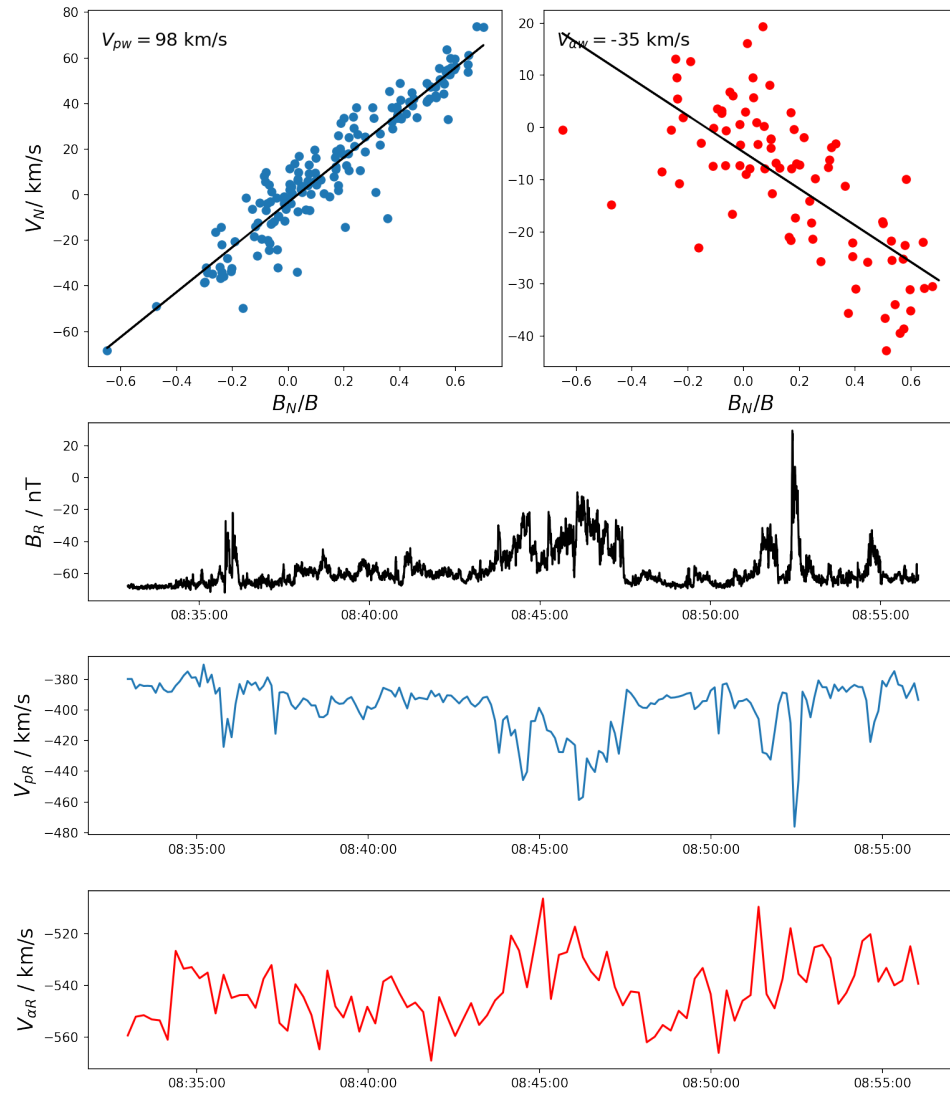
Figure 4.7: Summary plot of the third example switchback in figure 4.5 (bottom row) and discussed in the text. Panels as in figure 4.6. The antiphase motion of the alphas relative to the protons is clearly observed, with a decrease (in magnitude) of $V_{\alpha R}$ observed during the increase in V_{pR}.

computed using equation 4.1. The three panels below are radial components of the magnetic field, proton velocity, and alpha velocity respectively. The highly correlated Alfvénic motion between both species and the magnetic field is clearly visible, and the magnitude of the increase in alpha velocity is smaller than that in the proton velocity, as expected (~ 70 km/s compared to ~ 180 km/s).

In the second example SB (middle row), (taken from 2019-08-29/21:08:04 to 2019-08-29/21:20:46), the proton velocities are still spherically polarised, but the alpha's are not - they appear relatively stationary in velocity space through the SB and do not trace out an arc (the yellow markers for initial and maximum **B** deflection lie almost on top of each other). This corresponds to scenario (ii) in figure 4.4, where $V_{\alpha w} \approx 0$, and for the LQ interval preceding this SB, we have $V_{\alpha p} \approx 158$ km/s, $V_{pw} \approx 162$ km/s, and $V_{\alpha w} \approx 6$ km/s, with $V_A \approx 161$ km/s so that $V_{pw} \approx 1.01 V_A$. The alphas are therefore roughly comoving with the wave, and their location in velocity space serves as an estimate of the wave frame. The centre of the proton circle of best fit in blue lies reasonably close to the alpha velocities, but we note there is a fair amount of scatter in the proton measurements for this SB.

Finally, in the third example SB in the bottom row (from 2019-08-29/08:37:52 to 2019-08-29/08:51:09), the alphas are again spherically polarised, but moving in anti-phase with the protons, as can be seen by the relative locations of the points of maximum SB deflection (yellow triangles). This corresponds to scenario (iii) in figure 4.4. For this LQ region we have $V_{\alpha p} \approx 167$ km/s, $V_{pw} \approx 98$ km/s, and $V_{\alpha w} \approx -35$ km/s, with $V_A \approx 105$ km/s so that $V_{pw} \approx 0.93 V_A$. The quantitative agreement is not quite as good as previous, qualitatively however $V_{\alpha p} > V_{pw}$, and $V_{\alpha w}$ and V_{pw} have opposite signs, as expected. For SBs such as these, a time series of particle velocities would see spikes in proton velocity coinciding with dips in alpha velocity. This is indeed seen in the summary plot for this switchback in figure 4.7. We see the negative gradient in the scatter plot of $V_{\alpha N}$ vs B_N/B, and the antiphase (but still Alfvénic) motion reflected in the profiles of the alpha radial velocity $V_{\alpha R}$, relative to the proton radial velocity V_{pR}. We note that this anti-phase motion would also be expected to be observed in proton beams, since they typically travel at or slightly above the Alfvén speed relative to the core [3].

4.5.3 Relation to the de Hoffman-Teller Frame

Finally, for completeness we compare the wave frames determined using the methods described above with the direct computation of the de Hoffman-Teller (DHT) frame. First introduced by [41] in the context of MHD shocks, it is defined to be the frame in which the plasma's electric field vanishes, and is usually computed by finding the velocity **V** that minimizes the quantity [87]

$$D(\mathbf{V}) = \frac{1}{M} \sum_{m=1}^{M} \left| (\mathbf{v}^{(m)} - \mathbf{V}) \times \mathbf{B}^{(m)} \right|^2, \tag{4.2}$$

SB	$\mathbf{v}_{pw}$ (km/s)	$\mathbf{V}_{DHT}$ (km/s)
(i)	(-543, 147, 16)	(-548, 116, 9)
(ii)	(-598, 155, 33)	(-614, 152, 12)
(iii)	(-483, 128, 1)	(-473, 123, 9)

Table 4.1: Values of the wave frame velocity as computed via sphere fitting ($\mathbf{v}_{pw}$) and direct computation of the de Hoffman-Teller frame $\mathbf{V}_{DHT}$, for each of the three example SBs.

where $\mathbf{v}^{(m)}, \mathbf{B}^{(m)}$ denote velocity and magnetic field values over a series of measurements indexed by $m = 1, \ldots, M$. By definition we expect the DHT frame and the wave frames computed above to be one and the same. To see geometrically why this is so for the SBs being considered here, consider the ideal case of a perfectly spherically polarised Alfvén wave. The minimum value of $D(\mathbf{V}) = 0$ will be achieved only if each term in eq. 4.2 vanishes, which requires $\mathbf{V}_{\mathrm{DHT}}$ to lie on the line through $\mathbf{v}^{(m)}$ parallel to $\mathbf{B}^{(m)}$, for each measurement m. The point that uniquely satisfies this is the centre of the sphere in velocity space (as it is the point of intersection of each of these lines through $\mathbf{v}^{(m)}$). Thus, regarding SBs as essentially single, large-amplitude spherically polarised Alfvén waves, we expect $\mathbf{V}_{\mathrm{DHT}}$ and $\mathbf{v}_{pw}$ to agree to good approximation, and this is indeed the case for our three example SBs, as summarised in Table 4.1.

4.6 Conclusions

In this work the density and abundance variations of alpha particles were examined in a database of 92 switchbacks from PSP's encounter 3 and 4. No consistent compositional signature difference was observed in the alpha abundance $n_{\alpha p}$ inside SBs vs outside, suggesting that PSP is measuring the same plasma in both cases, in agreement with previous interpretations of SBs [188, 112, 186]. We argued that even if SBs are the results of interchange reconnection events lower down in the corona, compositional signatures are not likely to exist and be measurable at PSP for two reasons: 1) the local Alfvén speed at the postulated interchange reconnection sites is very high and most likely precludes alphas being able to travel with the SBs that are launched upwards along the field lines (thus preventing compositional information being carried with the SB), and 2) even if the alphas are able to travel with the SB, a small difference between $V_{\alpha p}$ and V_{pw} would cause a compositional signature to have long decayed away due to the distance (in Alfvén crossing times) to PSP's perihelia. Thus, our observation of there being no dependence of $\Delta n_{\alpha p}$ on $V_{\alpha p}/V_{pw}$ is to be expected and does not help distinguish between in situ generation and interchange reconnection as potential SB formation mechanisms.

In addition, we examined the three-dimensional nature of the velocity fluctuations of both protons and alphas within individual SBs. We observed spherical polarisation of both the

proton and alpha velocities, which can be understood as a consequence of energy conservation in the wave frame. Three example SBs showed the alphas moving in-phase, stationary relative to, and in anti-phase with, the protons. This corresponds to the three cases $V_{\alpha p} < V_{pw}$, $V_{\alpha p} \approx V_{pw}$, and $V_{\alpha p} > V_{pw}$. Thus while SBs are always associated with spikes in the proton velocity, alpha velocities may be enhanced, unchanged, or decrease, depending on the relative values of $V_{\alpha p}$ and V_{pw}. For the case $V_{\alpha p} < V_{pw}$, where the alphas move in phase on a sphere of smaller radius than the protons, the centres of the proton and alpha velocity spheres were in excellent agreement, illustrating how one can make two independent particle measurements to uniquely identify the wave frame. One can in principle use these methods to estimate the wave frame over short time scales using purely particle measurements, and we showed that this agreed well with the the usual method of computing the de Hoffman-Teller frame via minimisation of the motional electric field, $\mathbf{E} = -\mathbf{v} \times \mathbf{B}$. Intuitively then the Alfvenic motion of both the alphas and the protons through SBs can be understood as approximately rigid arm rotation about the location of the wave frame in velocity space, as illustrated in 4.4 and discussed in [116, 115], and the length of the lever arms are to a good approximation given by V_{pw} and $V_{\alpha w}$ for protons and alphas respectively.

Chapter 5

Observation and Statistics of Secondary Alpha Particle Populations in the Inner Heliosphere

5.1 Abstract

Proton velocity distribution functions (VDFs) in the solar wind have long been known to be well described by a core population and a less dense, faster moving beam population. Alpha particle VDFs are also known to sometimes exhibit a core-beam structure, but direct measurements are scarce, and alphas are most often treated as a single population in the literature. We present observations from Parker Solar Probe's 3rd encounter, showing clearly resolved core-beam structure in the alpha VDFs, and fit double bi-Maxwellians to both the proton and alpha VDFs. Normalised parallel heat flux, computed in the centre of mass frame of each species, is used as a quantitative measure of the VDF asymmetry along **B** and the prominence of the beam population. We find that during E3 proton beams are essentially ubiquitous and always measurable, with the proton beam drifting at an average speed of $1.1v_A$ relative to the proton core, and carrying a density fraction $n_{pb}/n_{p\mathrm{tot}}$ of 0.2 on average. Alpha beams on the other hand occurred much less frequently (as measured by $q_{\parallel}$), and we find that when alpha beams do occur they tend to drift more slowly relative to the alpha core population ($v_d \sim 0.7v_A$) and carry larger fractional density ($n_{\alpha b}/n_{\alpha\mathrm{tot}} \sim 0.35$) on average compared to the proton VDFs. We also show that there are localised time periods when the proton-frame and alpha-frame heat fluxes are strongly correlated, suggesting a common mechanism acting on both species' VDFs to produce the beam population. Using a source surface model we map our measurements back to the solar surface, but no firm conclusions can be drawn in distinguishing between beam generation mechanisms occurring at or near the source surface versus those happening in interplanetary space.

5.2 Preface

In this Chapter we change tack slightly from switchbacks and present a paper I have written (to be submitted to ApJ) that studies the alpha particle VDFs in more detail. Refining the fitting routines that we used to study the bulk Alfvénic motion of the alpha particles in the previous chapter, we focus now on measuring and characterising secondary alpha particle populations - or alpha beams. These are a rarely measured feature of the alpha VDFs and there have been no previous statistical studies of their properties. Because of this, not very much is known about them, and so we focus on very simple questions: 1) How often do they occur? 2) How dense are they typically? 3) How fast do they drift, relative to the core? 4) Do they occur at the same time as proton beams? 5) Is it possible to determine whether either the proton or alpha beams originate from processes occurring deep in the corona/on the solar surface, or are they generated in situ?

5.3 Introduction

Proton velocity distribution functions (VDFs) in the solar wind are well described by a dense, bi-Maxwellian, anisotropic "core", and a drifting, field aligned, lower density, bi-Maxwellian "beam". The beam being a commonly observed feature of proton VDFs has been known since the earliest days of in situ solar wind measurements [48, 109, 65], and it is particularly easy to observe in high speed wind. Despite a long history of observations, the precise mechanisms responsible for beam formation and evolution are still not fully understood, and many different theories have been proposed. In particular, the question of whether they originate at the base of the corona or develop in situ as the solar wind expands and travels outwards is still open.

An early idea for in situ beam generation by [102] postulated that beams arise due to the interplay between the low collisionality of the solar wind and the temperature anisotropisation $T_\parallel > T_\perp$ that naturally occurs as the plasma expands in the diverging interplanetary magnetic field. The fastest moving particles have the lowest collisional cross-sections and so runaway can't be prevented, and they showed via simulations that this leads to a field aligned secondary particle population. Most recent work on in situ beam generation however has tended to focus on various wave-particle interaction mechanisms. [140] describe a model where the field aligned electric potential generated by kinetic Alfvén waves (KAWs) with large $k_\perp$ traps and accelerates particles to produce a super-Alfvénic beam. The authors point out that this mechanism should also be able to produce heavier ion beams. [98] carry out 1D simulations successfully showing the formation of core and beam populations from an initially Maxwellian distribution under the action of just such a KAW. In [174] this is discussed further and the authors show that the conditions necessary for this process to occur naturally arise in solar wind turbulence at ion gyroradius scales. [119] and [106] describe a scenario where the parallel electric field required to accelerate the proton beam is instead generated by the ion-acoustic mode created in a parametric decay instability.

Magnetic reconnection, because it both energises particles and produces interpenetrating ion populations from different field lines, is a natural candidate to explain the presence of ion beams. [49] and [47] put forward the idea that higher speed injections of proton jets driven by magnetic reconnection in the chromosphere-corona transition region are responsible for the secondary proton populations. This model incidentally predicted a single component alpha particle distribution as Helium is "dragged" up by these jets via collisional friction. In [67] interchange reconnection between open coronal hole field lines and the closed field lines of the heliospheric current sheet (HCS) is used to explain Ulysses observations of ion beams either side of HCS crossings, but a lack of beams inside the HCS itself. This should however be contrasted with recent direct observations [137] of the formation of field aligned, energetic proton beams near the HCS due to high energy protons leaking out of *local* reconnection exhausts. [97] discuss a similar local reconnection mechanism, using detailed measurements of a reconnection event at the boundary of a magnetic switchback.

In contrast to the historically well established proton core and beam measurements, references to alpha beams are much more scarce. For clarity, in this work we refer to alpha particle VDFs in terms of a "core" and "beam" population exactly analogously to the protons. While the alphas are themselves a beam relative to the protons (and often referred to as such in the literature), we do not use the word in this sense to avoid confusion. In a comprehensive overview of the Helios observations of Helium ions from 0.3-1AU, [108] mention frequently seeing "magnetic-field-aligned bulges" in the alpha particle VDFs, constituting a non-zero heat flux, as well as give several example distributions where the secondary population forms a distinct second peak. [4] analyse 8 examples of distinct double peaked distributions in both the proton and alpha VDFs at 1AU. With such distinct and well resolved double peaks measured simultaneously in the protons and alphas, the majority of the discussion and interpretation was in the context of interpenetrating solar wind streams, as opposed to wave-particle processes or the second peak being an intrinsic feature of ion VDFs. In a large-scale survey of IMP 7 and 8 observations at 1AU, [49] conclude that the fast solar wind is characterised by two proton populations, and, in the vast majority of cases, one single alpha population. However, the authors give several isolated examples of distinctly non-Maxwellian alpha counts spectra, showing shoulder like beams and relatively flat-topped distributions. It is unclear whether the dearth of recorded observations of alpha beams in the literature is due to difficulty of measurement, rarity of occurrence, beams becoming less prevalent as the solar wind expands outwards (due to thermalization via Coulomb collisions, [3, 43]), or something else. In this work, we present measurements of both proton and alpha particle VDFs using the SPAN-Ion instrument [101] on board PSP, fitting core and beam bi-Maxwellians to both species and comparing the results.

5.4 Data

For this work we focus on the entirety of PSP's 3rd encounter (E3) from August 27th to September 7th 2019, with perihelion on September 1st at 17:50 UTC. PSP's distance from

the Sun during the encounter ranged from $57R_S$ to $35.7R_S$ or 0.17 AU at perihelion. For
the majority of the encounter PSP was situated in slow Alvénic wind, with relatively low
proton densities ranging from roughly 80 to 350 cm^{-3}, and bulk proton speeds ranging from
~ 250 to 550 km/s. The alpha particle density ranged from 2 to 6 cm^{-3} with speeds from
~ 250 to 700 km/s. This encounter contained no current sheet crossings, and PSP was not
particularly close to the HCS (a point we return to in section 5.5.5), making this encounter
somewhat more straightforward to analyse and fit to.

5.4.1   Fitting

The SPAN-Ion instrument is an electrostatic analyser (ESA) that measures three-dimensional
velocity distribution functions (VDFs) and is capable of distinguishing particle masses via
time-of-flight measurements. Three-dimensional counts spectra are organised into 32 energy-
per-charge by 8 azimuthal angle by 8 polar angle bins. The 32 energy bins are logarithmically
spaced from 125 eV to 20 keV, the 8 azimuthal angle bins each have a width of 11.25°, and
the 8 polar angle bins each have an average width of 14.5°. The proton (SF00) and alpha
(SF01) VDFs are produced at cadences of 6.99s and 13.98s respectively. In this work, in
order to obtain better statistics and more easily resolve the ion beams, we sum together 8
alpha SF01 spectra and 16 proton SF00 spectra, resulting in an effective cadence of 112s for
the fits to each species.

For the proton SF00 channel, we perform 3D bi-Maxwellian fits to both the proton core
and the proton beam, where we parameterise a bi-Maxwellian $f^M(\mathbf{v})$ as

$$f^M(\mathbf{v}) = n \left(\frac{m}{2\pi}\right)^{\frac{3}{2}} \sqrt{\frac{R}{T_\perp^3}} \exp\left(-\frac{\frac{1}{2}m\mathbf{v}^2}{T_\perp} \times \left\{\cos^2\Theta(R-1)+1\right\}\right), \qquad (5.1)$$

where n is the particle number density, m the mass, $T_\perp, T_\parallel$ the perpendicular and parallel
temperatures, $R = T_\perp/T_\parallel$ the temperature anisotropy, and Θ the angle between the vector
$\mathbf{v}$ and the magnetic field $\mathbf{B}$. We constrain the proton beam to lie along the magnetic field
direction relative to the proton core, so that the function $f_p(\mathbf{v})$ being fit to the proton counts
spectra is

$$f_p(\mathbf{v}) = f_{pc}^M(\mathbf{v} - \mathbf{v}_{pc}) + f_{pb}^M(\mathbf{v} - \mathbf{v}_{pb}), \qquad (5.2)$$

where $\mathbf{v}_{pb} \equiv \mathbf{v}_{pc} + v_{pd}\hat{\mathbf{B}}$ defines the scalar beam-core drift velocity v_{pd} relating the proton
core velocity $\mathbf{v}_{pc}$ to the proton beam velocity $\mathbf{v}_{pb}$ and the magnetic field direction $\hat{\mathbf{B}}$. We
therefore fit 10 free parameters (6 for the core, 4 for the beam) to the SF00 counts spectra.

5.4.2   Alpha Channel

SPAN-Ion's SF01 channel contains a small ($\sim 2\%$) contamination from the proton channel,
which, given the relative alpha particle abundance represents a very significant source of
noise that needs to be accounted for when fitting. It was checked that there is no energy
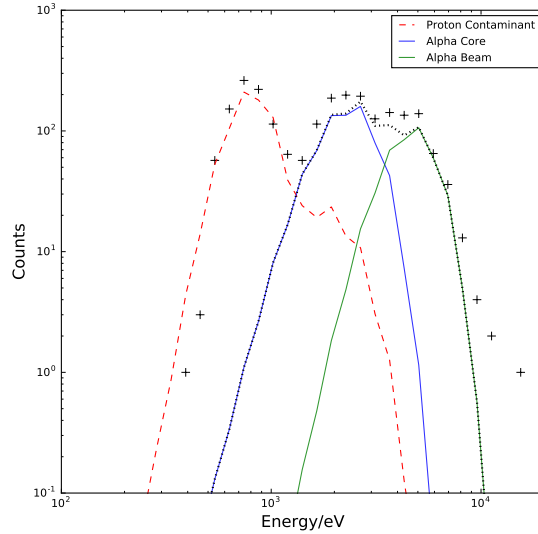
Figure 5.1: Example fit of equation 5.2 to a counts spectra in a single look direction of the SF01 alpha channel. Crosses are the raw counts; the red dashed, blue, and green lines represent fits to the proton contamination, alpha core, and alpha beam respectively. The black dotted is the sum of the alpha core and alpha beam components.

or angle dependence to the contaminant protons in the alpha channel, which allows us to simply take the fitted proton parameters and scale down the density to the $\sim 2\%$ level to take into account the contamination. Thus the function fit to the SF01 channel is

$$f_\alpha(\mathbf{v}) = \epsilon f_p(\mathbf{v}) + f_{\alpha c}^M(\mathbf{v} - \mathbf{v}_{\alpha c}) + f_{\alpha b}^M(\mathbf{v} - \mathbf{v}_{\alpha b}) \tag{5.3}$$

where the fitted parameter ϵ represents the instantaneous proportion of protons leaking into the alpha channel, and $f_{\alpha c}^M$, $f_{\alpha b}^M$ are defined analogously to eq. 5.2. The alpha channel fits thus have 11 free parameters (6 for the alpha core, 4 for the alpha beam, and ϵ). Figure 5.1 shows an example of fitting eq. 5.3 to an SF01 counts spectra (only one look direction out of 64 is shown).

5.4.3 Core vs Beam Labelling

When fitting eq. 5.2 to a counts spectra, there arises the question of which population to label as the core and which to label as the beam. In this work we adopt the convention that whichever fitted population has the higher phase space density at its bulk velocity, $f^M(\mathbf{0}) = n \left(\frac{m}{2\pi}\right)^{3/2} \frac{1}{T_\perp T_\parallel^{1/2}}$, will be labelled as the core. Classification schemes based on the speed of each population are undesirable because of the ubiquitous presence of magnetic

switchbacks [83, 182]. These magnetic field reversals have been shown [122] to be localised s-shaped kinks in the magnetic field and can therefore lead to an effective swapping of core and beam in velocity space. This has been observed in Ulysses data [129] and in recent PSP observations [123]. Denoting the beam to always be the lower density population was also deemed unsatisfactory because, as will be discussed in the next section, the density of the shoulder-like secondary population in alpha particle VDFs often exceeds that of the core, despite having a lower phase space height. PSP measurements have shown that this can happen in proton VDFs as well - [168] detail two spectacular ion-scale wave events where the proton beam is several times more dense than the core.

5.5 Results and Discussion

5.5.1 Qualitative Features

In figure 5.2 we illustrate some cuts through a variety of proton (left column) and alpha (right column) distribution functions during E3, displayed in the zx-plane of SPAN-Ion's instrument coordinates. The x axis corresponds roughly to the R direction and the z axis roughly to N. The black arrow overlaid is the magnetic field $\mathbf{B}$, its length is the local Alfvén speed computed using SPAN-Ion's measurement of the proton density. All four of the proton VDFs display prominent, field aligned beams; isotropic or beamless proton VDFs are rarely seen during this encounter. All except for (c) show a very anisotropic ($T_{c\perp}/T_{c\parallel} > 1$) core, and all have an overall anisotropy of $T_\perp/T_\parallel < 1$ when including the beam. Typically the proton beams show evidence of significant perpendicular heating, however distribution (c) shows a more isotropic core with a very narrow, elongated beam. Distribution (g) is measured towards the end of the encounter when PSP was in slower wind. The wind speed and temperatures are lower however the qualitative shape of the VDF is essentially the same as the earlier ones.

The alpha VDFs measured at the same time as the proton VDFs are shown in the right-hand column. For the purposes of these figures we have subtracted off and zeroed out the contribution from the contaminant protons described in section 5.4.2. The alpha-proton differential speed is such that the overlap in the two species' VDFs during E3 is small. In these few examples we already see a wide variety of non-thermal features. In VDFs (b), (d) and (h) a very clear core-beam structure is seen, analogous to the proton VDFs. The alpha core populations, as with the proton cores, also have $T_{c\perp}/T_{c\parallel} > 1$. The beam in (d) is prominent enough to actually be a secondary maximum in phase space. This is not commonly seen during E3 in either the proton or alpha VDFs, which usually display shoulder-like beams. In addition to a core-beam structure, VDFs (b) and (d) display very striking, arc-like features at large velocities, somewhat symmetric about the magnetic field direction, almost $2v_A$ away from the alpha core. These so-called "hammerhead" features are often seen in the proton VDFs as well, although particularly clear examples are not shown here. It is thought these are the result of resonant wave particle interactions with right
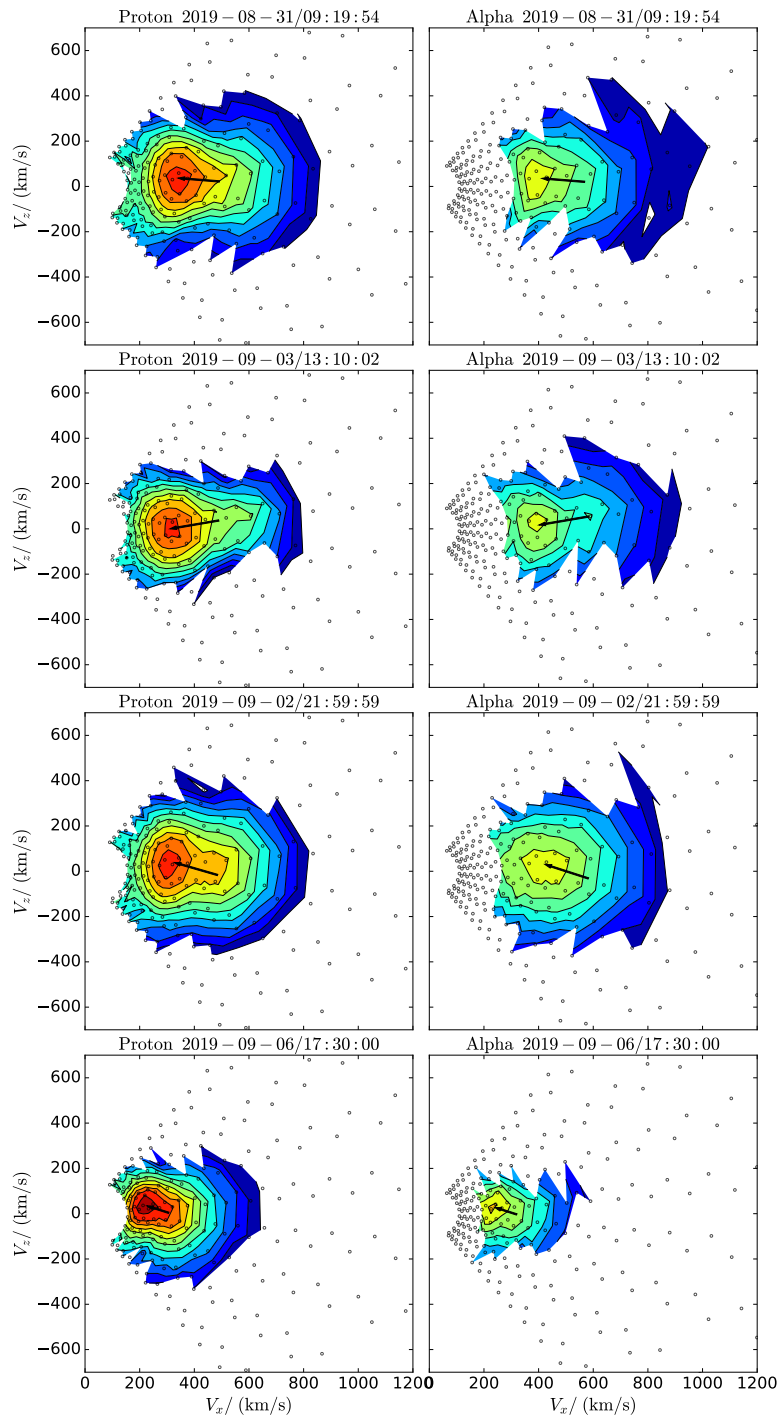
Figure 5.2: Example proton (left column) and alpha (right column) VDFs. Black arrows
represent the magnetic field direction, length of the arrow is the Alfvén speed.

handed fast magnetosonic/whistler waves (since the left handed resonance usually involves
the sunward part of the VDF), leading to pitch angle diffusion along "shells" of constant
energy in the reference frame of the wave [74, 75]. This interpretation was recently tested
using PSP measured proton VDFs [169], and the predictions of the linear theory were found
to agree well with the observations. In addition, figure 5.1 quite clearly shows a high energy
suprathermal tail above the alpha beam population. These also appear in the proton VDFs,
and are well known, ubiquitous features of the solar wind [37, 61], although what seeds these
populations in general is not known. We note then that a simple two bi-Maxwellian fit is
insufficient to capture the wide variety of kinetic features displayed by the proton and alpha
VDFs, and we leave the modelling of these features to future work.

Finally, distribution (f) shows a far more isotropic looking VDF with no distinct beam.
This type of beamless distribution is seen far more commonly in the alphas than the pro-
tons during E3. This instantly presents a problem when attempting to fit two drifting bi-
Maxwellians to the alpha VDFs - it will always be possible to fit two bi-Maxwellians under
one larger bi-Maxwellian, the result will simply be a small drift speed v_d and a large frac-
tional beam density n_b/n. These small drifts and large fractional densities will significantly
skew the statistics if such beamless distributions are common, as is the case here. One way
to distinguish the two cases would be to compute the normalised χ^2 per degree of freedom
ν for a single vs double bi-Maxwellian fit, and pick whichever is smaller. However, since the
number of degrees of freedom in the fits are very large (SPAN-Ion makes 2048 measurement
points in phase space), and a single vs double bi-Maxwellian fit only represents a change in
ν of 4, it was found that the normalised chi-squared was not a sensitive enough quantity
to distinguish the distributions in this way. To get around this problem we use normalised
parallel heat flux to quantify the asymmetry of the VDF along the magnetic field, and use
this to distinguish between beamless VDFs and those with beams, as described in the next
section.

5.5.2   Heat Flux

The parallel heat flux $q_\parallel$, computed in each particle species' centre of mass frame, quantifies
the asymmetry of a particle VDF along the magnetic field direction, and can therefore be
used as an indicator of both the presence of an ion beam, as well as how prominent it is.
A single bi-Maxwellian of course has $q_\parallel = 0$ in the centre of mass frame. Computing the
integral $q_{\parallel s} = \int \frac{1}{2} m_s v^2 v_\parallel f_s(\mathbf{v}) d^3\mathbf{v}$ for a distribution function of the form in eq. (5.2) we
obtain

$$q_\parallel = \frac{1}{2} m \frac{n_1 n_2}{n_1 + n_2} v_d \left(\frac{3}{2} \left(v_{t2\parallel}^2 - v_{t1\parallel}^2 \right) + v_d^2 \frac{n_1^2 - n_2^2}{(n_1 + n_2)^2} + v_{t2\perp}^2 - v_{t1\perp}^2 \right), \qquad (5.4)$$

where the $v_t^2 = 2T/m$ are thermal velocities. We define the normalised parallel dimensionless
heat flux $\tilde{q}_\parallel$ as

$$\tilde{q}_\parallel = \frac{q_\parallel}{m(n_1 + n_2) T_\parallel^{3/2}} \qquad (5.5)$$
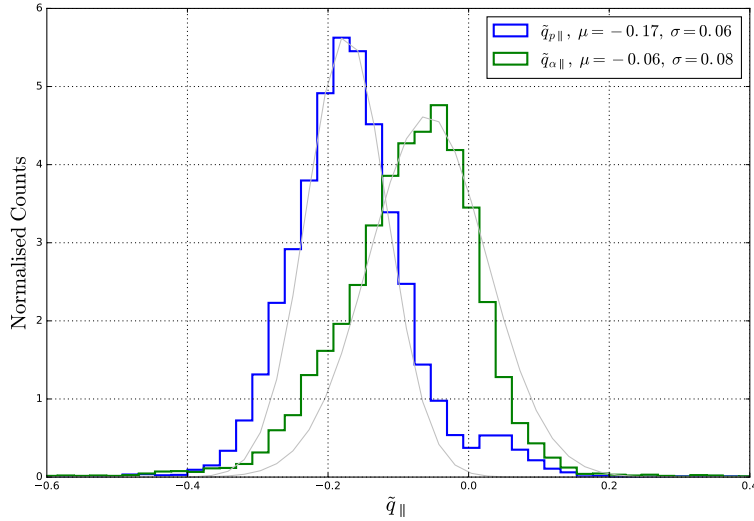
Figure 5.3: Histograms of normalised heat flux along the magnetic field direction in the proton (blue) and alpha (green) centre of mass frames.

where $T_\parallel$ is the total parallel temperature of the full VDF given by

$$T_\parallel = \frac{1}{n_1 + n_2} \left(n_1 T_{1\parallel} + n_2 T_{2\parallel} + m v_d^2 \frac{n_1 n_2}{n_1 + n_2} \right). \tag{5.6}$$

Figure 5.3 shows histograms of alpha and proton normalised heat fluxes for the full encounter. The light grey curves are Gaussian fits to those histogram bins with counts within 30% of the maximal counts bin. The parameters for each of these fits are $\mu_p \approx -0.17$, $\sigma_p \approx 0.06$ and $\mu_\alpha \approx -0.06$, $\sigma_\alpha \approx 0.08$. It's clearly seen that proton VDFs carry on average significantly more (almost three times as much) normalised heat flux in their own rest frame than alpha VDFs, meaning they are much more asymmetric along the magnetic field than alpha particle VDFs. The fact that the proton curve is centred almost $3\sigma_p$ away from the origin tells us that proton beams are essentially ubiquitous throughout this encounter and isotropic proton VDFs are rarely seen. In contrast, the alpha histogram being centred less than $1\sigma_\alpha$ from the origin means that a large proportion of the time the alpha VDFs are essentially beamless and well described by a single bi-Maxwellian, and occurrence of an alpha beam is much less common than for protons. The distribution does however have a large tail. We interpret these data points to be times when the distribution possesses a prominent beam, as in figure 5.2. In this work we are interested in observing and measuring the properties of *distinct* secondary alpha and proton populations. Ideally a fitting routine would produce $n_b \approx 0$ for a distribution best described by one bi-Maxwellian and no beam. While often true, this isn't always the case. Careful consideration of our fits showed that sometimes two Gaussians are
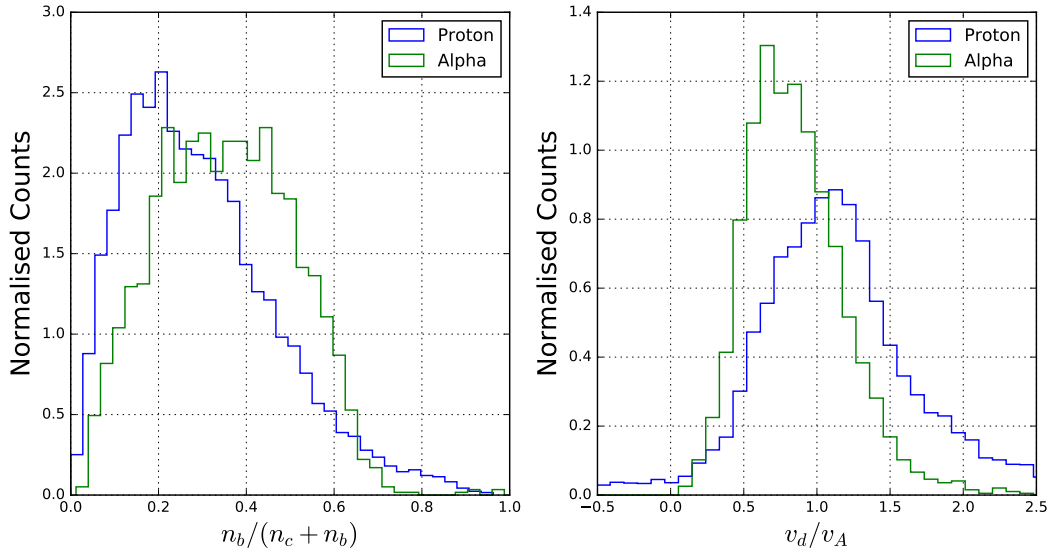
Figure 5.4: Left: Histograms of proton beam density fraction (blue) and alpha beam
density fraction (green). Right: Histograms of proton beam-core drift speeds (blue) and
alpha beam-core drift speeds (green), shown as a fraction of the Alfvén speed.

fit "under" what would best be described as one bi-Maxwellian, the result being a fit with
$n_b/n \sim 0.5$ and a very small drift speed ($v_d \lesssim 10$ km/s). The easiest way to remove these
fits from consideration is filtering by sufficiently large heat flux. For the analysis that follows
then we only include measurements with $q_{\alpha\parallel} \leq -0.14$ (one σ away from the mean), which
corresponds to $\sim 25\%$ of the data points. While this value of $q_{\alpha\parallel}$ is in some sense arbitrary
(in the same way that there is a continuum of skewness values between a pure bi-Maxwellian
distribution and one with a prominent beam), we note that our broad stroke conclusions are
not significantly affected by the choice of heat flux cutoff. For proton distributions no such
cutoff is required since as noted a proton beam is essentially always present and measurable
during E3, and we include all data points in our statistics.

5.5.3   Beam Densities and Beam-Core Drift Speeds

The left plot in figure 5.4 shows histograms of beam densities as a fraction of the total
density for protons (blue) and alphas (green). The proton histogram peaks at 0.2, in very
good agreement with the case study in [155] of an interval of slow Alfvénic wind at ~ 0.35
AU using Helios data. Their value of $n_{pb}/(n_{pc} + n_{pb}) \sim 0.18$ was significantly higher than
the fast Alfvénic ($n_{pb}/(n_{pc} + n_{pb}) \sim 0.07$) and the slow solar wind ($n_{pb}/(n_{pc} + n_{pb}) \sim 0.02$)
intervals also considered. Such large proton beam density fractions have implications for
angular momentum - recent work by [50] showed that the angular momentum flux carried

by the proton beam during two encounters of PSP (E3 and E4) was surprisingly larger than that carried by the alpha particles, and therefore cannot be ignored in discussions of the angular momentum budget.

The distribution of alpha particle beam densities is peaked around $n_{\alpha b}/(n_{\alpha c}+n_{\alpha b}) \sim 0.35$ and significantly broader than the proton curve. While alpha beams are often mentioned in the literature [108, 129, 125], they are rarely fit to and we have only a handful of previous measurements to compare our results to. [49]'s large scale survey concluded that alpha VDFs in the high speed solar wind at 1AU appear to almost always be single component, but gave four example spectra of clearly non-Maxwellian alpha VDFs. Fitting to each component produced beam density ratios of $n_{\alpha b}/(n_{\alpha c} + n_{\alpha b}) \sim 0.55, 0.54, 0.40, 0.32$, in good agreement with our conclusion here, namely that alpha beams, when they do occur, tend to carry a much larger proportion of the total density than is the case for proton beams, often over 50%. We note that alpha beam density ratios being larger than proton beam density ratios is equivalent to previous statements [4, 67] that the abundance ratio in secondary populations is larger than that in primary populations, because $n_{\alpha b}/n_{pb} \geq n_{\alpha c}/n_{pc} \iff n_{\alpha b}/(n_{\alpha c}+n_{\alpha b}) \geq n_{pb}/(n_{pc} + n_{pb})$.

The right histogram in figure 5.4 shows the distribution of beam drift speeds for protons (blue) and alphas (green). On average alpha beams drift more slowly than proton beams. The proton distribution peaks at $v_d \approx 1.1v_A$, a very similar value to that found in the large scale survey of *Wind* data at 1AU [3] which had $v_d \approx 1.05v_A$. The distribution has a comparatively large tail of measurements where $v_d > 1.5v_A$ presumably corresponding to those proton VDFs with enough fast moving particles to be resonant with the right handed magnetosonic/whistler waves described in section 5.5.1 [169]. In general a proton beam drift speed of $1 \lesssim v_d/v_A \lesssim 2$ has been documented many times in the literature [107, 164]. The distribution of the alpha drift speeds on the other hand has an average $v_d \approx 0.7v_A$ and is much more narrowly peaked than the proton distribution. There is an appreciable tail of measurements with $v_d > v_A$.

The fact that the abundance ratio in the secondary populations is larger than the abundance ratio in the primary populations ($n_{\alpha b}/n_{pb} \geq n_{\alpha c}/n_{pc}$) is sometimes invoked as evidence that the secondary population must have formed deeper in the corona where the Helium abundance is higher. This doesn't necessarily have to be the case. It is conceivable that wave particle processes that act on the proton and alpha VDFs simply happen to typically produce broader shoulders (and lower drift speeds) in the alpha VDFs compared to the proton VDFs, producing what *looks* to be a higher abundance ratio in the beam populations. As of yet there has been little work done on the dynamics and evolution of specifically proton core-beam and alpha core-beam VDFs under the action of ion-scale waves. Recently however [130] performed 2.5D and 3D hybrid simulations of proton and alpha VDFs, each with super-Alfvénic beam populations. They studied the subsequent evolution of the VDFs under the action of the triggered kinetic instabilities and waves, showing that the behaviour of the VDFs during the growth, saturation, and relaxation stages is indeed measurably different between the two species.
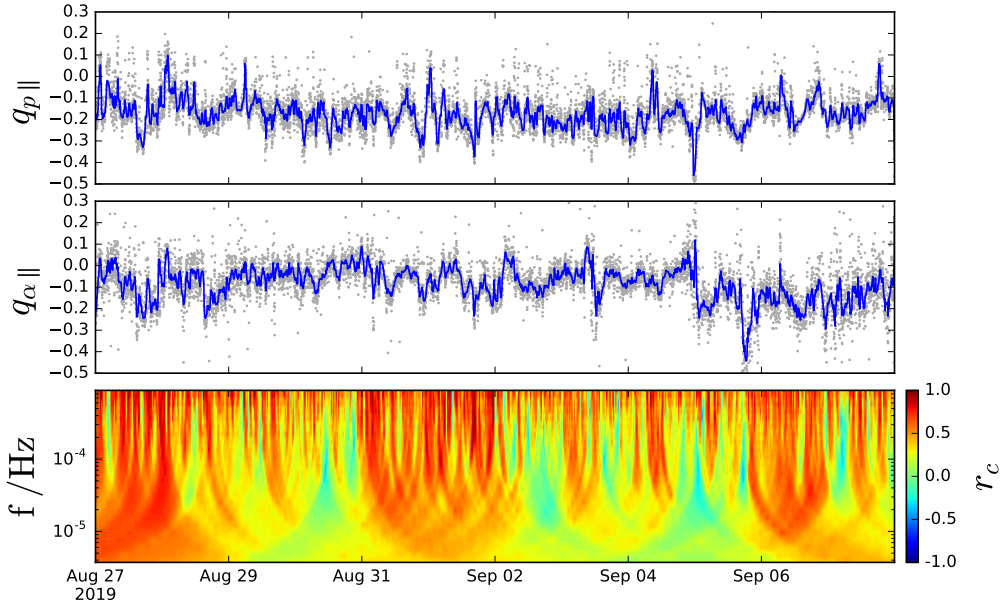
Figure 5.5: Time series of proton frame parallel heat flux $q_{p\parallel}$ (top), alpha frame parallel
heat flux $q_{p\alpha}$ (middle), and the windowed Spearman's rank correlation coefficient r_c between
them, as a function of window size expressed as a frequency (bottom).

5.5.4   Coincidence of Proton and Alpha Beams

A natural question to ask is to what extent alpha beams and proton beams occur simul-
taneously. We have established that alpha beams occur less frequently than proton beams
in the mostly slow Alfvénic wind being considered here, however we can consider whether
there is any time correlation between the skewness of the proton and alpha distributions (so
that even during "beamless" periods in the alpha distributions, the skewness of the proton
VDFs may correspondingly be smaller but still non-zero). 2D histograms of q_p vs q_α (not
shown) show very weak to no correlation. Such plots obscure any potential time localised
correlations. In figure 5.5 we plot for the entire encounter the proton frame (top panel) and
alpha frame (middle panel) normalised parallel heat flux. The third panel is a spectrogram
of the windowed Spearman's rank correlation coefficient ρ between the two species' heat
flux, for a range of different time windows. That is, for each time t and window size L, we
compute the ranked correlation coefficient of the two time series q_p and q_α over the time
window $[t - L/2, t + L/2]$, effectively producing a wavelet transform of ρ as a function of
time t and scale L. Window sizes L consist of 24 logarithmically spaced values ranging from
$L = 10$ to 2400, corresponding to time windows of $\sim$ 19 minutes to 3 days, and we use
moving windows. We use Spearman's rank correlation coefficient as opposed to Pearson's
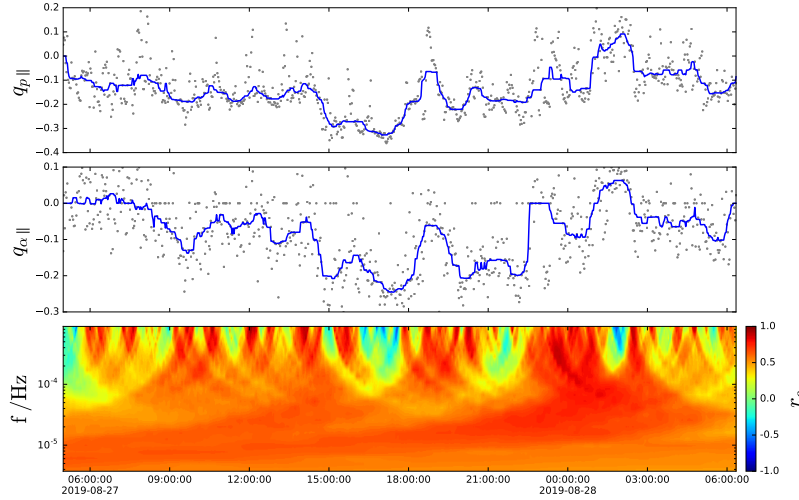
Figure 5.6: Zoomed in interval from figure 5.5, blue lines overlaid are ~ 46 minute moving medians. A very clear correlation between the fluctuations in the two species' heat fluxes can be seen.

because the absolute values of the two species' heat flux may not be correlated even if the fluctuations in their values are. No correlation between the two quantities would result in an average value of $r_c \sim 0$. From figure 5.5 we can see that there are localised periods of statistically significant ($r_c \sim 0.7$) correlations between q_p and q_α, as well as periods when the correlation is not so strong (the green periods). In Figure 5.6 we zoom in on one of these correlated time periods. The blue lines overlaid represent the moving median values with a window size of 25, or $T \sim 46$ minutes. A striking correlation between q_p and q_α is observed over this roughly day-long interval. Moreover, this correlation persists over a wide range of heat flux values in both species, that is to say q_α explores times of very prominent beams ($\sim 17:00$) as well as times of beamless distributions ($\sim 06:00$) during this day, and the proton heat flux moves in tandem, despite there being a proton beam present for essentially the entire day. It is not the case that strong correlation in heat flux only occurs when prominent beams are present in both species. From this observation we can deduce that, of the mechanisms (of which there may be several) responsible for production of beams in the solar wind, there is at least one that acts similarly upon the proton and alpha VDFs.

5.5.5 Longitudinal Variations

Having established the existence of temporal correlations between the proton and alpha frame normalised heat fluxes, we now extend the analysis to investigate any potential spatial
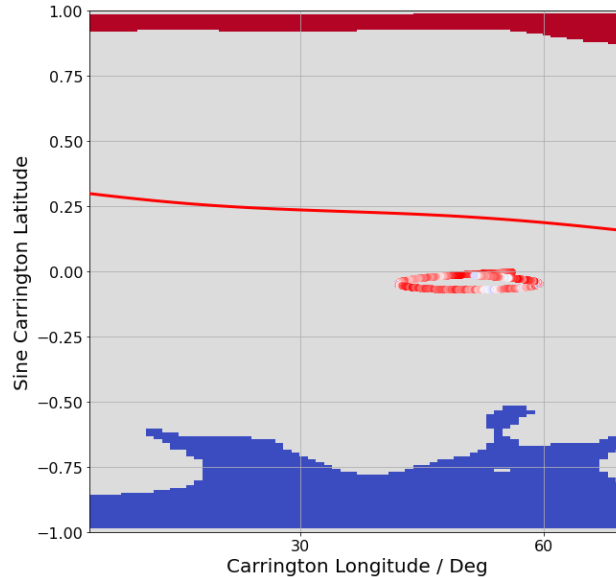
Figure 5.7: PSP's E3 orbit in Carrington coordinates, showing the locations of the HCS
(red line) and the profile of the North and South polar coronal holes.

correlations in r_c and other quantities. We make use of a Potential Field Source Surface
model [8] to map the magnetic connectivity of PSP during E3 and obtain time series as
functions of Carrington longitude. Figure 5.7 shows the projection of PSP's orbit during E3
as a function of its Carrington coordinates, with the location of the HCS indicated by the
red line. It's clearly seen that the HCS is both flat and well above PSP's orbit, making it
unlikely that processes near the current sheet are playing a significant role in the observations
discussed thus far. Recent work by [137] has provided compelling evidence of local beam
generation in the proton VDFs due to reconnection events near the HCS during PSP's 7th
and 8th encounters. However the authors point out that not all of the proton beams observed
there can be explained by reconnection, and that often beams are already clearly present
in the solar wind plasma. In a similar vein, while [97] show in situ population mixing due
to a local reconnection event at the boundary of a magnetic switchback, they conclude that
such processes can only explain a small (estimated at $\sim 2\%$) fraction of beam generation
in the solar wind. These results, and the relative distance to the HCS from PSP during
E3, means we can probably discount local reconnection events as a dominant mechanism for
beam generation in the E3 measurements.

In figure 5.8 we have taken a slice of r_c (at frequency $f = 4 \times 10^{-5}$ Hz), from figure 5.5
and plotted it versus Carrington longitude, obtained via ballistic mapping. The idea is to see
if there is any evidence for periods of correlation between proton- and alpha-frame heat flux
occurring at similar longitudes, indicating spatial structure and suggesting that processes
at or near the source surface are responsible for the periods of time-localised correlation
seen in figure 5.5. From figure 5.8 we see there may be indications of correlation at higher
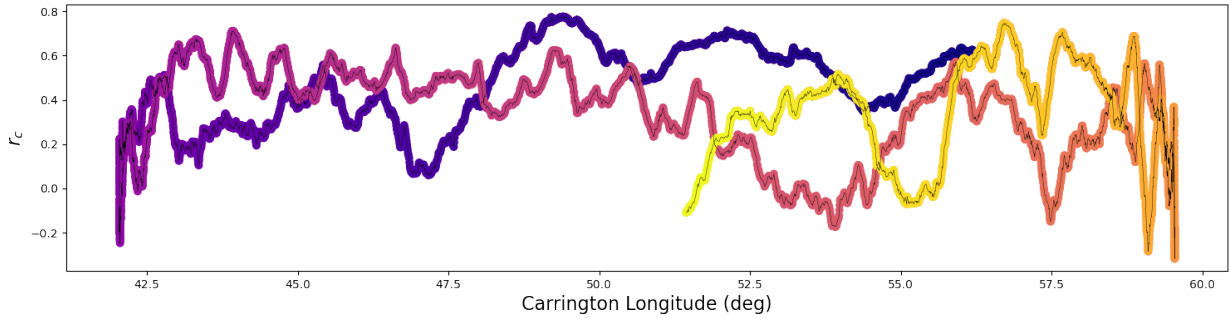
Figure 5.8: Correlation r_c of proton and alpha parallel heat flux $q_\parallel$ as a function of Carrington longitude. Colour represents time from the start (dark blue) to the end (yellow) of the encounter.

longitudes, in particular the coincident depressions around $57.5°$, and between $54 - 56°$. At lower longitudes there does not appear to be much correlation at all.

By itself, figure 5.8 is hard to interpret, as any correlations appear to be somewhat weak. As a point of comparison, in figure 5.9 we show several other solar wind parameters as functions of Carrington longitude: solar wind speed (top panel), proton parallel heat flux $q_{p\parallel}$ (middle panel), and alpha abundance n_α/n_p (bottom panel), where the colour indicates time from the beginning (dark blue) to the end (yellow) of the encounter. In the longitude range below $\sim 50°$, solar wind speed V_{SW} shows clear signs of (spatial) periodicity (especially in the peak-like features around $47°$), indicating that PSP was crossing through the same streams during these times. At longitudes greater than this there does not appear to be much correlation at all, even before PSP dropped into a slower speed stream towards the end of the encounter. The longitudinal profile of the alpha abundance n_α/n_p (bottom panel) on the other hand shows essentially no periodicity at all. The inbound and outbound Helium abundances appear completely uncorrelated, despite the clear stream structure evident in the velocity profile. This is a rather surprising result, especially as Helium abundances are frequently used as source markers of the solar wind [22, 176]. Helium abundance is known to be a sensitive function of heliographic latitude [126, 85], with lower abundances generally found in wind originating from mid-latitude coronal holes or from coronal hole boundaries, and so it's possible that the lack of spatial structure seen in the bottom panel of figure 5.9 is due to latitudinal variation in the magnetic footpoints. This could be from the tilt of PSP's trajectory itself (early PSP encounters are more tilted relative to later ones, see figure 5.7), or perhaps the presence of the coronal hole extension at $\sim 50°$ moving the footpoints up several degrees in latitude. Alternatively, we may simply be seeing the evidence of highly dynamic processes that are responsible for setting the Helium abundance at the base of the corona. Recent work by [10] showed very strong modulation of the measured alpha abundance during PSP's E6 on supergranular angular scales ($\sim 3°$), interpreted as the
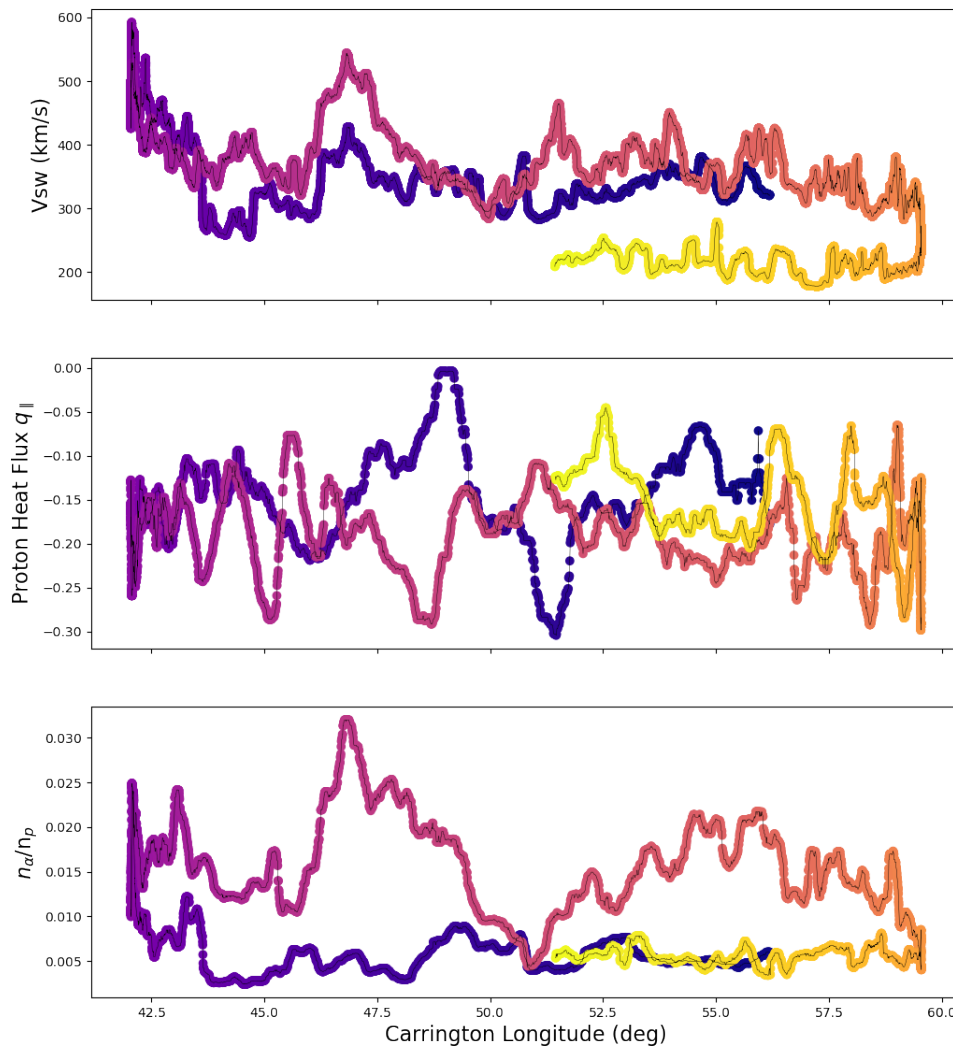
Figure 5.9: Solar wind proton velocity (top), proton parallel heat flux (middle), and alpha to proton number ratio n_α/n_p (bottom) as a function of Carrington longitude. Colour value represents time from the start (dark blue) to the end (yellow) of the encounter. Clear spatial correlation is seen in the profile of V_{SW}, but no significant correlation is seen in the other two quantities.

traversal of funnel-like spatial structures formed by the release and subsequent overexpansion of plasma from supergranule boundaries. Given that supergranules last on the order of 1-2 days [145], compared to PSP's 10 day encounter, one may be observing the lifecycle of the "microstreams" (c.f. [128]) that are responsible for setting the Helium abundance in the chromosphere/transition region before expanding out to form the fast-like CH wind. This would then result in the lack of periodicity seen in n_α/n_p when traveling back over the same Carrington longitude a few days later (we cannot directly compare to the E6 data in [10] because, in contrast to E3, PSP's E6 perihelion did not double back over the same longitudes, although it did traverse a much wider longitudinal range). We note that there are many open questions here that are beyond the scope of this current paper, and this is certainly fertile ground for future study.

Finally, the middle panel in figure 5.9 of parallel proton heat flux $q_{p\parallel}$ vs longitude shows no correlation or evidence of spatial structure. At face value this might appear to be evidence in favour of in situ proton beam generation mechanisms over those occurring at the coronal base. However, the fact that Helium abundance n_α/n_p is known to be frozen in at the solar wind source, yet did not produce a time series that showed any self-correlation as a function of longitude (as just described above), makes it difficult to conclude this. By the same reasoning, returning to figure 5.8, we hesitate to use the lack of periodicity as evidence strongly in favour of an in situ based mechanism for producing correlated heat fluxes in both the alpha and proton VDFs, and the two regions that appeared to show some spatial correlation could very well simply be coincidental (especially the feature at 57.5°, considering it is during a very clearly different stream).

5.6 Conclusions

We have analysed measurements made by the SPAN-Ion instrument [101] on board PSP of the proton and alpha VDFs during E3, with particular emphasis on the core-beam structure, which is well known in protons but has only rarely been measured or studied in the alpha particles. Several example VDFs were shown with clearly discernible core and beam populations in both species. To characterise these for the full encounter, double bi-Maxwellians were fit to both the proton and alpha VDFs (summing measurements to obtain better statistics in the alphas), but we note that the example VDFs shown exhibit many other non-thermal features that will not be well captured by a double bi-Maxwellian fit. To quantitatively measure the asymmetry of the VDF along the magnetic field direction, we compute parallel normalised heat flux, $q_\parallel$, in the centre of mass frame of each species. We argue that this is a better measure of the prominence of the beam population than simple beam density fractions or drift speeds (which are usually used in the literature), and gets around the pitfalls of fitting a double bi-Maxwellian to a VDF that is essentially beamless. Distributions of $q_\parallel$ show that during E3 proton beams were essentially ubiquitous and easily measured, and isotropic proton VDFs were rarely observed. The alpha VDFs on the other hand exhibited beams much less commonly than the protons, and were often well described as a single

population. On average proton beams drifted at a speed of $1.1v_A$ relative to the core, and carried a density fraction of $n_b/n_{tot} \approx 0.2$. Alpha beams, when they did occur, drifted more slowly ($v_d \sim 0.7v_A$) and carried a larger density fraction ($n_{\alpha b}/n_{\alpha tot} \sim 0.35$) on average when compared to the protons.

Moving window Spearman rank correlation coefficients between the alpha and proton heat flux time series showed periods of strong correlation between the two quantities, indicating a common mechanism acting on both species' VDFs to produce the beam populations, the first time such a relationship has been shown. Using a PFSS model (badman reference), we attempted to determine if such periods were spatially correlated as well (as a function of Carrington longitude), which would imply processes at the solar surface were responsible for beam generation. The observed correlation was weak, and the same was observed in the time series of just proton heat flux. Interpretation was complicated however by the fact that time series of quantities that one *would* expect to show a relatively high degree of spatial correlation (the Helium abundance) showed essentially no correlation at all. We therefore don't draw strong conclusions in favour of solar source-based vs in situ beam generation mechanisms, but believe that these methods can be expanded upon in future to settle this long-standing open question.

Chapter 6

Proton and Alpha Driven Instabilities in the Inner Heliosphere: A Case Study

6.1 Introduction

As was discussed in the previous chapter, ion VDFs in the fast-like solar wind are not in local thermodynamic equilibrium (LTE), as evidenced by the presence of temperature anisotropies ($T_\perp \neq T_\parallel$) and drifts between different particle populations. These departures from LTE represent sources of free energy that are available to drive kinetic micro-instabilities and produce a variety of plasma waves. In turn the particles are scattered by the presence of these waves, which therefore have an isotropising effect on the VDFs, driving them back towards LTE and limiting the free energy available to drive the instability. This is to be contrasted with the ineffective regulating effect of Coulomb collisions on ion VDFs, given that in the fast wind, the Coulomb collisional age $A_c \lesssim 1$ at 1AU [3], and is therefore even more negligible at PSP distances [110] (justifying the frequent assumption of fast solar wind being collisionless). Such plasma waves are directly measurable in magnetic and electric field data [28] and often probed via examination of magnetic field power spectra, magnetic field ellipticity (polarisation), Poynting vectors, etc. In this final chapter we study in detail one such ion-scale wave event, modelling the plasma with core and beam populations for both the protons and the alpha particles.

Empirically [76, 78, 77, 59, 168, 27], it suffices to restrict attention to quasi-parallel propagation with $\mathbf{k} \times \mathbf{B} = 0$, in which case there are three main types of ion instability driven modes physically relevant in the solar wind. Alfvén/Ion Cyclotron (A/IC) instabilities are triggered by temperature anisotropies with $T_\perp/T_\parallel > 1$ and produce left-handed (LH) circularly polarised waves in the particles' rest frame. Fast magnetosonic/whistler (FM/W) instabilities produce right-handed (RH) circularly polarised waves and are driven by temperature anisotropies with $T_\perp/T_\parallel < 1$. Finally, ion/ion component instabilities are caused

by relative drifts between particle populations.

Traditionally, statistical analyses of the role that temperature anisotropy driven instabilities play in the solar wind have focussed on parameterising instability thresholds as functions of the temperature anistropy $R = T_\perp/T_\parallel$ and parallel plasma beta $\beta_\parallel$ only, and plotting the data as functions of these two parameters ("Brazil plots"). Given the large number of free parameters available when modelling solar wind plasma (each bi-Maxwellian comes with 6 for a start), flattening the data onto a 2D parameter space may seem overly restrictive. However, the excellent agreement between the distribution of proton measurements in the $(R_p, \beta_{p,\parallel})$ plane and instability contours of constant growth rate [82, 58, 70, 13, 118], as well as statistical enhancements in the amplitude of magnetic field fluctuations at the boundaries of these measurements [13], is strong evidence that a) various kinetic instabilities are indeed active in the solar wind and are limiting the range of proton temperature anisotropies, and b) R_p and $\beta_{p,\parallel}$ are good choices of physically relevant parameters and order the data well. Moreover, this effect has also been observed in the alphas [58, 114], suggesting analogous mechanisms at work. Another concern regarding the unreasonable effectiveness of linear theory in constraining observations is raised when comparing linear vs non-linear timescales; non-linear turbulent growth rates are usually found to be faster than linear growth rates, suggesting that the assumptions of linear theory of a uniform, homogeneous background (so that a Fourier transform can be performed) should break down due to turbulence. However, recent work [17] has shown that this timescale ordering is reversed near the instability thresholds, causing kinetic instabilities to dominate precisely near the bounds where we observe the solar wind measurements to be constrained.

In the case of ion/ion drift instabilities, it is the right-handed resonant instability that is usually considered to be more important in the solar wind [118], as under reasonable assumptions [56] there are too few particles available for resonance with the LH mode (we note that this is not the case in higher beta wind [172]). These instabilities impose "speed limits" on both proton beam-core drifts [107, 63, 164] and alpha-proton drifts [64, 57, 24, 171, 117], and a good intuitive description of how these modes become stable or unstable (via quasilinear diffusion) as a function of drift speed is given in [171].

Wave damping via the ion cyclotron resonance is one mechanism by which the energy in Alfvénic turbulence can be dissipated, leading to perpendicular heating. Remote sensing observations of coronal temperatures show large ion temperature anisotropies, indicative of this process taking place [39, 38, 158]. Broadly speaking, radial ion temperature profiles show slower than expected decreases in the perpendicular direction and faster than expected decreases in the parallel direction when compared to simple adiabatic cooling [118, 154]. Case studies of wave events like the one in this chapter add to our understanding of the detailed processes responsible for shaping the solar wind ion VDFs as they travel outwards and the mechanisms of energy exchange between particles and waves.

This chapter is organised as follows. In the next section we give a recap of linear Vlasov analysis and the solution of the warm plasma dispersion relation. Section 6.2 outlines our methods and section 6.3 presents the interval under study. In section 6.4 we give the results

of the instability analysis, breaking the wave event into sub-intervals, and perform Doppler shift calculations to compare predicted wave frequencies and polarisations in the spacecraft frame with the magnetic field measurements. Finally in section 6.5 we give a summary of our findings.

6.1.1 Normal Mode Analysis and Linear Vlasov Theory

We give here a brief recap of the method for calculating plasma normal modes in the cold and warm plasma regimes, and determining their stability. Starting with Maxwell's equations

$$\nabla \times \mathbf{E} = -\frac{1}{c}\frac{\partial \mathbf{B}}{\partial t} \tag{6.1}$$

$$\nabla \times \mathbf{B} = \frac{4\pi\mathbf{j}}{c} + \frac{1}{c}\frac{\partial \mathbf{E}}{\partial t} \equiv \frac{1}{c}\frac{\partial \mathbf{D}}{\partial t}, \tag{6.2}$$

where $\mathbf{D}$ is the displacement field, related to the electric field via the dielectric tensor ϵ

$$\mathbf{D} = \epsilon \cdot \mathbf{E}, \tag{6.3}$$

we Fourier transform them to get

$$\mathbf{k} \times \mathbf{E} = \frac{\omega}{c}\mathbf{B} \tag{6.4}$$

$$\mathbf{k} \times \mathbf{B} = -\frac{4\pi i}{c}\mathbf{j} - \frac{\omega}{c}\mathbf{E} = -\frac{\omega}{c}\epsilon \cdot \mathbf{E}. \tag{6.5}$$

Taking the curl of equation 6.4 to eliminate $\mathbf{B}$ from equation 6.5, we obtain the wave equation,

$$\mathbf{k} \times (\mathbf{k} \times \mathbf{E}) + \frac{\omega^2}{c^2}\epsilon \cdot \mathbf{E} = 0, \tag{6.6}$$

which is usually written in terms of the refractive index $\mathbf{n} = \omega\mathbf{k}/c$ as $\mathbf{n} \times (\mathbf{n} \times \mathbf{E}) + \epsilon \cdot \mathbf{E} \equiv \mathcal{D}(\omega, \mathbf{k}; \mathcal{P}) \cdot \mathbf{E} = 0$, or in matrix form:

$$\begin{pmatrix} \epsilon_{xx} - n_z^2 & \epsilon_{xy} & \epsilon_{xz} + n_x n_z \\ \epsilon_{yx} & \epsilon_{yy} - n^2 & \epsilon_{yz} \\ \epsilon_{zx} + n_x n_z & \epsilon_{xy} & \epsilon_{xz} - n_x^2 \end{pmatrix} \begin{pmatrix} E_x \\ E_y \\ E_z \end{pmatrix} = 0. \tag{6.7}$$

The normal modes of the plasma are therefore determined by solving the *dispersion relation*

$$\det \mathcal{D}(\omega, \mathbf{k}; \mathcal{P}) = 0. \tag{6.8}$$

Here $\mathcal{P}$ represents a set of plasma parameters, which will implicitly appear in the components of ϵ. In practice then the problem reduces to calculating the components of the dielectric tensor ϵ under whichever approximations and plasma regimes are deemed relevant to the problem at hand, for instance which plasma species are present, the precise forms of the

VDFs if kinetic effects are important (Maxwellian, bi-Maxwellian, kappa, etc.), if the plasma
is collisional, and so on. ϵ is calculated via the constitutive relations

$$\mathbf{j} = \sigma \cdot \mathbf{E} \equiv -\frac{i}{\omega}\chi \cdot \mathbf{E}, \tag{6.9}$$

where σ is the conductivity and χ the susceptibility tensor. Substituting equation 6.9 into
equation 6.5 we have $\epsilon(\omega, \mathbf{k}) = \mathbb{I} + \chi$. Since equation 6.5 is linear, this relation is often
written explicitly to show the individual contributions to ϵ from each species s:

$$\epsilon(\omega, \mathbf{k}) = \mathbb{I} + \sum_s \chi_s. \tag{6.10}$$

In the cold plasma regime, one solves the fluid momentum equation (which reduces to the
equation for a single particle moving in $\mathbf{E}$ and $\mathbf{B}$ fields in the limit $T \to 0$) for the fluid
velocities $\mathbf{v}_s$. This then gives the current $\mathbf{j}$ via $\mathbf{j} = \sum_s n_s q_s \mathbf{v}_s$ (as a function of $\mathbf{E}$), from
which χ and ϵ can be read off using equations 6.9 and 6.10. In the warm plasma regime, the
starting point is taken to be the Vlasov equation, or the collisionless Boltzmann equation:

$$\frac{\partial f_s}{\partial t} + \mathbf{v} \cdot \frac{\partial f_s}{\partial \mathbf{r}} + \frac{q_s}{m_s}\left(\mathbf{E} + \frac{\mathbf{v} \times \mathbf{B}}{c}\right) \cdot \frac{\partial f_s}{\partial \mathbf{v}} = 0, \tag{6.11}$$

where f_s is the VDF corresponding to species s. In linear Vlasov theory, one perturbs f_s, $\mathbf{E}$,
and $\mathbf{B}$ about their (known) background values,

$$f_s = f_s^{(0)} + f_s^{(1)} + \dots \tag{6.12}$$

$$\mathbf{E} = \mathbf{E}^{(0)} + \mathbf{E}^{(1)} + \dots \tag{6.13}$$

$$\mathbf{B} = \mathbf{B}^{(0)} + \mathbf{B}^{(1)} + \dots \tag{6.14}$$

to obtain an equation for $f_s^{(1)}$:

$$\left(\frac{Df_s^{(1)}}{Dt}\right)_0 \equiv \frac{\partial f_s^{(1)}}{\partial t} + \mathbf{v} \cdot \frac{\partial f_s^{(1)}}{\partial \mathbf{r}} + \frac{q_s}{m_s}\left(\frac{\mathbf{v} \times \mathbf{B}_0}{c}\right) \cdot \frac{\partial f_s^{(1)}}{\partial \mathbf{v}} \tag{6.15}$$

$$= -\frac{q_s}{m_s}\left(\mathbf{E}^{(1)} + \frac{\mathbf{v} \times \mathbf{B}^{(1)}}{c}\right) \cdot \frac{\partial f_s^{(0)}}{\partial \mathbf{v}}, \tag{6.16}$$

where $(Df_s/Dt)_0$ represents the convective derivative of f_s along the *unperturbed* trajectory.
Equation 6.16 is then solved (using e.g. the method of unperturbed orbits, see Stix Ch.
10) for a given zeroth order distribution function $f_s^{(0)}$. Finally, $f_s^{(1)}$ is used to compute the
perturbed current as a function of $\mathbf{E}^{(1)}$,

$$\mathbf{j}^{(1)} = \sum_s q_s \int d^3\mathbf{v} \, \mathbf{v} f_s^{(1)} \tag{6.17}$$

from which the susceptibilities can again be read off using equation 6.9 and the components of $\mathcal{D}(\omega, \mathbf{k}; \mathcal{P})$ calculated. For a given $\mathbf{k}$ (taken to be real) and set of plasma parameters $\mathcal{P}$, the normal mode solutions ω to the dispersion relation $\det \mathcal{D}(\omega, \mathbf{k}; \mathcal{P}) = 0$ will in general be complex, $\omega = \omega_r + i\gamma$, where ω_r is the real frequency and γ the growth rate. Given the time dependence of our first order quantities $\sim e^{i(\mathbf{k} \cdot \mathbf{r} - \omega t)}$, a positive growth rate $\gamma > 0$ represents an unstable, growing mode, and $\gamma < 0$ one that is damped.

With this in mind, an elegant method for determining the overall stability of our system is to use Nyquist's Criterion. Considering $\det \mathcal{D}(\omega, \mathbf{k}; \mathcal{P})$ as a complex valued function over the complex variable ω, the contour integral

$$W_n = \frac{1}{2\pi i} \oint_C \frac{d\omega}{\det \mathcal{D}(\omega, \mathbf{k}; \mathcal{P})} \qquad (6.18)$$

taken over the upper half plane *counts* the number of normal modes with $\gamma > 0$ (via the residue theorem, since these zeros will appear as poles). Thus a value of $W_n > 0$ represents a system that is linearly unstable with respect to at least one mode, and $W_n < 0$ one that is linearly stable.

To calculate γ_{max}, the growth rate of the maximally unstable (and therefore most physically relevant) mode, and its associated ω_r, the contour C can start below the real axis and iteratively be moved upwards until $W_n = 0$. The value at which W_n vanishes will give the maximum growth rate γ_{max}. ω_r for this most unstable mode can then be computed via use of a simple root-finding algorithm (Newton-Raphson or bisection) along the line $\gamma = \gamma_{\mathrm{max}}$. This scheme is illustrated in the cartoon in figure 6.1, where $W_n = 4$. Here the modes (red dots) are symmetrically distributed about the imaginary axis $\omega_r = 0$, which will always be the case if the VDF is symmetric (forwards and backwards are equivalent). The drifting beam populations considered in this study however break this symmetry resulting in a non-symmetric distribution of modes. Finally, one can repeat this process of

Figure 6.1: Nyquist's Criterion showing $W_n = 4$. Red dots indicate the normal modes $\det \mathcal{D}(\omega, \mathbf{k}; \mathcal{P}) = 0$. The bottom of the contour C is iteratively moved up until $W_n = 0$.

computing the winding number over a range of $\mathbf{k}$ vectors to find the most unstable mode $(\gamma_{\mathrm{max}}, \mathbf{k}_{\mathrm{max}}, \omega_r)$. We have explained here in brief the method employed by the PLUME warm

plasma dispersion solver [90], which we employ to analyse the SPAN-Ion measurements in section 6.4.

An alternate method for computing growth rates can be derived starting from Poynting's theorem. One can show ([157], Chapter 4) that the dissipation or absorption of wave energy is captured by the anti-Hermitian part of the dielectric tensor. The rate of energy absorption/emission (i.e. the power P) is given by

$$P = \frac{\omega_r}{8\pi} \mathbf{E}^* \cdot \epsilon_a \cdot \mathbf{E}, \tag{6.19}$$

where $\epsilon_a = (\epsilon - \epsilon^\dagger)/2i$ is the anti-Hermitian part of ϵ, and $\mathbf{E}$ the oscillating electric field associated with any given wave mode. Once again using the linearity of the dielectric tensor in equation 6.10, we have that

$$P \equiv \sum_s \gamma_s = \frac{\omega_r}{8\pi} \sum_s \mathbf{E}^* \cdot \chi_{a,s} \cdot \mathbf{E}, \tag{6.20}$$

where $\chi_{a,s}$ is the anti-Hermitian part of the susceptibility tensor for species s. This gives a very convenient way of computing the contributions to overall wave power absorption/emission *from each species s*: once the dispersion relation equation 6.8 has been solved, compute the eigenvectors $\mathbf{E}$ for each mode, then plug them into equation 6.20 to calculate the individual species contributions. This allows us to define individual species growth rates γ_s which we refer to extensively in the discussion that follows.

6.2 Method

6.2.1 Data

The interval we analyse here is taken during the inbound portion of PSP's fourth encounter, from 2020-01-26/13:10:00 to 2020-01-26/15:30:00, and is shown in figure 6.2. High resolution magnetic field measurements from the FIELDS magnetometer [14] are shown in panel (a) in spacecraft coordinates (blue, green, red represent x, y, z components respectively). A Morlet wavelet transform, as in Chapter 3 equation 3.1, is applied to these measurements to compute the magnetic field power spectrum as a function of frequency and time, shown in panel (b). This has been normalised by a Kolmogorov $f^{-5/3}$ power spectrum, with the idea being that excess power will show up as bumps above this background, highlighting coherent wave activity (see for instance figure 3 in [181] or figure 2 in [27]). Panel (c) plots the perpendicular polarisation of the magnetic field, which from a practical point of view is the most important quantity, as coherent wave activity shows up as bright, easily identifiable red (RH) or blue (LH) bands, at or around the proton gyrofrequency. The power in the left- and right-handed components is computed as

$$P_L(t, f) = |B_x(t, f) - iB_y(t, f)|^2 \tag{6.21}$$
$$P_R(t, f) = |B_x(t, f) + iB_y(t, f)|^2, \tag{6.22}$$
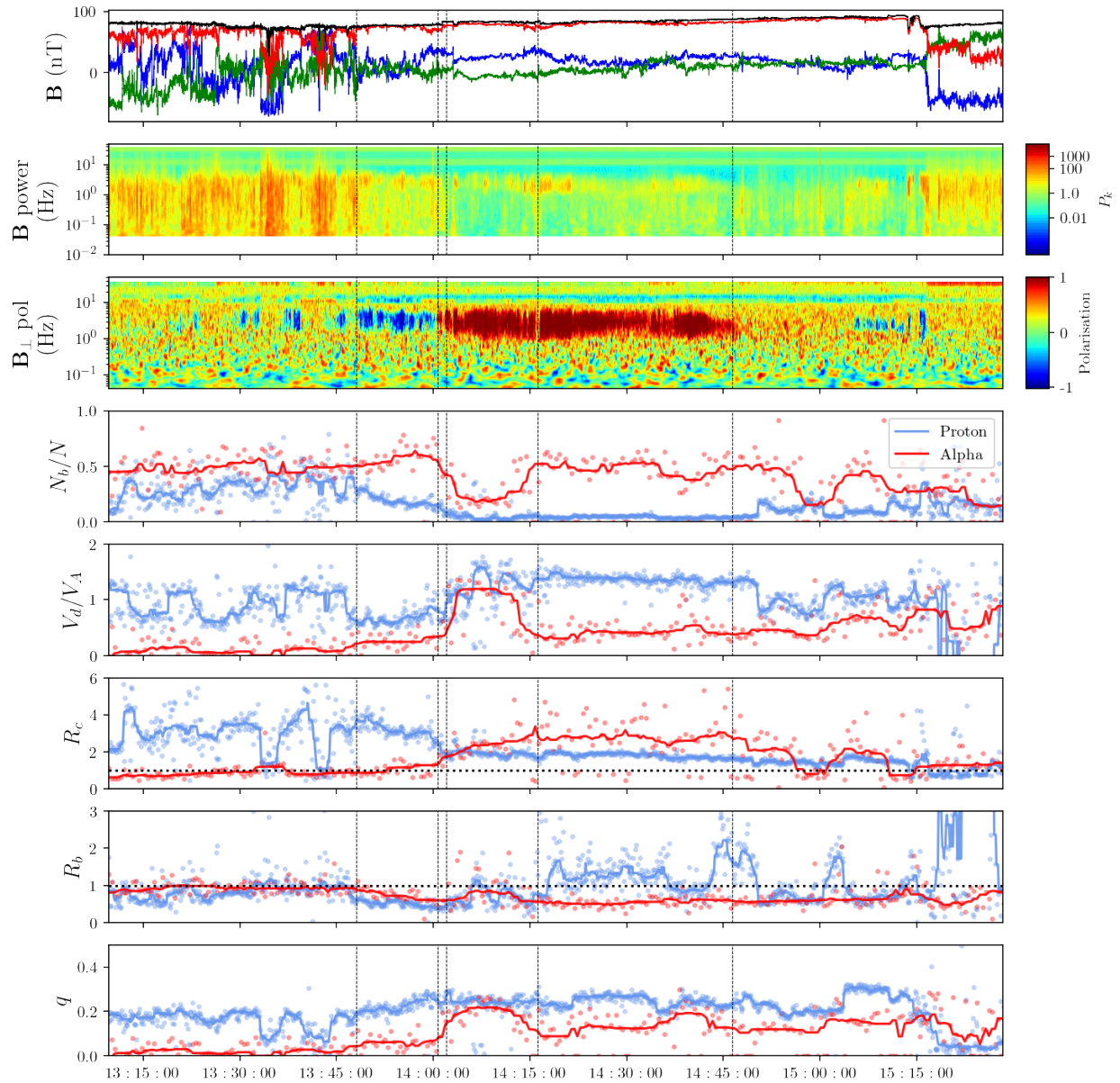
Figure 6.2: Ion scale wave event interval showing a period of coherent wave power and
polarisation coincident with both proton and alpha particle beam populations. Panels from
top to bottom are magnetic field **B** in spacecraft coordinates, magnetic field power spectrum,
magnetic field perpendicular polarisation, proton (blue) and alpha (red) beam density ratio,
beam drift speed as a fraction of the local Alfvén speed V_d/V_A, core temperature anisotropy
$R_c = T_{c\perp}/T_{c\parallel}$, beam temperature anisotropy $R_b = T_{b\perp}/T_{b\parallel}$, and normalised heat flux q. Solid
lines in the bottom four panels are moving window medians (15 measurement points wide).

where $B_i(t, f)$ are the i-th components of the wavelet transform of **B**, from which the perpendicular polarisation is defined as the normalised difference

$$\text{Pol}(t, f) = \frac{P_R(t, f) - P_L(t, f)}{P_R(t, f) + P_L(t, f)}. \tag{6.23}$$

With this representation note that a polarisation of 0 doesn't necessarily mean $P_R = P_L = 0$; it is possible that two modes are concurrently present and that polarisation in the LH component is cancelling out polarisation in the RH component.

6.2.2 Fits

As in Chapter 5, we perform fits to the SF00 spectra at their native cadence of 7s, fitting a bi-Maxwellian distribution to both the proton core and beam populations. To the alpha SF01 channel, we also fit a bi-Maxwellian distribution to the alpha core and beam, with one additional parameter ϵ to capture the proportion of protons leaking into the SF01 channel. In order to get slightly better statistics, two SF01 spectra are summed together per fit. The results from these fits are shown as blue (proton) and red (alpha) dots in figure 6.2, with moving window median filters overlaid on top (a window size of 15 measurement points was used). When we require the plasma density to compute the Alfvén speed V_A, or the proton density in computing the alpha abundance ratio $N_{\alpha p} = N_\alpha / N_p$, we don't use the fitted proton density but in both cases instead use electron density values computed via extraction of the plasma frequency line from FIELDS RFS spectra [147], as was done in Chapter 4, making the reasonable approximation that $N_p \approx N_e$ as the alpha abundance is quite low, around $2 - 3\%$ throughout this interval.

6.3 Event Interval

The event interval in figure 6.2 is characterised by a very quiet, fairly radially aligned magnetic field of almost constant field strength, lasting approximately 90 minutes, corresponding to one of the quiet interstitial periods between switchback patches [10, 45]. Previous studies [27, 168] of ion scale wave storms in PSP data have tended to focus on similar quiet field intervals. It has been suggested this may be because the polarisation signatures are more easily observed during quiet field times, and that turbulent power in the perpendicular directions is swamping them during the switchback patches. Here the wave event itself is very clearly delineated by a strong LH polarisation signature from around 13:45 to 14:00, in a frequency band of roughly $1 - 6$ Hz, and a strong RH polarisation signature from around 14:00 to 14:45 over a similar frequency range. The very clear and abrupt switch from a prolonged period of LH to RH polarisation at 14:00 is somewhat unusual and one of the main reasons this interval was chosen for further study. In addition, there appears to be a slight modulation with time in the bandwidth of the RH polarisation signature, being in general more broad than the LH period. The aim of this case study is to see whether these observations can be

explained and understood within the context of linear Vlasov theory, in particular whether we can predict and identify the unstable wave modes that are being measured, determine which particle species are responsible for either driving or damping the modes, and tie the sudden shift from LH to RH polarisation to any changes in the plasma parameters.

6.3.1 Sub-Intervals

For convenience we split the interval into 4 sub-intervals, denoted P1 to P4, as follows:

1. **P1**: 2020-01-26/13:48:05 to 2020-01-26/14:00:45. Period of continuous LH polarisation. The proton VDFs are characterised by a prominent beam, drift speed $V_d \sim 0.7V_A$, . The alpha VDFs are fairly isotropic with a small $q_\alpha \sim 0.05$.

2. **P2**: 2020-01-26/14:00:45 to 2020-01-26/14:02:00. A brief, measurable gap between the strong LH and RH polarisation periods, containing 4 SPAN-Ion fits.

3. **P3**: 2020-01-26/14:02:00 to 2020-01-26/14:16:10. Period of RH polarisation coincident with a very fast ($V_d \gtrsim 1.1V_A$), low density ($N_b/N \sim 0.2$), prominent alpha beam ($q_\alpha \sim 0.2$).

4. **P4**: 2020-01-26/14:16:10 to 2020-01-26/14:46:25. Remaining period of RH polarisation (a small gap between the RH polarisation signatures of P3 and P4 is resolvable in the magnetic field data, but not at our fitted SPAN cadences). By eye there seems to be appreciable modulation in the polarisation envelope as well as fluctuations in the central frequency during P4.

The sub-intervals P1 to P4 are demarcated in figures 6.2 and 6.4 with vertical lines. Interval P1 is characterised by a continuous period of LH magnetic field polarisation. From figure 6.2 we can see that the proton VDF has a relatively dense ($N_{pb}/N \sim 0.2$) and slow ($V_{pd} \sim 0.6V_A$) beam population, with a very anisotropic core, $R_p \gtrsim 3$. The proton beam density fraction gradually decreases through P1. The alphas on the other hand are almost isotropic (although slightly less so than in the times preceding P1), with a close to negligible beam component. While an alpha beam density ratio of $N_{\alpha b}/N \sim 0.5$ in panel (d) might suggest a prominent beam, a glance at the drift speed, $V_{\alpha d} \sim 0.15V_A$, and the normalised parallel heat flux $q_\alpha \sim 0.05$, shows that this is not the case. Per our discussion in Chapter 5 section 5.5.2, we again see the utility of computing q in distinguishing between these two scenarios, of a prominent beam vs merely fitting two similar sized bi-Maxwellians under one larger one. The second row in figure 6.3 shows an example proton (left) and alpha (middle) VDF from P1, as well as $f(v)$ summed over all angles. The small alpha beam and relatively slow drifting proton beam are both readily visible. For contrast, the top row in figure 6.3 shows VDFs from 13:28:10, right at the start of the interval in figure 6.2, where there are no LH or RH polarisation signatures and the plasma is, at first glance, stable. The alpha VDF is clearly much closer to isotropy and the proton beam is also less prominent.
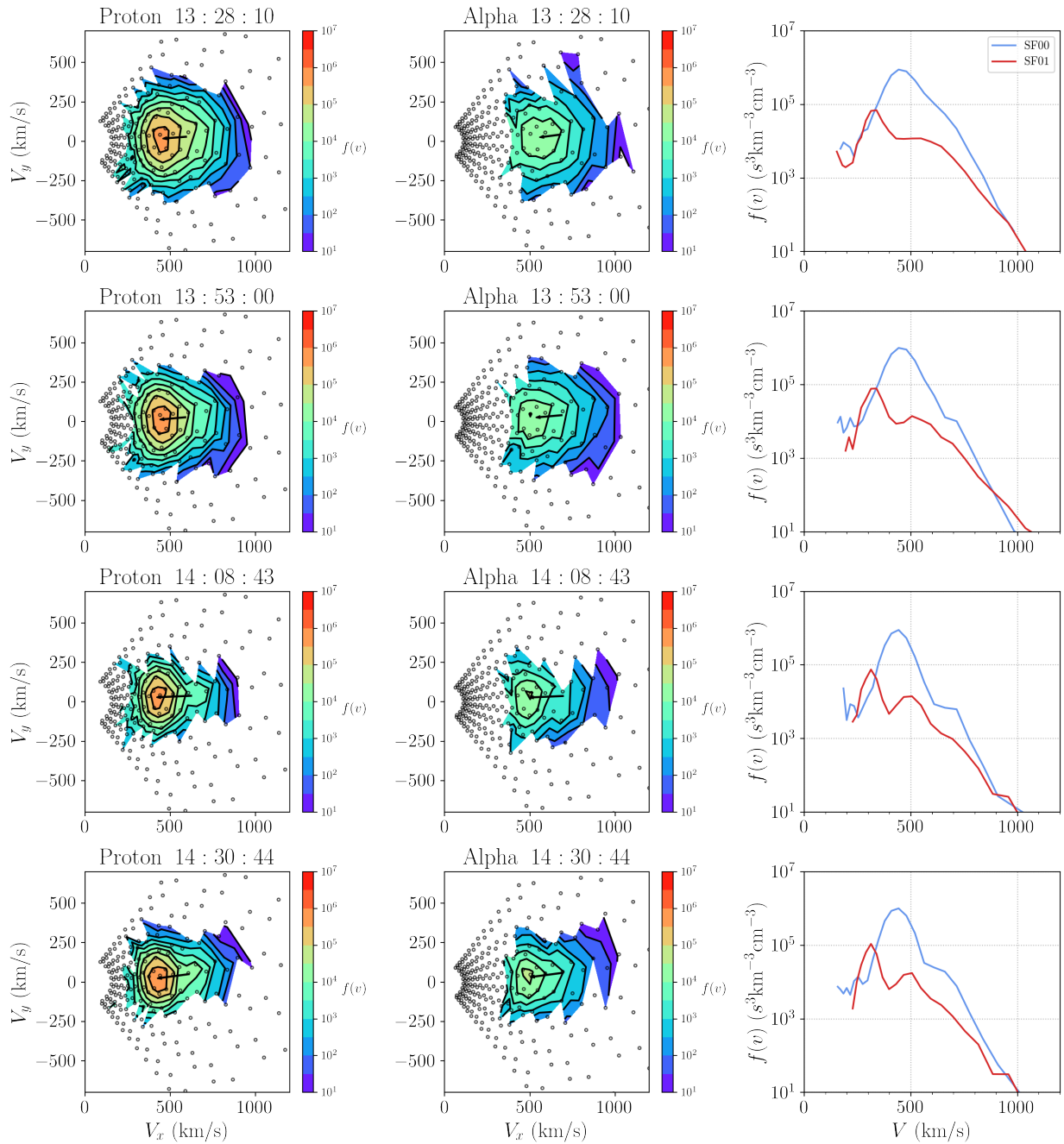
Figure 6.3: Example proton and alpha VDFs, as well as 1D profiles of $f(v)$ of the SF00 and SF01 spectra at four different times. First time is from the beginning of the period shown in figure 6.2, with no LH or RH polarisation.

A dramatic rearrangement of the VDFs occurs during P2 (the small gap in visible LH and RH polarisation) and P3, the first part of the RH polarisation. The proton beam density fraction N_{pb}/N falls to between 0.05 and 0.1, while the drift speed increases to between 1.1 and $1.4V_A$, constituting a very fast, low density beam. The proton core anisotropy also very suddenly drops from $R_p \sim 3$ to just below $R = 2$. At the same time, a prominent alpha beam abruptly appears, with a density fraction of $N_{\alpha b}/N \sim 0.15$, and a drift speed $V_{\alpha d} \sim 1.2V_A$. The alpha core anisotropy steps upwards from $R_\alpha \lesssim 1$ to $R_\alpha \sim 1.5$ and continues to increase throughout P3. The change in R_α throughout P3 is much more gradual compared to the step-like changes in $N_{\alpha b}/N$ and $V_{\alpha d}/V_A$. Example alpha and proton VDFs from P3 are shown in the third row of figure 6.3, where the lower density, more tenuous beams are made clear.

From P3 to P4 there are no significant changes in the proton beam and core parameters. The proton beam density fraction remains around $N_{pb}/N \sim 0.05$, with a remarkably steady drift speed around $1.3V_A$ and the core anisotropy around $R_p \sim 2$. The very fast alpha beam characterising P3 is no longer present in P4, but is abruptly replaced by a slower moving ($V_{\alpha d} \sim 0.4V_A$) and more dense ($N_{\alpha b}/N \sim 0.5$) beam. The alpha heat flux q_α remains significantly higher than in P1. No such abrupt changes between P3 and P4 are observed in the core anisotropy R_α, it remains elevated throughout this entire period of RH polarisation. Example VDFs from P4 are shown in the fourth row of figure 6.3.

6.3.2 Fluid Parameters

In figure 6.4 we plot the macroscopic fluid parameters during the interval. In particular, the alpha to proton number density ratio $N_{\alpha p}$, alpha proton drift speed $(V_\alpha - V_p)/V_A$ (where we use the centre of mass velocities for each species s, $\mathbf{V}_j = (n_{sc}\mathbf{V}_{sc} + n_{sb}\mathbf{V}_{sb})/(n_{sc} + n_{sb})$, and $V_s = |\mathbf{V}_s|$), the total parallel and perpendicular temperatures $T_\perp, T_\parallel$, and the total temperature anisotropies $R_s = T_{s,\perp}/T_{s,\parallel}$. Total temperatures for each species are calculated using

$$T_\perp = \frac{n_c T_{\perp,c} + n_b T_{\perp,b}}{n_c + n_b} \tag{6.24}$$

$$T_\parallel = \frac{1}{n_c + n_b}\left(n_c T_{\parallel,c} + n_b T_{\parallel,b} + \frac{n_c n_b}{n_c + n_b}mv_d^2\right) \tag{6.25}$$

where v_d is the drift speed between the core and beam populations. Focussing on the sub-intervals just discussed, from figure 6.4 we can see that neither the alpha abundance nor the alpha-proton drift speed change significantly, with a slight decrease in the alpha-proton drift speed at the start of the RH interval P3. $N_{\alpha p}$ also remains fairly constant at just below 2%. The centre of mass speeds V_p and V_α are remarkably constant, particularly V_p. The temperatures of both species drop near the beginning of P3, before becoming very steady. The temperature anisotropies however don't vary much between P1 and P3-P4, with $R_\alpha < 1$ and $R_p \gtrsim 1$ throughout. Compared to the individual beam and core parameters shown in figure 6.2, the changes in the bulk fluid parameters are much less sharp and much less drastic. These parameters can be used to examine the stability of the plasma to the long wavelength
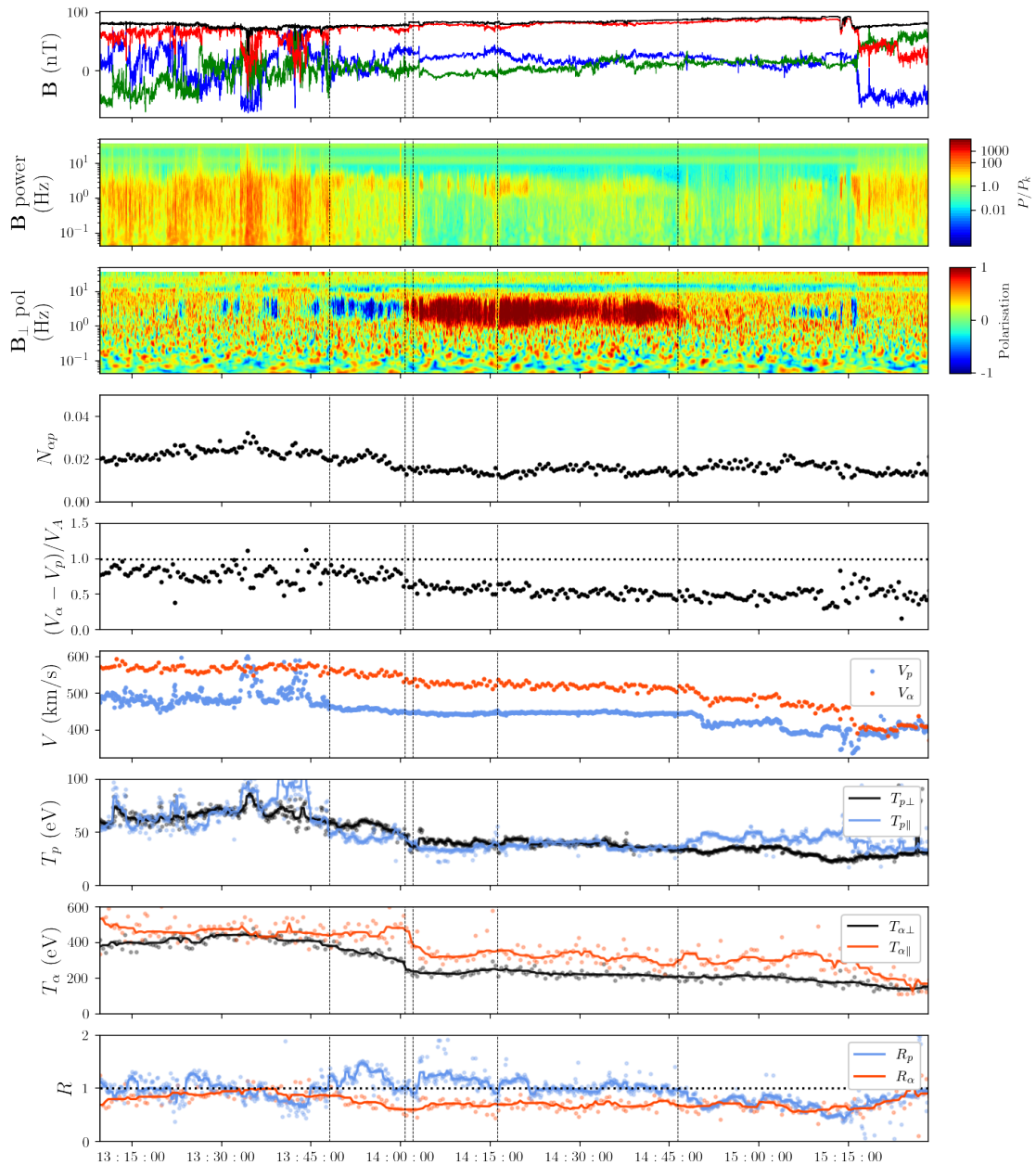
Figure 6.4: Same event interval as in figure 6.2 showing macroscopic plasma parameters. Panels are magnetic field **B** in spacecraft coordinates, magnetic field power spectrum, magnetic field perpendicular polarisation, alpha to proton number density ratio, alpha to proton drift speed normalised by the Alfvén speed, proton (blue) and alpha (red) centre of mass speeds, proton parallel (blue) and perpendicular (black) temperatures, alpha parallel (red) and perpendicular (black) temperatures, and total temperature anisotropies.

(i.e. fluid) mirror [68] and firehose instabilities [92], via computation of the parameters

$$\Lambda_M = \sum_s \beta_{s\perp} \left(\frac{T_{s\perp}}{T_{s\parallel}} - 1 \right) - \frac{\left(\sum_s \rho_s \frac{T_{s\perp}}{T_{s\parallel}} \right)^2}{2 \sum_s \frac{\rho_s^2}{\beta_{s\parallel}}} \tag{6.26}$$

and

$$\Lambda_F = \frac{\beta_\parallel - \beta_\perp}{2} + \frac{\sum_s n_s m_s |\Delta V_s|^2}{\sum_s n_s m_s V_A^2}, \tag{6.27}$$

where $\rho_s = q_s n_s$ is the charge density, ΔV_s the speed relative to the centre of mass, and total β's are given by $\beta_\perp = \sum_s \beta_{s,\perp}, \beta_\parallel = \sum_s \beta_{s,\parallel}$. The plasma is considered unstable to each instability if their respective parameter exceeds 1. For this interval neither Λ_M nor Λ_F come close to reaching this threshold. The point here is that the instabilities active and causing the wave activity observed during this interval are truly *kinetic*, not fluid, instabilities. In particular, this means that any changes in the associated wave observables (polarisation, wave power, wave frequency), are not due to changes in large scale macroscopic quantities, but must be due to changes in the microstructure of the VDFs. From examining figures 6.2 and 6.4, this clearly involves redistribution of thermal energy between the core and beam populations of each species, since the *overall* parallel and perpendicular temperatures are relatively unchanged throughout. The free energy driving these waves derives from the drifts and temperature anisotropies of the individual components of the particle VDFs, and their resultant coupling to the electromagnetic fields.

6.4   Instability Analysis

6.4.1   PLUME Dispersion Solver

To analyse this interval we make use of the PLUME dispersion relation solver [89], whose principle calculation method was sketched out in section 6.1.1. PLUME solves the warm plasma dispersion relation for an arbitrary number of drifting bi-Maxwellian distribution functions (i.e. the zeroth-order distribution function $f^{(0)}(\mathbf{v})$ in the linearised Vlasov equation 6.16 is taken to be a bi-Maxwellian function of $v_\perp$ and $v_\parallel$ only). In our case this means five population VDFs - proton core, proton beam, alpha core, alpha beam, and the electrons. The electron density and velocity are calculated from the ion fits in order to enforce charge and current neutrality. One population, in our case the proton core, is assigned to be the reference population, and all calculations are performed in this frame. Most importantly, derived wave frequencies ω_r are in the frame of the proton core. Drift speeds of the other particle populations are defined relative to the reference population, and are assumed to all lie along $\mathbf{B}$. This is a slightly more restrictive requirement than is imposed by the fitting routines on the SPAN-Ion data, as while beam populations are assumed to lie parallel to $\mathbf{B}$ relative to their respective cores, the alphas are not assumed to lie along $\mathbf{B}$, relative to the protons. The set of plasma parameters $\mathcal{P}$ used as input in solving the dispersion

relation $\det \mathcal{D}(\omega, \mathbf{k}; \mathcal{P}) = 0$ consists of the three parameters defining the reference proton core population:

$$\mathcal{P}_c = \left\{ \beta_{\parallel,c}, \frac{w_{\parallel,c}}{c}, \frac{T_{\perp,c}}{T_{\parallel,c}} \right\}, \tag{6.28}$$

where $\beta_{\parallel,c}$ is the parallel plasma beta for the proton core, and $w_{\parallel,c} = \sqrt{2T_{\parallel,c}/m_p}$ the parallel thermal velocity, and a set of 6 dimensionless parameters for each of the proton beam, alpha core, and alpha beam populations:

$$\mathcal{P}_j = \left\{ \frac{T_{\parallel,c}}{T_{\parallel,j}}, \frac{m_j}{m_p}, \frac{q_j}{q_p}, \frac{T_{\perp,j}}{T_{\parallel,j}}, \frac{n_j}{n_c}, \frac{dV_j}{V_{ac}} \right\}. \tag{6.29}$$

Here m_j, q_j and n_j represent the mass, charge, and number density of species j respectively, and dV_j/V_{ac} the drift speed of population j relative to the core, as a fraction of the *core* Alfvén speed:

$$V_{ac} = \frac{B}{\sqrt{4\pi m_p n_c}}. \tag{6.30}$$

Finally, we note that PLUME employs a signed frequency ω_r convention, with $\omega_r > 0$ denoting forward propagation (in the direction of **B**) and $\omega_r < 0$ backward propagation. In this convention, $k_\parallel$ is always positive. This is to be contrasted with the perhaps more familiar (in physics) convention of $\omega_r > 0$ always and the wave vector **k** defining the propagation direction. We also restrict our attention throughout to parallel propagating modes $\mathbf{k} \times \mathbf{B} = 0$, both because empirically one finds the modes to be parallel propagating (via minimum variance analysis) and the fact that the parallel modes are found to almost always have the highest growth rates.

6.4.2 Results

P1: LH Polarisation

P1 is characterised by the strong, continuous band of LH polarisation from X to Y Hz, and consists of 27 measurement points, meaning we have the results of 27 PLUME calculations. For completeness, in figure 6.5 we show a representative time-slice output from PLUME during this interval in its entirety. In discussion of subsequent intervals we will only focus on the pertinent parts of the PLUME output. As we are only focussing on parallel propagating modes, $k_\perp \rho_c$ is fixed to be a small value of 10^{-3}, ρ_c being the proton gyroradius. The top left grey plot in figure 6.5 shows the location of the modes (red dots) in complex frequency space in the long wavelength limit with $k_\parallel \rho_c = k_\perp \rho_c = 10^{-3}$. The four uppermost red dots are the forward and backward propagating Alfvén/Ion Cyclotron (A/IC) and Fast Magnetosonic/Whistler (FM/W) modes. The "Christmas-tree" like structure of the multitude of modes beneath these four are compressive modes with drastically reduced growth rates that do not play a significant role in the dynamics here. Thus, this shows the starting,

fluid-like conditions, after which $k_\parallel \rho_c$ is stepped through and $\mathcal{D}(\mathbf{k}, \omega; \mathcal{P})$ solved at each $k_\parallel \rho_c$ to build up ω_r and γ as functions of $k_\parallel \rho_c$. The four most unstable (largest γ) modes are numbered 1 through 4 based on their positions at this initial $k_\parallel \rho_c$ slice, and subsequently tracked through the calculation. The remaining seven plots in the top two rows of figure 6.5 show various 2D distributions of the dimensionless parameters in equations 6.28 and 6.29 for each ion species (grey dots), and the location of this particular time slice (dark red dot). The remaining four columns show mode information for the four most unstable modes identified in the top left plot as just described. From top to bottom, as functions of $k_\parallel \rho_c$, we have the dispersion relation ω_r, the individual contributions to the growth rate from each ion species γ_j, with the overall growth rate γ shown in black, and the mode polarisation in the proton core frame (as a proportion of LH and RH). The power in the compressive component E_z is also shown but is zero for all four modes as expected. This means that Landau damping plays no role here, as it necessarily couples to the parallel component of the electric field E_z, and only cyclotron damping is physically relevant. From the dispersion relations modes 1 and 4 are clearly seen to be the backward and forward propagating FM/W modes, and modes 3 and 2 the forward and backward propagating A/IC modes, respectively.

For this time slice (which is typical of all the PLUME results during interval P1) the forward propagating A/IC mode is seen to be linearly unstable, and is primarily driven unstable by the proton core. That is, the largest contribution to the positive growth rate comes from γ_c, and is confined to the range $0.3 \lesssim k_\parallel \rho_c \lesssim 0.6$. The effect of the proton beam, alpha core, and alpha beam populations over this $k_\parallel \rho_c$ range is to damp this mode somewhat - in figure 6.5 we can see the black line denoting overall growth rate γ is slightly beneath the γ_c curve, and this effect is typical during P1. From the plot of $T_{\perp,c}/T_{\parallel,c}$ vs $\beta_{\parallel,c}$ in figure 6.5, and the 6th panel in figure 6.2, we conclude that this mode is most likely being driven unstable by a proton-cyclotron instability in the proton core population. Mode 4, the forward propagating FM/W mode, is also predicted linearly unstable at this time, driven by the alpha beam (the orange $\gamma_{\alpha2}$ curve), albeit with a significantly lower growth rate than that of the A/IC mode. Again, this is typical for P1, with occasional positive contributions to the growth rate from the proton beam population as well. The median dimensionless maximum growth rate of the A/IC mode for the entirety of P1 is $\gamma_{\max}/|\omega_r| = 5.1 \times 10^{-2}$.

This is the output of the PLUME calculation, the question remains of course whether this tallies with the actual magnetic field polarisation signatures that we observe in figure 6.2. In order to test this, we need to: 1) Take the intrinsic proton frame polarisation of this A/IC mode and Doppler shift it to the spacecraft frame to deduce what the observed polarisation would be, as it is possible for Doppler shifts to induce sign changes in polarisation if the shifted frequency crosses through 0 [28], and 2) Doppler shift the real frequency $\omega_r^{\max}$ associated with the maximum growth rate to obtain the spacecraft frequency $\omega_{r,sc}^{\max}$ and compare it to the frequencies of the ion scale waves seen in the magnetic field measurements. We carry out both of these calculations in section 6.4.4, where we show that the Doppler shift does *not* change the sign of ω_r, that is the polarisation of these modes in the proton core frame will appear the same in the spacecraft frame. We therefore conclude that the LH
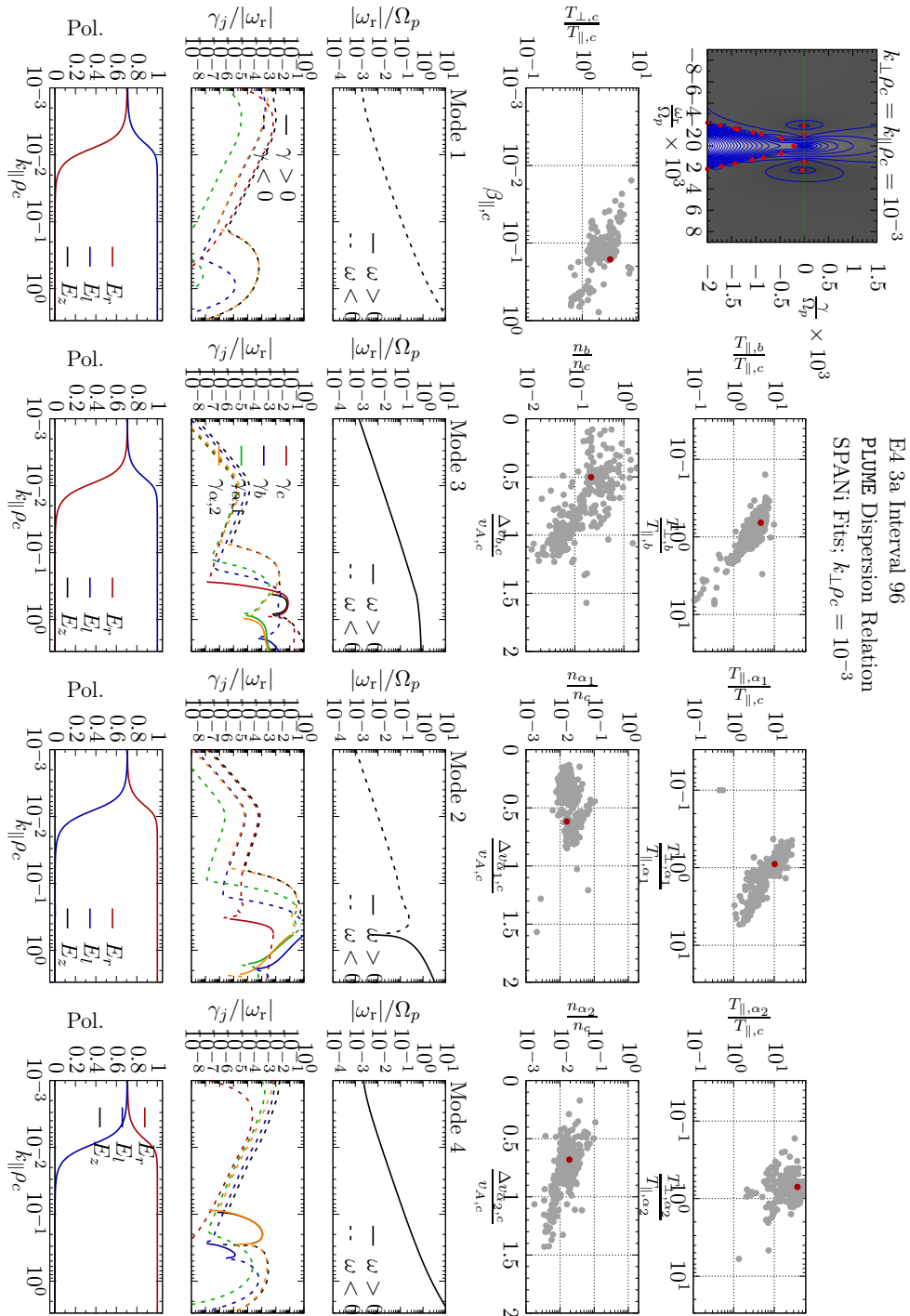
Figure 6.5: Full PLUME results for a time slice during interval P1, the period of LH polarisation.
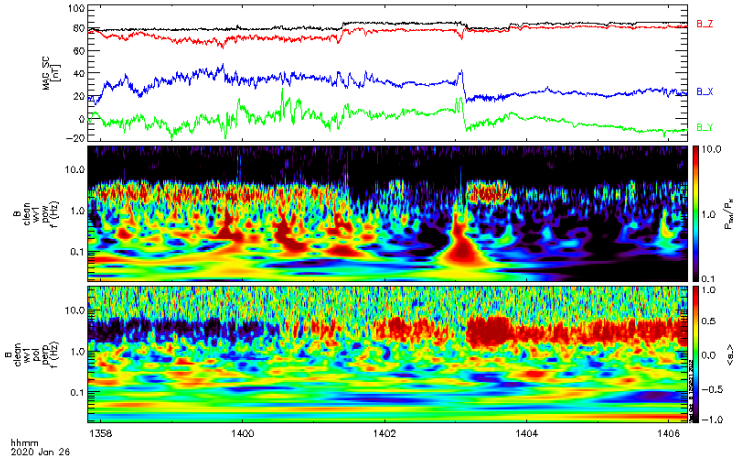
Figure 6.6: Zoomed in view of the P2 interval, showing the gap between LH and RH
polarisation.Top panel: magnetic field in spacecraft coordinates. Middle panel: Magnetic
field power. Bottom panel: Magnetic field perpendicular polarisation.

polarisation band observed during P1 is indeed due to an A/IC mode driven unstable by a
proton core temperature anisotropy.

P2: Gap Between LH and RH

A zoomed in view of interval P2, the short gap between the bands of LH and RH polarisation,
is shown in figure 6.6. From this, we can see that the LH signature in panel 3 has disappeared
completely, but there are still small measurable flecks of RH polarisation present. There is
also a fairly marked drop off in power in the frequency range of interest (panel 2). In P2
we have 4 SPAN-Ion fits and so 4 PLUME results to analyse. Each row of figure 6.7 shows
the ion component growth rates for both the A/IC mode and the FM/W mode for each of
these 4 time slices. Remarkably, we can see that the A/IC mode (first column) is no longer
unstable, coinciding exactly with the disappearance of LH polarisation! Comparing figure
6.7 to figure 6.5, the damping rates from the components other than the proton core are
all broadly similar, and it is a drastic reduction in the proton core growth rate γ_c that is
responsible for the mode becoming overall linearly stable. The right hand column shows the
proton core temperature anisotropy as a function of parallel core $\beta_{\parallel,c}$, and comparing this to
its equivalent plot in figure 6.5 (and the data in figure 6.2) it is clear there is a reduction in
the proton core anisotropy, supporting our interpretation in the previous section that this
mode is being driven unstable by a proton cyclotron instability. The middle column in figure
6.7 shows the growth rates for the FM/W mode, and similarly to the time slice in figure 6.5,
it is unstable, predominantly driven so by the alpha beam population.
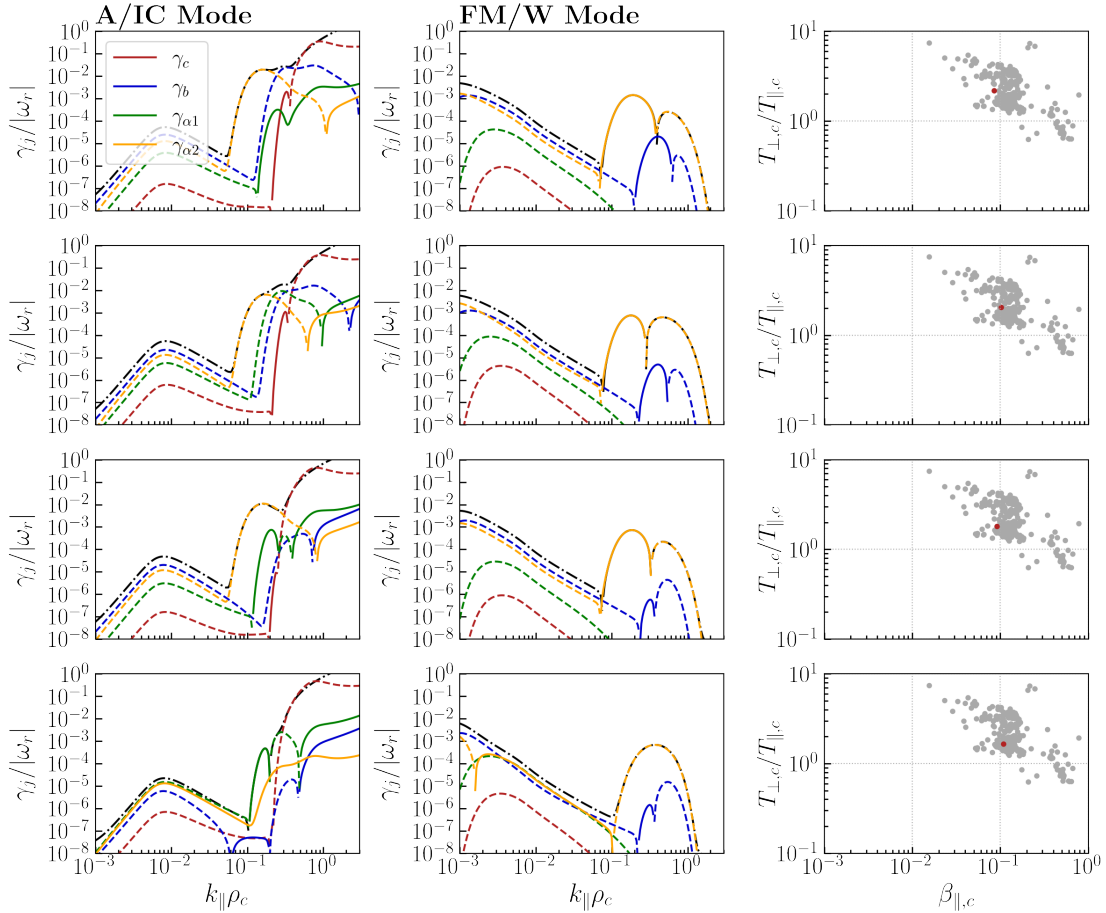
Figure 6.7: Contributions to the growth rates of the A/IC mode (left column) and FM/W mode (middle column) from each ion species (black dash-dotted lines are the overall growth rate). Each row represents a single time slice during P2. Proton core temperature anisotropies are shown in the right column, with data points from the full interval in grey, and red the measurement at each specific time. The A/IC mode is observed to be linearly stable, coinciding with the dropout in LH polarisation seen in figure 6.6.

P3: Initial Period of RH Polarisation

In contrast to P1 and P2 (and, as we shall see, P4), P3 is less straightforward to understand, and the agreements between the observations and the PLUME predictions are not as good. The PLUME results for maximum growth rate are of two types, shown in the top two rows of figure 6.8. In the first, the forward propagating A/IC mode is predicted to be linearly unstable with a higher growth rate than the FM/W mode, with the dominant positive contribution to γ coming from the alpha core component $\gamma_{\alpha 1}$ (green), in contrast to the proton core component during P1. In the second, the FM/W mode is unstable and the A/IC
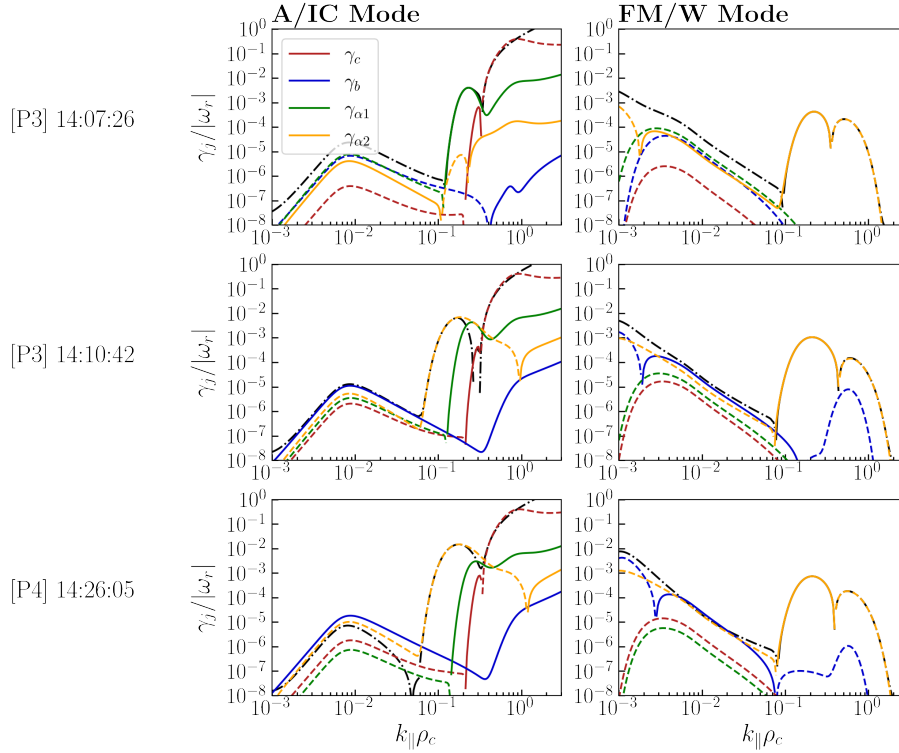
Figure 6.8: Example growth rates of the A/IC and FM/W modes during two different times in subinterval P3 (top two rows) and one time during P4 (bottom row). Times are shown on the left, showing how the A/IC mode in P3 is sometimes predicted to be driven unstable by the alpha core population (green), while at other times, and during P4, it is heavily damped by the alpha beam (orange).

mode stable, and is again being driven by the alpha beam component $\gamma_{\alpha 2}$. Of the 30 PLUME results in P3, 16 of them have $\gamma^{A/IC} > \gamma^{FM/W}$, and 13 of them have $\gamma^{FM/W} > \gamma^{A/IC}$. We would therefore expect to see a roughly equal mixture of LH and RH polarisations, which is clearly at odds with the purely red RH band we observe throughout. The median maximum growth rate of these A/IC modes is $\gamma^{A/IC}/|\omega_r| = 4.2 \times 10^{-3}$, lower than the corresponding growth rate in P1, and that of the FM/W modes is $\gamma^{FM/W}/|\omega_r| = 5.2 \times 10^{-4}$.

P4: Second Period of RH Polarisation

P4 is characterised by the abrupt disappearance of the very fast moving, tenuous alpha beam seen during P3, replaced by a slower moving, denser one ($V_{\alpha d} \sim 0.4 V_A$, $N_{\alpha b}/N \sim 0.5$). A representative plot of the A/IC and FM/W growth rates and their individual species contributions during P4 is shown in the third row of figure 6.8. As in the previous three
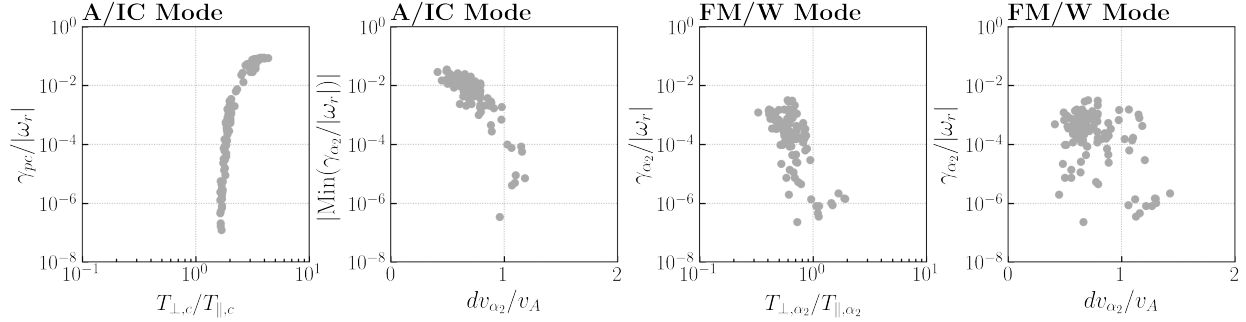
Figure 6.9: From left to right: Proton core contribution to the normalised growth rate of the A/IC mode vs proton core temperature anisotropy; damping rate of the alpha beam component on the A/IC mode as a function of alpha beam drift speed; alpha beam contribution γ_{α_2} to the FM/W mode vs the alpha beam temperature anisotropy; γ_{α_2} vs alpha beam drift speed.

sub-intervals the FM/W mode is being driven unstable by the alpha beam population. Of the 64 PLUME outputs in P4, 38 of them have $\gamma^{FM/W} > \gamma^{A/IC}$, and only 9 of them have $\gamma^{A/IC} > \gamma^{FM/W}$ (here γ implicitly means $\gamma_{\max}$). Thus, we would expect P4 to be majority RH polarised, which is in agreement with the observations. The median growth rate for the FM/W mode is $\gamma/|\omega_r| = 3.5 \times 10^{-4}$, and the median growth rate of the A/IC mode is $\gamma/|\omega_r| = 4.0 \times 10^{-3}$. We also point out that for the majority of times during P4 where the A/IC max growth rate is larger than the FM/W max growth rate, the range of $k_\parallel \rho_c$ over which the mode is unstable is exceedingly narrow. Given the sensitivity of the growth (and damping) rates on the plasma parameters, these could easily be spurious results ascribable to occasional sub-optimal fits.

We note that, although there is some tension between the observations and PLUME predictions during P3, in all cases it is the alphas - core and beam - that are playing the primary role in determining plasma stability here, and the proton contributions are subdominant. Alpha associated modes are also unstable at smaller wavevectors $k_\parallel \rho_c$, so regardless of polarisation we predict that the wave frequencies during the RH periods P3 and P4 are lower than those during the LH period P1, which we examine in the section 6.4.4.

6.4.3   Parameterisations

As discussed in the introduction, statistical studies of kinetic instabilities in the solar wind often focus on 2D histograms as functions of R_p and $\beta_\parallel$ ("Brazil plots"). This makes sense when only considering protons, but each new species adds several additional parameters to the system, bringing into question the validity of restricting to just these two variables. Indeed, one possible explanation of why the *oblique* instability thresholds seem to do a better

job of constraining the measurements [70, 13] despite the fact that empirically in case studies
the waves always seem to be parallel propagating could be the sensitivity of these Brazil plots
to other effects, such as additional species [58, 69], non-Maxwellian distribution functions
[139], or perhaps other things like departures from linear theory, etc. In reality, these systems
are high-dimensional (with correlations existing between different plasma parameters, for
instance beam drift speeds and beam density ratios (see e.g. figure 6.5 or figure 9 in [88])),
and overall stability may depend sensitively on many different quantities at once. Simple
parameterisations of instability thresholds, such as those in Brazil plots, are not a priori
expected to be attainable.

   Nevertheless, in figure 6.9 we show several different parameterisations of the A/IC and
FM/W mode growth rates (the data points are from P1 through P4). The first plot shows
the proton core normalised growth rate $\gamma_{pc}/|\omega_r|$ as a function of the proton core temperature
anisotropy, showing a remarkably clear positive correlation. Given that γ_{pc} is the species with
the highest positive contribution to the growth rate during P1, this confirms our interpreta-
tion above that the LH polarisation signatures we see are LH A/IC waves driven by a proton
core cyclotron instability. The second plot is the maximum *damping* rate on the A/IC mode
due to the alpha beam, showing a clear negative correlation; slower moving alpha beams
are responsible for greater damping of the forward propagating A/IC mode. The damping
rate of a particle species on a given wave mode will be proportional to the magnitude of
the pitch angle operator applied to the particle's VDF, evaluated at the resonant velocity
(see equation 9 for the growth rate γ in [86]). The very fast moving alpha beam during P3
does not sufficiently damp the forward propagating A/IC mode, producing the conflicting
prediction of the most dominant wave mode during this period. During P4, when the alpha
beam becomes slower and more dense, the A/IC mode is more heavily damped, allowing the
FM/W mode to dominate.

   The next two plots show the dependence of the alpha beam contribution $\gamma_{\alpha_2}/|\omega_r|$ to
the growth rate of the FM/W mode on the temperature anisotropy $T_{\perp,\alpha_2}/T_{\parallel,\alpha_2}$ and drift
speed dv_{α_2}/v_A. There is a negative correlation with the temperature anisotropy, but the
relation with the drift speed is much less obvious (if indeed there is one at all). One may
conclude that it is therefore a firehose instability $T_{\perp,\alpha_2}/T_{\parallel,\alpha_2} < 1$ responsible for driving the
RH wave mode being measured, as opposed to an alpha-proton drift instability, but this is in
some sense a semantic point. The parallel firehose instability and the ion/ion right handed
resonant instability can really be considered two limiting cases of one single instability, that
of a drifting beam that is allowed to be anisotropic. The *pure* parallel firehose instability
would be the case of $V_d = 0$ and $T_\perp/T_\parallel < 1$, while a pure ion/ion instability would have
$T_\perp/T_\parallel = 1$ and $V_d \neq 0$. Intuitively, this instability is simply due to an excess of parallel
pressure, which can be supplied by either a temperature anisotropy or a drift along the
magnetic field direction. This is made clear in [172] where the authors derive an expression
for the linear growth rate of the FM/W mode in the case where a single drifting alpha

population is non-isotropic; their expression for the sign of γ_α is given by

$$\text{sgn } \gamma_\alpha = \text{sgn} \left[\Omega_\alpha \left(\frac{T_{\parallel,\alpha}}{T_{\perp,\alpha}} - 1 \right) - \omega_r + k_\parallel V_{\alpha d} \right], \tag{6.31}$$

showing the two distinct contributions from the temperature anisotropy and drift speed to
the same wave mode.

6.4.4 Doppler Shift Calculation

Polarisation

In this section we perform the Doppler shift calculation of the proton frame frequencies and
intrinsic polarisations into the spacecraft frame, in order to compare the PLUME predictions
to the magnetic field observations. If $(\omega_r, \mathbf{k})$ are the real frequency and wave vector associated
with a given mode in the proton core frame, then the Doppler shifted frequency observed in
the spacecraft frame, ω_{sc}, is given by

$$\omega_{\text{sc}} = \omega_r + \mathbf{k} \cdot \mathbf{V}_{\text{sw}}, \tag{6.32}$$

where $\mathbf{V}_{\text{sw}}$ is the solar wind velocity (in this case the proton core velocity). For convenience of
the following discussion we use the $\omega_r > 0$ convention, with $\mathbf{k}$ denoting the direction of wave
propagation. From equation 6.32 we can see that since $\mathbf{V}_{\text{sw}}$ is always radially outwards,
waves that also propagate outwards are always shifted to higher frequencies $\omega_{\text{sc}} > \omega_r$, as
$\mathbf{k} \cdot \mathbf{V}_{\text{sw}} > 0$. The polarisation of such outward waves in the spacecraft frame is therefore the
same as it was in the proton core frame. For radially inward propagating waves, $\mathbf{k} \cdot \mathbf{V}_{\text{sw}} < 0$,
and there are two possibilities. The first is that the shift to lower frequencies $\omega_{\text{sc}} < \omega_r$ leaves
$\omega_{\text{sc}} > 0$. In this case the spacecraft frame polarisation again remains unchanged relative
to the proton frame polarisation. The second possibility is that the Doppler shift is large
enough to make $\omega_{\text{sc}} < 0$. These inwardly propagating waves will be measured to have the
opposite polarisation to their proton frame polarisation. In addition, since the spacecraft
measured frequency is a positive definite quantity, these waves will have a measured frequency
of $|\omega_{\text{sc}}| = -\omega_{\text{sc}}$ in the spacecraft frame. For an in-depth discussion of these ambiguities and
their relation to in-situ observations, see [28].

Fortunately for us, the relevant modes as predicted by PLUME here are the *outward*
propagating A/IC and FM/W modes, which have proton frame polarisations of LH and
RH respectively. These modes are both Doppler shifted to higher frequencies, maintaining
their plasma frame polarisations in the spacecraft frame, with no possibility of a change in
sign of ω_{sc}. Thus, we instantly see that our interpretation of the wave event as being an
A/IC mode during P1, the disappearance of the A/IC mode during P2, and predominantly
an FM/W mode during P3 and P4, predicts a change from LH polarisation during P1, to
no LH polarisation in P2, to RH polarisation during P3 and P4, which is exactly what we
observe!
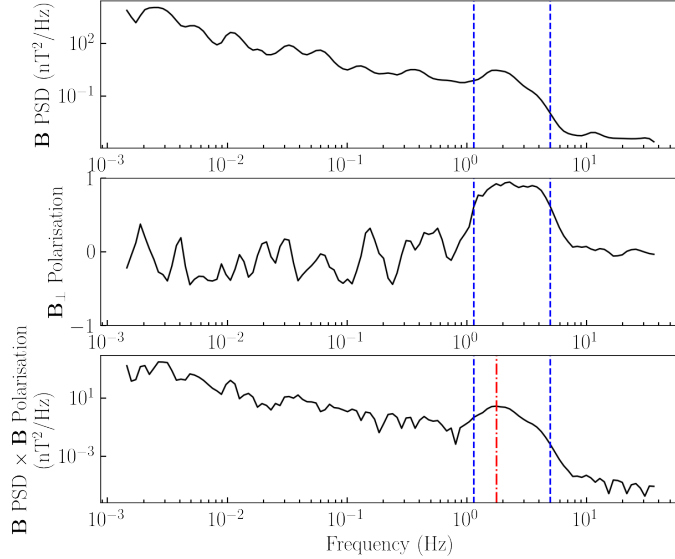
Figure 6.10: Example illustrating how an estimated frequency for the ion scale wave is
extracted from the magnetic field measurements. Top panel shows magnetic field trace power
spectral density, middle panel the perpendicular polarisation, and the product of the two is
shown in the bottom panel. Wave frequency is then estimated to be the local maximum in
the bottom panel. Blue dashed lines indicate the range over which polarisation is greater
than 0.5.

Predicted Frequencies

For a given unstable mode, we can make a prediction of its observed frequency by finding
the $(\omega_r, k_\parallel)$ that correspond to its maximum growth rate γ^{max}, and substituting these into
equation 6.32. Since we are restricting the calculation to parallel propagation $\mathbf{k} \times \mathbf{B} = 0$,
$\mathbf{k} \cdot \mathbf{V}_{\mathrm{sw}} = k_\parallel \hat{\mathbf{b}} \cdot \mathbf{V}_{\mathrm{sw}}$. (We note here that performing a minimum variance analysis during
this interval gives a very small median value of $\theta_{kb} \approx 4°$ away from parallel, which in
turn provides some upper and lower bounds on the predicted Doppler shifted frequencies
ω_{sc}. These error bars are very small however, only $\approx 2\%$, confirming our approximation in
section 6.4 of restricting to parallel propagation only.) There are several ways of estimating
the associated "central frequency" of the bands of polarisation in $\mathbf{B}_\perp$ in order to make a
comparison between the PLUME output and the observations. A simple method is shown
in figure 6.10, which shows an example of the magnetic field trace power spectrum (top),
magnetic field perpendicular polarisation (middle), and the product of these two quantities
(bottom), as functions of frequency, averaged over an interval of ≈ 29 s (this particular
interval was during P4). The bump in the power spectrum around 2 Hz is the excess coherent
wave power representing the presence of the ion-scale wave. The vertical dashed lines show
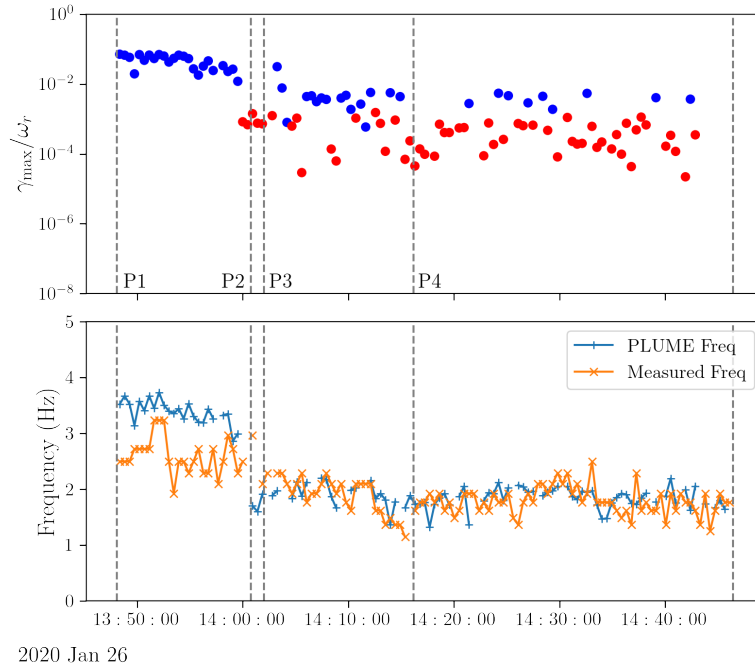
Figure 6.11: Top panel: Maximum growth rates of the predicted unstable modes and their spacecraft frame polarisations (blue = LH, red = RH), as a function of time. Vertical lines indicate the 4 sub-intervals. Bottom panel: Comparison between the PLUME predicted frequencies Doppler shifted into the spacecraft frame, and those derived from the magnetic field measurements using the method outlined in figure 6.10.

the frequency range over which the absolute value of the magnetic field polarisation is greater than 0.5, which we use as our cutoff for a polarisation signature being present. The central frequency is then estimated as the frequency corresponding to the maximum of the power spectrum multiplied by the polarisation, shown in the bottom panel marked by the dash-dotted red line. This method therefore makes use of both observational features available to us, the magnetic field power and polarisation.

The comparison between the PLUME predicted frequencies and the observed frequencies are shown in the bottom panel of figure 6.11 as a function of time, where we have taken the A/IC mode as the predominant mode during P1, and the FM/W mode for the remainder of the interval. (The constancy of the measured frequencies at the start of the LH interval is due to the frequency quantisation.)

The agreement between the predicted and observed frequencies is remarkably good, with a difference of $\lesssim 1$ Hz during the LH period, and the two time series lying essentially on top

of each other during the RH interval. Although the agreement is less good during the LH
interval, the fact that the decrease in wave frequency between the LH and RH intervals is
clearly reflected in the PLUME output further supports our interpretation of the LH and RH
waves as being proton and alpha associated modes respectively. By eye one could perhaps say
that the small modulations in observed frequency during the RH period are being observed
in the PLUME output as well, but it's difficult to make such an assertion having only looked
at one example wave event.

6.5 Summary

1. In this chapter we have studied an ion scale wave event from PSP's E4, characterised
   by a strong, prolonged period of LH polarisation lasting $\sim$ 15 minutes, followed by
   a very abrupt change (taking place over 2 minutes) to RH polarisation, lasting $\sim$ 45
   minutes.

2. The overall macroscopic fluid parameters of the protons and alpha particles do not
   change significantly during the event, but the substructures of the VDFs do, showing
   rearrangement of thermal energy between beam and core populations. The plasma is
   found to be overall stable to the long wavelength mirror and firehose instabilities.

3. From considering SPAN-Ion VDF measurements, the plasma was modelled as bi-
   Maxwellian proton core, proton beam, alpha core, and alpha beam populations (with
   an electron background for charge neutrality). PLUME [90] was used to solve the warm
   plasma dispersion relation for the four most unstable modes at each time throughout
   the wave event.

4. The LH polarised waves were identified as forward propagating (radially outwards)
   A/IC waves, driven by a proton cyclotron instability in the proton core population,
   with median growth rate $\gamma/|\omega_r| = 5.1 \times 10^{-2}$.

5. The RH polarised waves were identified as forward propagating (radially outwards)
   FM/W waves, predominantly driven by a parallel firehose instability in the alpha
   beam population, with median growth rate $\gamma/|\omega_r| = 3.5 \times 10^{-4}$.

6. The abrupt change from LH to RH polarisation was caused by a decrease in the proton
   core temperature anisotropy, drastically reducing the growth rate of the A/IC mode,
   allowing the formerly sub-dominant alpha beam driven FM/W mode to dominate.

7. The dropout in any LH polarisation signature during the very short interval between
   LH and RH polarisation corresponded to the plasma becoming instantaneously stable
   to the LH A/IC mode.

8. Doppler shifting the frequencies of the PLUME predicted most unstable modes to the spacecraft frame showed excellent agreement with magnetic field measurements, with $\lesssim 1$ Hz difference during the LH period and $\lesssim 0.5$ Hz during the RH period.

9. The predicted spacecraft frame polarisations also agree very well, with the only discrepancies occurring during the initial period of RH polarisation, where both the LH A/IC and RH FM/W modes are predicted to be the most unstable mode roughly half the time each.

10. The alpha beam population was observed to heavily damp the forward propagating A/IC mode, with higher damping at lower drift speeds.

11. The extremely good correspondence between predicted wave mode properties (via particle data) and the observed wave signatures in the magnetic field data strongly suggest we are measuring instantaneously unstable plasma locally generating ion-scale waves.

12. This chapter is not only the first case study to show in-situ evidence of a minor ion species driving ion-scale waves locally, but also the first to consider a drifting *secondary* alpha population as the source of free energy for driving such waves, and for showing that the alpha beam is indeed playing a significant role in the wave particle dynamics.

Chapter 7

Conclusions and Further Work

In this chapter we summarise the conclusions from Chapters 2 through 6, put them in context with recent results and outline potential avenues for future investigation.

In Chapter 2 we gave a summary of electrostatic analysers and the operation of the SPAN-Ion instrument. We also gave an account of intrinsic moment uncertainties, and a discussion of SPAN-Ion's finite FOV. In terms of future work, further investigation of the field alignment of the measured VDFs is probably the most pressing issue, with a view towards understanding the small ϕ offset we observed during an "ideal" measurement interval and whether or not this can be reduced using the method outlined in section 2.4. We also note that there are myriad available SPAN-Ion data products that have yet to receive much research attention; archive (high time cadence) data, targeted sweeps, higher mass products, and counts in the backward facing anodes all undoubtedly hold valuable scientific data. An effort should be made to make these data products as user-friendly as possible and available to the community.

In Chapter 3 we reproduced a paper we published in the PSP initial results special issue. Wavelet representations of the MHD invariants σ_c and σ_r were used to probe the ion-scale fluctuations from a day's worth of data during PSP's E1. Values of σ_c and σ_r typical to (slow) Alfvénic wind were observed, except for a population of negative σ_c that appeared at higher frequencies. By separating out our results as a function of θ_{Bv} we observed that negative values of σ_c were occurring during switchbacks, implying that they were local folds in the magnetic field and that the Alfvénic fluctuations were travelling "backwards" during these times. This also had implications for future studies of inner heliosphere turbulence using PSP data, as these sign-flipped values of σ_c might spuriously reduce average values if not properly taken into account.

In Chapter 4 we continued our analysis of the properties and geometry of switchbacks, this time being able to use SPAN-Ion proton and alpha measurements, having developed both the moment and fitting routines in the interim. These fitting routines, particularly to the alpha SF01 channel spectra, were a necessary prerequisite, as in order to get good measurements of the alpha particle density and abundance the contaminant protons in the

SF01 channel needed to be accounted for (despite being a small fraction of the total proton density they do represent a very sizable density *relative* to the alphas). In addition, that part of the alpha VDF truncated by SPAN's finite FOV needed to be "filled in" by fitting.

Our main result was showing that there were no consistent changes in alpha abundance inside switchbacks compared to outside, and that this didn't change when separating the switchbacks according to $V_{\alpha p}/V_W$, the ratio of the alpha-proton drift to the local wave speed. At first glance this might seem to be evidence in favour of in situ based switchback generation mechanisms over coronal processes. However, as we argue in the paper, if switchbacks were generated deep in the corona by interchange reconnection events that introduce compositional differences, such signatures would most likely not persist to be able to be observed at PSP. This is because the Alfvén speed at the speculated heights of these interchange reconnection events is very high ($\sim$ 1000 km/s), much higher than the alpha-proton drift speed is ever expected to be. Thus, the alphas would never be able to travel fast enough to carry this compositional signature outwards, being much slower than any Alfvénic fluctuations launched up the open field lines. In addition, even if they were somehow able to travel at the same speed as the switchbacks, their scale size requires many tens of Alfvén crossing times before reaching PSP, meaning any abundance difference would most likely have decayed away so as to be unobservable. Thus, while alpha abundance was in some sense a "tempting" quantity to study in relation to switchbacks, our work showed that it could not in the end be used to distinguish between different theorised generation mechanisms. There is a chance that this could change in the future, as PSP's projected closest approach to the Sun is $9.8R_S$, significantly closer to some postulated high-altitude generation mechanisms [189] than the $35R_s$ E3 data used in Chapter 4. However, a picture now seems to be emerging in the literature pointing more towards low coronal origins of switchbacks.

Evidence from later encounters increasingly pointed to a link between the "patch-like" occurrence of switchbacks and the angular scale of supergranules [10, 45]. [10] argued that the modulations in solar wind speed, alpha abundance and magnetic field intensity within the patches were PSP observing funnel-like spatial structures that originated from superexpanded wind at the edge of the convection cell boundaries. Convection within the supergranule drags the photospheric field to its boundary, bunching it up and causing interchange reconnection events that produce the switchbacks, as well as resulting in an asymmetry in the leading edge of the patch profile (as has clearly been seen in the PSP data). Other intriguing observational clues in the data were the striking power law extensions of the thermal proton and alpha distribution functions. These extended up to and above the top of the SPAN-Ion energy range and were able to be observed by the ISOIS Epi-Lo instrument. Together, we have worked on expending the ideas in [10] in [12] (in prep), where corroborating particle-in-cell simulations of the interchange reconnection events reproduce 1) the leading edge asymmetry in the patches, 2) the high energy suprathermal tails/power laws seen in the VDFs, and 3) a highly bursty radial wind profile, the individual bursts of which may correspond to the individual switchbacks themselves. Matching up the observed SPAN-Ion VDF energy spectra to the simulation spectra allows for an order of magnitude estimate of the Alfvén speed at the reconnection site, and hence the magnetic energy available for

heating the surrounding plasma. This is shown to be comparable to the energy flux required to accelerate high speed coronal hole wind [7]. More ambitiously then, this may not only explain the origin of switchbacks and the patch-like microstructure of fast wind streams, but confirm previous theories by tying the energy released by these interchange reconnection events to that required to heat and sustain a Parker type fast wind [133].

The second half of Chapter 4 was concerned with the 3D velocity fluctuations of both the protons and alpha particles during switchbacks. We showed that the Alfvénic motion of both species could be understood as rigid arm rotation about a fixed point in velocity space - the wave frame (showing that switchbacks can be well approximated as single, large amplitude spherically polarised Alfvén waves). By fitting spheres to the proton and alpha velocities, we can make two, independent estimates of the location of the wave frame using particle measurements alone. This was shown to agree very well with the usual method of estimating the wave frame, computation of the de Hoffmann-Teller velocity via minimisation of the motional electric field (which requires knowledge of the magnetic field), and we gave a geometric argument for why the two methods must agree. Using three case studies we showed that while switchbacks are always associated with positive increases in proton radial velocity (the "jets" of [73]), alpha radial velocities may be positive, negative, or stay the same, depending on the relative position of the alphas to the protons and wave frame velocity (encoded by the relative magnitudes of V_{pw} and $V_{\alpha p}$, the wave frame speed relative to the protons and the alpha proton drift speed).

This can be considered a direct extension of work first published in 1995 [62], showing that alpha particles can move in phase and out of phase with proton fluctuations, and the geometric picture of rotations in velocity space developed in [116, 115]. It also ties in nicely with a recent renewal of interest in the DHT frame, for instance using it as the frame of reference from which to analyse the non-linear interaction terms in MHD turbulence [25], or more generally its emphasis as the "correct" solar wind frame of reference [125] (as opposed to the centre of mass fluid frame). Indeed, while the analysis in Chapter 4 worked very well in singling out the preferred frame of reference in the (essentially ideal) case of a single, large amplitude Alfvén wave, the typical solar wind will contain a multitude of waves of different wave vectors and amplitudes. The authors in [125] point out that DHT frame determinations using different particle species agree with each other in the aggregate, and that equation 4.2 is therefore still a useful *definition* even if there is no single frame where the motional electric field becomes approximately zero. A natural extension of our work would be to include an analysis of the proton beam, which is expected to typically move in antiphase relative to the proton core, and to confirm more explicitly (as is highly suggested in figure 4.5) that the alphas and protons really do subtend the same angle during their oscillations, meaning that any mass dependence for their respective fluctuation amplitudes has dropped out, something which should be able to be derived analytically from the multi-fluid MHD equations [111].

In Chapter 5 we presented SPAN-Ion data from PSP's E3 with an emphasis on the measurement and characterisation of secondary alpha populations or "alpha beams". These features of alpha VDFs are rarely reported on and have not previously been systematically studied in the literature. We found that proton beams travelled at an average speed of $1.1V_A$

relative to the proton core, and carried an average density fraction of $\sim 20\%$, consistent with previous observations, in particular those of near-Sun slow Alfvénic wind measured by Helios [155]. Alpha beams, when they did occur, travelled more slowly, on average $0.7V_A$ relative to the alpha core, and carried a larger density fraction, $\sim 35\%$. Alpha beams carrying a relatively large density fraction is consistent with the few previously reported measurements in the literature.

Using a moving window Spearman's rank correlation coefficient with variable window size (essentially a wavelet transform) allowed us to show that there are time-localised periods of striking correlation between the proton and alpha normalised heat fluxes $q_{p\parallel}$ and $q_{\alpha\parallel}$. This strongly indicates that at least some of the time there is a common mechanism acting on both the proton and alpha VDFs producing the beam populations, a result that has not been observed or reported before, to our knowledge. In an attempt to see whether these time-localised correlations were spatially correlated as well, we used a PFSS model to trace the magnetic footpoints of PSP and plot variables as functions of Carrington longitude. The observed spatial structure was weak - periods of strong correlation between the two species' heat flux did not seem to correspond to the same longitudes, and neither did times of high proton heat flux. At face value this might seem to suggest that the relevant mechanisms affecting beam generation were taking place as the plasma travelled outwards. However, repeating this with the Helium abundance A_{He} also showed no evidence of spatial structure or periodicity! This was a rather surprising observation, given that Helium abundance is frozen in at the coronal base, and therefore perhaps the variable *most* expected to act as a source marker. We discussed some of the potential reasons for this result in section 5.5.5, and noted that it prevented us from concluding strongly in favour of local vs coronal beam generation or vice versa.

The potential avenues for future work concerning alpha (and proton) beams using SPAN-Ion measurements are numerous. Given the discussion above concerning switchback patches and their potential association with interchange reconnection events happening near supergranule boundaries, it would be interesting to investigate if there is any modulation in beam occurrence or magnitude coinciding with the patches. The reason to suspect a connection might exist is that interchange reconnection is one of the main theories of coronal based beam generation [49]. Any potential analysis is inherently made tricky because the large magnetic field deviations during switchbacks will result in the velocity space smearing discussed in section 2.4, and the beam becoming less well defined and harder to fit to. This necessitates using as high a measurement cadence as possible, which then becomes a trade off with worse counting statistics and poorer fits (especially in the alphas). Accordingly, this may be a perfect opportunity to apply the method in [113] to the SPAN-Ion data.

In Chapter 5 we only analysed data from one encounter; a natural thing to do is to compute fits for later encounters and examine the radial scalings of beam parameters. Of particular interest would be the radial evolution of the normalised heat fluxes (as is commonly done for electron heat flux [151, 66]) as a way to tease out any signatures of in situ beam regeneration . Previous work has shown the independence of proton beam-core drift speed as a function of collisional age A_c [3] which can be interpreted as evidence of local wave-particle

interactions maintaining the beam and preventing it decaying via Coulomb collisions. It is an open question whether the same thing would be seen for alpha beams; however, since PSP uniformly samples very collisionally young wind, it's not clear we could make a direct comparison using PSP data as a function of A_c.

In Chapter 6 we presented a detailed case study of an ion scale "wave storm" [181], involving a very abrupt change in the magnetic polarisation from left-handed (LH) to right-handed (RH). By modelling the ions as bi-Maxwellians for the proton core, proton beam, alpha core, and alpha beam, and performing an instability analysis, we identified with a high degree of certainty that the LH waves were outward propagating A/IC waves, driven by a proton cyclotron instability in the proton core population. The RH waves were identified as outward propagating FM/W waves, driven by a parallel firehose instability in the alpha beam population.

The occurrence of these wave storms and their nature has been elucidated at 1AU [76, 78, 77, 59, 181, 184], and PSP has confirmed their ubiquity in the inner heliosphere [168, 28, 27]. Our study constitutes the first direct measurement of a minor ion species actively taking part in one of these wave events, and also the first to model an alpha beam component as being relevant to the dynamics and the source of free energy driving the waves unstable. The success of this case study and the degree of agreement between the purely particle based predictions and the magnetic field fluctuations is a testament to the quality of the SPAN-Ion measurements, and going forward will allow us to further study wave-particle interaction events such as these in unprecedented detail, as well as answer broader questions about the processes that regulate the the form of ion VDFs in the expanding solar wind. Studies of the more general properties of these wave storms in the inner heliosphere using the wealth of PSP data collected so far have not yet been thoroughly carried out. Speculatively, one potential avenue for further work stems from the discussion in Chapter 6 that simple binary instability thresholds become harder to conceptualise when dealing with so many different particle populations and free plasma parameters. The set of plasma parameters (and $\mathbf{k}$) can be viewed as inputs to a scalar function that spits out a single number denoting "stable" or "unstable" (in practice this would be the growth rate for a particular mode), and such a problem is ideally suited to a machine learning approach. The idea would be to identify which variables are the most important, and then being able to predict system stability just by inputting plasma parameters, without doing the extensive calculations involved in solving the warm plasma dispersion relation. In addition, instabilities such as these, that decelerate the alpha particles relative to the protons, have been shown to significantly contribute to the net heating of the solar wind in the inner heliosphere [173], and the alpha particles constitute an important part of the solar wind's energy budget. Previous studies of this were limited to Helios measurements and radial distances greater than 0.3AU. Carrying out similar analyses for $r < 0.3$ AU using PSP data should be considered a high priority area of future work.

Bibliography

[1]   Paul S Addison. *The illustrated wavelet transform handbook: introductory theory and applications in science, engineering, medicine and finance.* CRC press, 2017.

[2]   OV Agapitov et al. "Sunward-propagating Whistler Waves Collocated with Localized Magnetic Field Holes in the Solar Wind: Parker Solar Probe Observations at 35.7 R Radii". In: *The Astrophysical journal letters* 891.1 (2020), p. L20.

[3]   BL Alterman et al. "A comparison of alpha particle and proton beam differential flows in collisionally young solar wind". In: *The Astrophysical Journal* 864.2 (2018), p. 112.

[4]   JR Asbridge, SJ Bame, and WC Feldman. "Abundance differences in solar wind double streams". In: *Solar Physics* 37.2 (1974), pp. 451–467.

[5]   Markus Aschwanden. *Physics of the solar corona: an introduction with problems and solutions.* Springer Science & Business Media, 2006. Chap. 9.

[6]   HF Astudillo et al. "Evidence for nongyrotropic alpha particle and proton distribution functions: TAUS solar wind measurements". In: *Journal of Geophysical Research: Space Physics* 101.A11 (1996), pp. 24423–24432.

[7]   WI Axford and JF McKenzie. "The origin of high speed solar wind streams". In: *Solar Wind Seven.* Elsevier, 1992, pp. 1–5.

[8]   Samuel T Badman et al. "Magnetic connectivity of the ecliptic plane within 0.5 au: Potential field source surface modeling of the first Parker Solar Probe encounter". In: *The Astrophysical Journal Supplement Series* 246.2 (2020), p. 23.

[9]   Badman, Samuel T. et al. "Measurement of the open magnetic flux in the inner heliosphere down to 0.13 AU". In: *A&A* 650 (2021), A18. DOI: 10.1051/0004-6361/202039407. URL: https://doi.org/10.1051/0004-6361/202039407.

[10]   SD Bale et al. "A Solar Source of Alfvénic Magnetic Field Switchbacks: In Situ Remnants of Magnetic Funnels on Supergranulation Scales". In: *The Astrophysical Journal* 923.2 (2021), p. 174.

[11]   SD Bale et al. "Highly structured slow solar wind emerging from an equatorial coronal hole". In: *Nature* 576.7786 (2019), pp. 237–242.

[12] SD Bale et al. "Interchange reconnection within coronal holes powers the solar wind". In: *Nature, In Prep* (2022).

[13] SD Bale et al. "Magnetic fluctuation power near proton temperature anisotropy instability thresholds in the solar wind". In: *Physical review letters* 103.21 (2009), p. 211101.

[14] SD Bale et al. "The FIELDS instrument suite for solar probe plus". In: *Space science reviews* 204.1 (2016), pp. 49–82.

[15] A Balogh et al. "Heliospheric magnetic field polarity inversions at high heliographic latitudes". In: *Geophysical research letters* 26.6 (1999), pp. 631–634.

[16] SJ Bame et al. "The Ulysses solar wind plasma experiment". In: *Astronomy and Astrophysics Supplement Series* 92 (1992), pp. 237–265.

[17] Riddhi Bandyopadhyay et al. "Interplay of turbulence and proton-microinstability growth in space plasmas". In: *Physics of Plasmas* 29.10 (2022), p. 102107.

[18] Aaron Barnes and Joseph V Hollweg. "Large-amplitude hydromagnetic waves". In: *Journal of Geophysical Research* 79.16 (1974), pp. 2302–2318.

[19] B. Bavassano and R. Bruno. "On the distribution of energy versus Alfvénic correlation for polar wind fluctuations". In: *Annales Geophysicae* 24.11 (Nov. 2006), pp. 3179–3184. DOI: `10.5194/angeo-24-3179-2006`.

[20] B. Bavassano, E. Pietropaolo, and R. Bruno. "Cross-helicity and residual energy in solar wind turbulence: Radial evolution and latitudinal dependence in the region from 1 to 5 AU". In: 103.A4 (Apr. 1998), pp. 6521–6530. DOI: `10.1029/97JA03029`.

[21] Stanislav Boldyrev. "On the spectrum of magnetohydrodynamic turbulence". In: *The Astrophysical Journal Letters* 626.1 (2005), p. L37.

[22] Joseph E Borovsky. "Flux tube texture of the solar wind: Strands of the magnetic carpet at 1 AU?" In: *Journal of Geophysical Research: Space Physics* 113.A8 (2008).

[23] Joseph E Borovsky. "The plasma structure of coronal hole solar wind: Origins and evolution". In: *Journal of Geophysical Research: Space Physics* 121.6 (2016), pp. 5055–5087.

[24] Sofiane Bourouaine et al. "Limits on alpha particle temperature anisotropy and differential flow from kinetic instabilities: solar wind observations". In: *The Astrophysical Journal Letters* 777.1 (2013), p. L3.

[25] T Bowen et al. "Nonlinear Interactions in Spherically Polarized Alfvénic Turbulence, IN PREP". In: *The Astrophysical Journal* (2022).

[26] Trevor A Bowen et al. "Impact of Residual Energy on Solar Wind Turbulent Spectra". In: *The Astrophysical Journal* 865.1 (2018), p. 45.

[27] Trevor A Bowen et al. "Ion-scale electromagnetic waves in the inner heliosphere". In: *The Astrophysical Journal Supplement Series* 246.2 (2020), p. 66.

[28]   Trevor A Bowen et al. "The Electromagnetic Signature of Outward Propagating Ion-scale Waves". In: *The Astrophysical Journal* 899.1 (2020), p. 74.

[29]   R. Bruno et al. "Magnetically dominated structures as an important component of the solar wind turbulence". In: *Annales Geophysicae* 25.8 (Aug. 2007), pp. 1913–1927. DOI: 10.5194/angeo-25-1913-2007.

[30]   Roberto Bruno and Vincenzo Carbone. "The solar wind as a turbulence laboratory". In: *Living Reviews in Solar Physics* 2.1 (2005), p. 4.

[31]   Anthony W Case et al. "The solar probe cup on the Parker Solar Probe". In: *The Astrophysical Journal Supplement Series* 246.2 (2020), p. 43.

[32]   Benjamin D. G. Chandran and Jean C. Perez. "Reflection-driven magnetohydrodynamic turbulence in the solar atmosphere and solar wind". In: *Journal of Plasma Physics* 85.4, 905850409 (Aug. 2019), p. 905850409. DOI: 10.1017/S0022377819000540. arXiv: 1908.00880 [physics.space-ph].

[33]   Sydney Chapman and Harold Zirin. "Notes on the solar corona and the terrestrial ionosphere". In: *Smithsonian Contributions to Astrophysics* (1957).

[34]   CC Chaston et al. "MHD Mode Composition in the Inner Heliosphere from Parker Solar Probe's 1st Perihelion". In: *The Astrophysical Journal Supplement Series* 246 (2020).

[35]   CHK Chen et al. "Anisotropy of Alfvénic turbulence in the solar wind and numerical simulations". In: *Monthly Notices of the Royal Astronomical Society* 415.4 (2011), pp. 3219–3226.

[36]   CHK Chen et al. "Residual energy spectrum of solar wind turbulence". In: *The Astrophysical Journal* 770.2 (2013), p. 125.

[37]   Michael R Collier et al. "Neon-20, oxygen-16, and helium-4 densities, temperatures, and suprathermal tails in the solar wind determined with WIND/MASS". In: *Geophysical research letters* 23.10 (1996), pp. 1191–1194.

[38]   Steven R Cranmer. "Ion cyclotron wave dissipation in the solar corona: The summed effect of more than 2000 ion species". In: *The Astrophysical Journal* 532.2 (2000), p. 1197.

[39]   Steven R Cranmer, George B Field, and John L Kohl. "Spectroscopic constraints on models of ion cyclotron resonance heating in the polar solar corona and high-speed solar wind". In: *The Astrophysical Journal* 518.2 (1999), p. 937.

[40]   R D'Amicis et al. "Radial Evolution of Solar Wind Turbulence during Earth and Ulysses Alignment of 2007 August". In: *The Astrophysical Journal* 717.1 (2010), p. 474.

[41]   F De Hoffmann and E Teller. "Magneto-hydrodynamic shocks". In: *Physical Review* 80.4 (1950), p. 692.

[42] JF Drake et al. "Switchbacks as signatures of magnetic flux ropes generated by interchange reconnection in the corona". In: *Astronomy & Astrophysics* 650 (2021), A2.

[43] Tereza Ďurovcová, Jana Šafránková, and Zdeněk Němeček. "Proton Beam Abundance Variations and Their Relation to Alpha Particle Properties". In: *The Astrophysical Journal* 923.2 (2021), p. 170.

[44] Marie Farge. "Wavelet transforms and their applications to turbulence". In: *Annual review of fluid mechanics* 24.1 (1992), pp. 395–458.

[45] Naïs Fargette et al. "Characteristic scales of magnetic switchback patches near the Sun and their possible association with solar supergranulation and granulation". In: *The Astrophysical Journal* 919.2 (2021), p. 96.

[46] Andrew N Fazakerley, Steven J Schwartz, and Gotz Paschmann. "Measurement of plasma velocity distributions". In: *ISSI Scientific Reports Series* 1 (1998), pp. 91–124.

[47] WC Feldman et al. "Constraints on high-speed solar wind structure near its coronal base: a ULYSSES perspective." In: *Astronomy and Astrophysics* 316 (1996), pp. 355–367.

[48] WC Feldman et al. "Double ion streams in the solar wind". In: *Journal of Geophysical Research* 78.13 (1973), pp. 2017–2027.

[49] WC Feldman et al. "Evidence for ion jets in the high-speed solar wind". In: *Journal of Geophysical Research: Space Physics* 98.A4 (1993), pp. 5593–5605.

[50] AJ Finley et al. "The contribution of alpha particles to the solar wind angular momentum flux in the inner heliosphere". In: *Astronomy & Astrophysics* 650 (2021), A17.

[51] LA Fisk and G Gloeckler. "Acceleration and composition of solar wind suprathermal tails". In: *Space science reviews* 130.1 (2007), pp. 153–160.

[52] LA Fisk and JC Kasper. "Global circulation of the open magnetic flux of the Sun". In: *The Astrophysical Journal Letters* 894.1 (2020), p. L4.

[53] NJ Fox et al. "The solar probe plus mission: humanity's first visit to our star". In: *Space Science Reviews* 204.1 (2016), pp. 7–48.

[54] C Froment et al. "Direct evidence for magnetic reconnection at the boundaries of magnetic switchbacks with Parker Solar Probe". In: *Astronomy & Astrophysics* 650 (2021), A5.

[55] SA Fuselier et al. "Specularly reflected He2+ at high Mach number quasi-parallel shocks". In: *Journal of Geophysical Research: Space Physics* 95.A4 (1990), pp. 4319–4325.

[56] S Peter Gary and S Peter Gary. *Theory of space plasma microinstabilities*. 7. Cambridge university press, 1993.

[57] S Peter Gary et al. "Alpha/proton magnetosonic instability in the solar wind". In: *Journal of Geophysical Research: Space Physics* 105.A9 (2000), pp. 20989–20996.

[58] S Peter Gary et al. "Consequences of proton and alpha anisotropies in the solar wind: Hybrid simulations". In: *Journal of Geophysical Research: Space Physics* 108.A2 (2003).

[59] S Peter Gary et al. "Ion-driven instabilities in the solar wind: Wind observations of 19 March 2005". In: *Journal of Geophysical Research: Space Physics* 121.1 (2016), pp. 30–41.

[60] Karl-Heinz Glassmeier and Fritz M Neubauer. "Low-frequency electromagnetic plasma waves at comet P/Grigg-Skjellerup: Overview and spectral characteristics". In: *Journal of Geophysical Research: Space Physics* 98.A12 (1993), pp. 20921–20935.

[61] George Gloeckler. "Ubiquitous suprathermal tails on the solar wind and pickup ion distributions". In: *AIP Conference Proceedings*. Vol. 679. 1. American Institute of Physics. 2003, pp. 583–588.

[62] BE Goldstein, M Neugebauer, and EJ Smith. "Alfvén waves, alpha particles, and pickup ions in the solar wind". In: *Geophysical research letters* 22.23 (1995), pp. 3389–3392.

[63] Bruce E Goldstein et al. "Observed constraint on proton-proton relative velocities in the solar wind". In: *Geophysical research letters* 27.1 (2000), pp. 53–56.

[64] L Gomberoff, G Gnavi, and FT Gratton. "Minor heavy ion electromagnetic beam–plasma interactions in the solar wind". In: *Journal of Geophysical Research: Space Physics* 101.A6 (1996), pp. 13517–13522.

[65] CC Goodrich and AJ Lazarus. "Suprathermal protons in the interplanetary solar wind". In: *Journal of Geophysical Research* 81.16 (1976), pp. 2750–2754.

[66] J. S. Halekas et al. "Electron heat flux in the near-Sun environment". In: 650, A15 (June 2021), A15. DOI: 10.1051/0004-6361/202039256. arXiv: 2010.10302 [astro-ph.SR].

[67] CM Hammond et al. "Solar wind double ion beams and the heliospheric current sheet". In: *Journal of Geophysical Research: Space Physics* 100.A5 (1995), pp. 7881–7889.

[68] Petr Hellinger. "Comment on the linear mirror instability near the threshold". In: *Physics of plasmas* 14.8 (2007), p. 082105.

[69] Petr Hellinger and Pavel Trávníček. "Parallel and oblique proton fire hose instabilities in the presence of alpha/proton drift: Hybrid simulations". In: *Journal of Geophysical Research: Space Physics* 111.A1 (2006).

[70] Petr Hellinger et al. "Solar wind proton temperature anisotropy: Linear theory and WIND/SWE observations". In: *Geophysical research letters* 33.9 (2006).

[71]   Timothy S Horbury, Miriam Forman, and Sean Oughton. "Anisotropic scaling of mag-netohydrodynamic turbulence". In: *Physical Review Letters* 101.17 (2008), p. 175005.

[72]   Timothy S Horbury et al. "Sharp Alfvénic impulses in the near-Sun solar wind". In: *The Astrophysical Journal Supplement Series* 246.2 (2020), p. 45.

[73]   TS Horbury, L Matteini, and D Stansby. "Short, large-amplitude speed enhancements in the near-Sunfast solar wind". In: *Monthly Notices of the Royal Astronomical Society* 478.2 (2018), pp. 1980–1986.

[74]   Philip A Isenberg and Martin A Lee. "A dispersive analysis of bispherical pickup ion distributions". In: *Journal of Geophysical Research: Space Physics* 101.A5 (1996), pp. 11055–11066.

[75]   Philip A Isenberg, Martin A Lee, and Joseph V Hollweg. "The kinetic shell model of coronal heating and acceleration by ion cyclotron waves: 1. Outward propagating waves". In: *Journal of Geophysical Research: Space Physics* 106.A4 (2001), pp. 5649–5660.

[76]   Lan K Jian et al. "Ion cyclotron waves in the solar wind observed by STEREO near 1 AU". In: *The Astrophysical Journal* 701.2 (2009), p. L105.

[77]   LK Jian et al. "Electromagnetic waves near the proton cyclotron frequency: STEREO observations". In: *The Astrophysical Journal* 786.2 (2014), p. 123.

[78]   LK Jian et al. "Observations of ion cyclotron waves in the solar wind near 0.3 AU". In: *Journal of Geophysical Research: Space Physics* 115.A12 (2010).

[79]   AD Johnstone et al. "The Giotto three-dimensional positive ion analyser". In: *Journal of Physics E: Scientific Instruments* 20.6 (1987), p. 795.

[80]   SW Kahler, NU Crocker, and JT Gosling. "The topology of intrasector reversals of the interplanetary magnetic field". In: *Journal of Geophysical Research: Space Physics* 101.A11 (1996), pp. 24373–24382.

[81]   JT Karpen et al. "Reconnection-driven coronal-hole jets with gravity and solar wind". In: *The Astrophysical Journal* 834.1 (2017), p. 62.

[82]   Justin C Kasper, Alan J Lazarus, and S Peter Gary. "Wind/SWE observations of firehose constraint on solar wind proton temperature anisotropy". In: *Geophysical research letters* 29.17 (2002), pp. 20–1.

[83]   Justin C Kasper et al. "Alfvénic velocity spikes and rotational flows in the near-Sun solar wind". In: *Nature* 576.7786 (2019), pp. 228–231.

[84]   Justin C Kasper et al. "Solar wind electrons alphas and protons (SWEAP) investi-gation: Design of the solar wind and coronal plasma instrument suite for solar probe plus". In: *Space Science Reviews* 204.1 (2016), pp. 131–186.

[85]   Justin C Kasper et al. "Solar wind helium abundance as a function of speed and heliographic latitude: variation through a solar cycle". In: *The Astrophysical Journal* 660.1 (2007), p. 901.

[86] CF Kennel and HV Wong. "Resonant particle instabilities in a uniform magnetic field". In: *Journal of Plasma Physics* 1.1 (1967), pp. 75–80.

[87] Alexander V Khrabrov and Bengt UÖ Sonnerup. "deHoffmann-Teller analysis". In: *Analysis methods for multi-spacecraft data* 1 (1998), pp. 221–248.

[88] KG Klein et al. "Inferred Linear Stability of Parker Solar Probe Observations Using One-and Two-component Proton Distributions". In: *The Astrophysical Journal* 909.1 (2021), p. 7.

[89] Kristopher G Klein and Gregory G Howes. "Predicted impacts of proton temperature anisotropy on solar wind turbulence". In: *Physics of Plasmas* 22.3 (2015), p. 032903.

[90] Kristopher G Klein et al. "Applying Nyquist's method for stability determination to solar wind observations". In: *Journal of Geophysical Research: Space Physics* 122.10 (2017), pp. 9815–9823.

[91] Vladimir Krasnoselskikh et al. "Localized magnetic-field structures and their boundaries in the near-sun solar wind from parker solar probe measurements". In: *The Astrophysical Journal* 893.2 (2020), p. 93.

[92] Matthew W Kunz et al. "Inertial-range kinetic turbulence in pressure-anisotropic astrophysical plasmas". In: *Journal of Plasma Physics* 81.5 (2015).

[93] Ronan Laker et al. "Statistical analysis of orientation, shape, and size of solar wind switchbacks". In: *Astronomy & Astrophysics* 650 (2021), A1.

[94] J Martin Laming et al. "Element abundances: A new diagnostic for the solar wind". In: *The Astrophysical Journal* 879.2 (2019), p. 124.

[95] D Lario. "Estimation of the solar flare neutron worst-case fluxes and fluences for missions traveling close to the Sun". In: *Space Weather* 10.3 (2012).

[96] Larosa, A. et al. "Switchbacks: statistical properties and deviations from Alfvénicity". In: *A&A* 650 (2021), A3. DOI: 10.1051/0004-6361/202039442. URL: https://doi.org/10.1051/0004-6361/202039442.

[97] Benoit Lavraud et al. "Magnetic reconnection as a mechanism to produce multiple thermal proton populations and beams locally in the solar wind". In: *Astronomy & Astrophysics* 656 (2021), A37.

[98] Xing Li et al. "A kinetic Alfvén wave and the proton distribution function in the fast solar wind". In: *The Astrophysical Journal Letters* 719.2 (2010), p. L190.

[99] BR Lichtenstein and CP Sonett. "Dynamic magnetic structure of large amplitude Alfvénic variations in the solar wind". In: *Geophysical Research Letters* 7.3 (1980), pp. 189–192.

[100] RP Lin et al. "A three-dimensional plasma and energetic particle investigation for the Wind spacecraft". In: *Space Science Reviews* 71.1-4 (1995), pp. 125–153.

[101] Roberto Livi et al. "The Solar Probe ANalyzer -Ions on Parker Solar Probe". In: *Earth and Space Science Open Archive* (2021), p. 20. DOI: `10.1002/essoar.10508651.1`. URL: `https://doi.org/10.1002/essoar.10508651.1`.

[102] S Livi and E Marsch. "Generation of solar wind proton tails and double beams by Coulomb collisions". In: *Journal of Geophysical Research: Space Physics* 92.A7 (1987), pp. 7255–7261.

[103] Allan R Macneil et al. "The evolution of inverted magnetic fields through the inner heliosphere". In: *Monthly Notices of the Royal Astronomical Society* 494.3 (2020), pp. 3642–3655.

[104] Alfred Mallet and Alexander A Schekochihin. "A statistical model of three-dimensional anisotropy and intermittency in strong Alfvénic turbulence". In: *Monthly Notices of the Royal Astronomical Society* 466.4 (2016), pp. 3918–3927.

[105] Alfred Mallet et al. "Evolution of large-amplitude Alfvén waves and generation of switchbacks in the expanding solar wind". In: *The Astrophysical Journal* 918.2 (2021), p. 62.

[106] Yana G Maneva, Jaime A Araneda, and Eckart Marsch. "Parametrically Unstable Alfvén-cyclotron Waves and Wave–Particle Interactions in the Solar Corona and Solar Wind". In: *AIP Conference Proceedings*. Vol. 1121. 1. American Institute of Physics. 2009, pp. 122–126.

[107] E Marsch and S Livi. "Observational evidence for marginal stability of solar wind ion beams". In: *Journal of Geophysical Research: Space Physics* 92.A7 (1987), pp. 7263–7268.

[108] E Marsch et al. "Solar wind helium ions: Observations of the Helios solar probes between 0.3 and 1 AU". In: *Journal of Geophysical Research: Space Physics* 87.A1 (1982), pp. 35–51.

[109] E Marsch et al. "Solar wind protons: Three-dimensional velocity distributions and derived plasma parameters measured between 0.3 and 1 AU". In: *Journal of Geophysical Research: Space Physics* 87.A1 (1982), pp. 52–72.

[110] Eckart Marsch. "Kinetic physics of the solar corona and solar wind". In: *Living Reviews in Solar Physics* 3.1 (2006), pp. 1–100.

[111] Eckart Marsch and Daniel Verscharen. "On nonlinear Alfvén-cyclotron waves in multi-species plasma". In: *Journal of Plasma Physics* 77.3 (2011), pp. 385–403.

[112] Mihailo M Martinović et al. "Multiscale Solar Wind Turbulence Properties inside and near Switchbacks Measured by the Parker Solar Probe". In: *The Astrophysical Journal* 912.1 (2021), p. 28.

[113] BA Maruca and JC Kasper. "Improved interpretation of solar wind ion measurements via high-resolution magnetic field data". In: *Advances in Space Research* 52.4 (2013), pp. 723–731.

[114] Bennett A Maruca, Justin C Kasper, and S Peter Gary. "Instability-driven limits on helium temperature anisotropy in the solar wind: observations and linear Vlasov analysis". In: *The Astrophysical Journal* 748.2 (2012), p. 137.

[115] L Matteini et al. "Ion kinetic energy conservation and magnetic field strength constancy in multi-fluid solar wind Alfvénic turbulence". In: *The Astrophysical Journal* 802.1 (2015), p. 11.

[116] Lorenzo Matteini et al. "Dependence of solar wind speed on the local magnetic field orientation: Role of Alfvénic fluctuations". In: *Geophysical Research Letters* 41.2 (2014), pp. 259–265.

[117] Lorenzo Matteini et al. "Fire hose instability driven by alpha particle temperature anisotropy". In: *The astrophysical journal* 812.1 (2015), p. 13.

[118] Lorenzo Matteini et al. "Ion kinetics in the solar wind: Coupling global expansion to local microphysics". In: *Space science reviews* 172.1 (2012), pp. 373–396.

[119] Lorenzo Matteini et al. "Kinetics of parametric instabilities of Alfvén waves: Evolution of ion distribution functions". In: *Journal of Geophysical Research: Space Physics* 115.A9 (2010).

[120] DJ McComas et al. "Integrated Science Investigation of the Sun (ISIS): Design of the energetic particle investigation". In: *Space Science Reviews* 204.1 (2016), pp. 187–256.

[121] JP McFadden et al. "MAVEN suprathermal and thermal ion compostion (STATIC) instrument". In: *Space Science Reviews* 195.1 (2015), pp. 199–256.

[122] Michael D McManus et al. "Cross helicity reversals in magnetic switchbacks". In: *The Astrophysical Journal Supplement Series* 246.2 (2020), p. 67.

[123] Michael D McManus et al. "Density and Velocity Fluctuations of Alpha Particles in Magnetic Switchbacks". In: *The Astrophysical Journal* 933.1 (2022), p. 43.

[124] FS Mozer et al. "Switchbacks in the solar magnetic field: Their evolution, their content, and their effects on the plasma". In: *The Astrophysical Journal Supplement Series* 246.2 (2020), p. 68.

[125] Zdeněk Němeček et al. "What is the solar wind frame of reference?" In: *The Astrophysical Journal* 889.2 (2020), p. 163.

[126] M Neugebauer et al. "Spatial structure of the solar wind and comparisons with solar data and models". In: *Journal of Geophysical Research: Space Physics* 103.A7 (1998), pp. 14587–14599.

[127] M Neugebauer et al. "Ulysses observations of differential alpha-proton streaming in the solar wind". In: *Journal of Geophysical Research: Space Physics* 101.A8 (1996), pp. 17047–17055.

[128] M Neugebauer et al. "Ulysses observations of microstreams in the solar wind from coronal holes". In: *Journal of Geophysical Research: Space Physics* 100.A12 (1995), pp. 23389–23395.

[129] Marcia Neugebauer and Bruce E Goldstein. "Double-proton beams and magnetic switchbacks in the solar wind". In: *AIP Conference Proceedings*. Vol. 1539. 1. American Institute of Physics. 2013, pp. 46–49.

[130] Leon Ofman et al. "Modeling ion beams, kinetic instabilities, and waves observed by the Parker Solar Probe near perihelia". In: *The Astrophysical Journal* 926.2 (2022), p. 185.

[131] KW Ogilvie et al. "SWE, a comprehensive plasma instrument for the Wind spacecraft". In: *Space Science Reviews* 71.1 (1995), pp. 55–77.

[132] EN Parker. "Dynamical theory of the solar wind". In: *Space Science Reviews* 4.5 (1965), pp. 666–708.

[133] Eugene N Parker. "Dynamics of the interplanetary gas and magnetic fields." In: *The Astrophysical Journal* 128 (1958), p. 664.

[134] Clare E Parnell and Ineke De Moortel. "A contemporary view of coronal heating". In: *Philosophical Transactions of the Royal Society A: Mathematical, Physical and Engineering Sciences* 370.1970 (2012), pp. 3217–3240.

[135] G Paschmann and SJ Schwartz. "ISSI book on analysis methods for multi-spacecraft data". In: *Cluster-II workshop multiscale/multipoint plasma measurements*. Vol. 449. 2000, p. 99.

[136] Jean Carlos Perez and Benjamin DG Chandran. "Direct numerical simulations of reflection-driven, reduced magnetohydrodynamic turbulence from the sun to the Alfvén critical point". In: *The Astrophysical Journal* 776.2 (2013), p. 124.

[137] TD Phan et al. "Parker Solar Probe observations of solar wind energetic proton beams produced by magnetic reconnection in the near-Sun heliospheric current sheet". In: *Geophysical Research Letters* (2022), e2021GL096986.

[138] TD Phan et al. "Prevalence of magnetic reconnection in the near-Sun heliospheric current sheet". In: *Astronomy & Astrophysics* 650 (2021), A13.

[139] V Pierrard and M Lazar. "Kappa distributions: theory and applications in space plasmas". In: *Solar physics* 267.1 (2010), pp. 153–174.

[140] Viviane Pierrard and Yuriy Voitenko. "Velocity Distributions and Proton Beam Production in the Solar Wind". In: *AIP Conference Proceedings*. Vol. 1216. 1. American Institute of Physics. 2010, pp. 102–105.

[141] V Pizzo et al. "Determination of the solar wind angular momentum flux from the HELIOS data-an observational test of the Weber and Davis theory". In: *The Astrophysical Journal* 271 (1983), pp. 335–354.

[142] JJ Podesta. "Dependence of solar-wind power spectra on the direction of the local mean magnetic field". In: *The Astrophysical Journal* 698.2 (2009), p. 986.

[143] Cara E Rakowski and J Martin Laming. "On the origin of the slow speed solar wind: helium abundance variations". In: *The Astrophysical Journal* 754.1 (2012), p. 65.

[144] Pete Riley et al. "Properties of arc-polarized Alfvén waves in the ecliptic plane: Ulysses observations". In: *Journal of Geophysical Research: Space Physics* 101.A9 (1996), pp. 19987–19993.

[145] François Rincon and Michel Rieutord. "The Sun's supergranulation". In: *Living Reviews in Solar Physics* 15.1 (2018), pp. 1–74.

[146] DA Roberts et al. "The nature and evolution of magnetohydrodynamic fluctuations in the solar wind: Voyager observations". In: *Journal of Geophysical Research: Space Physics* 92.A10 (1987), pp. 11021–11040.

[147] Orlando Romeo et al. "Characterization of Strahl Electron Scattering in the Solar Wind Observed by PSP". In: *AGU Fall Meeting 2021*. AGU. 2021.

[148] H Rosenbauer et al. "A survey on initial results of the Helios plasma experiment". In: *Journal of Geophysics Zeitschrift Geophysik* 42.6 (1977), pp. 561–580.

[149] D Ruffolo et al. "Shear-driven transition to Isotropically turbulent solar wind outside the Alfvén critical zone". In: *The Astrophysical Journal* 902.2 (2020), p. 94.

[150] NA Schwadron and DJ McComas. "Switchbacks Explained: Super-Parker Fields—The Other Side of the Sub-Parker Spiral". In: *The Astrophysical Journal* 909.1 (2021), p. 95.

[151] Earl E Scime et al. "Regulation of the solar wind electron heat flux from 1 to 5 AU: Ulysses observations". In: *Journal of Geophysical Research: Space Physics* 99.A12 (1994), pp. 23401–23410.

[152] Munehito Shoda, Benjamin DG Chandran, and Steven R Cranmer. "Turbulent generation of magnetic switchbacks in the Alfvénic solar wind". In: *The Astrophysical Journal* 915.1 (2021), p. 52.

[153] Jonathan Squire, Benjamin DG Chandran, and Romain Meyrand. "In-situ switchback formation in the expanding solar wind". In: *The Astrophysical Journal Letters* 891.1 (2020), p. L2.

[154] D Stansby et al. "Alpha particle thermodynamics in the inner heliosphere fast solar wind". In: *Astronomy & Astrophysics* 623 (2019), p. L2.

[155] D Stansby et al. "The origin of slow Alfvénic solar wind at solar minimum". In: *Monthly Notices of the Royal Astronomical Society* 492.1 (2020), pp. 39–44.

[156] JT Steinberg et al. "Differential flow between solar wind protons and alpha particles: First WIND observations". In: *Geophysical research letters* 23.10 (1996), pp. 1183–1186.

[157] Thomas H Stix. *Waves in plasmas*. Springer Science & Business Media, 1992.

[158] D Telloni, E Antonucci, and Maria Adele Dodero. "Outflow velocity of the O+ 5 ions in polar coronal holes out to 5 R". In: *Astronomy & Astrophysics* 472.1 (2007), pp. 299–307.

[159] Anna Tenerani et al. "Evolution of switchbacks in the inner Heliosphere". In: *The Astrophysical Journal Letters* 919.2 (2021), p. L31.

[160] Anna Tenerani et al. "Magnetic field kinks and folds in the solar wind". In: *The Astrophysical Journal Supplement Series* 246.2 (2020), p. 32.

[161] KM Thieme, E Marsch, and R Schwenn. "Spatial structures in high-speed streams as signatures of fine structures in coronal holes." In: *Annales Geophysicae*. Vol. 8. 1990, pp. 713–723.

[162] C Torrence and GP Compo. *A practical guide to wavelet analysis, B. Am. Meteorol. Soc., 79, 61–78.* 1998.

[163] BT Tsurutani et al. "The relationship between interplanetary discontinuities and Alfvén waves: Ulysses observations". In: *Geophysical Research Letters* 21.21 (1994), pp. 2267–2270.

[164] C-Y Tu, E Marsch, and Z-R Qin. "Dependence of the proton beam drift velocity on the proton core plasma beta in the solar wind". In: *Journal of Geophysical Research: Space Physics* 109.A5 (2004).

[165] Vadim M Uritsky et al. "Reconnection-driven Magnetohydrodynamic Turbulence in a Simulated Coronal-hole Jet". In: *The Astrophysical Journal* 837.2 (2017), p. 123.

[166] Vytenis M Vasyliunas. "12. Deep space plasma measurements". In: *Methods in Experimental Physics*. Vol. 9. Elsevier, 1971, pp. 49–88.

[167] Marco Velli, Roland Grappin, and André Mangeney. "Turbulent cascade of incompressible unidirectional Alfvén waves in the interplanetary medium". In: *Physical Review Letters* 63.17 (1989), p. 1807.

[168] JL Verniero et al. "Parker Solar Probe observations of proton beams simultaneous with ion-scale waves". In: *The Astrophysical Journal Supplement Series* 248.1 (2020), p. 5.

[169] JL Verniero et al. "Strong Perpendicular Velocity-space Diffusion in Proton Beams Observed by Parker Solar Probe". In: *The Astrophysical Journal* 924.2 (2022), p. 112.

[170] Daniel Verscharen, Sofiane Bourouaine, and Benjamin DG Chandran. "Instabilities driven by the drift and temperature anisotropy of alpha particles in the solar wind". In: *The Astrophysical Journal* 773.2 (2013), p. 163.

[171] Daniel Verscharen and Benjamin DG Chandran. "The dispersion relations and instability thresholds of oblique plasma modes in the presence of an ion beam". In: *The Astrophysical Journal* 764.1 (2013), p. 88.

[172] Daniel Verscharen et al. "A parallel-propagating Alfvénic ion-beam instability in the high-beta solar wind". In: *The Astrophysical Journal* 773.1 (2013), p. 8.

[173] Daniel Verscharen et al. "Deceleration of alpha particles in the solar wind by instabilities and the rotational force: implications for heating, azimuthal flow, and the Parker spiral magnetic field". In: *The Astrophysical Journal* 806.2 (2015), p. 157.

[174] Y Voitenko and Viviane Pierrard. "Generation of proton beams by non-uniform solar wind turbulence". In: *Solar Physics* 290.4 (2015), pp. 1231–1241.

[175] Angelos Vourlidas et al. "The wide-field imager for Solar Probe Plus (WISPR)". In: *Space Science Reviews* 204.1 (2016), pp. 83–130.

[176] Y-M Wang. "Relating the solar wind helium abundance to the coronal magnetic field". In: *The Astrophysical Journal* 683.1 (2008), p. 499.

[177] Edmund J Weber and Leverett Davis Jr. "The angular momentum of the solar wind". In: *The Astrophysical Journal* 148 (1967), pp. 217–227.

[178] P. Whittlesey et al. "Strahl Tracers of Inner Heliosphere Frequent Switchbacks: Early results from the SPAN-Electron Analyzers on Parker Solar Probe". In: *The Astrophysical Journal* In prep (2019b).

[179] Phyllis L Whittlesey et al. "The Solar Probe ANalyzers—electrons on the parker solar probe". In: *The Astrophysical Journal Supplement Series* 246.2 (2020), p. 74.

[180] Robert T Wicks et al. "Correlations at large scales and the onset of turbulence in the fast solar wind". In: *The Astrophysical Journal* 778.2 (2013), p. 177.

[181] RT Wicks et al. "A proton-cyclotron wave storm generated by unstable proton distribution functions in the solar wind". In: *The Astrophysical Journal* 819.1 (2016), p. 6.

[182] Thierry Dudok de Wit et al. "Switchbacks in the near-Sun magnetic field: long memory and impact on the turbulence cascade". In: *The Astrophysical Journal Supplement Series* 246.2 (2020), p. 39.

[183] LD Woodham et al. "Enhanced proton parallel temperature inside patches of switchbacks in the inner heliosphere". In: *Astronomy & Astrophysics* 650 (2021), p. L1.

[184] Lloyd D Woodham et al. "Parallel-propagating fluctuations at proton-kinetic scales in the solar wind are dominated by kinetic instabilities". In: *The Astrophysical Journal Letters* 884.2 (2019), p. L53.

[185] Thomas Woolley et al. "Plasma properties, switchback patches, and low α-particle abundance in slow Alfvénic coronal hole wind at 0.13 au". In: *Monthly Notices of the Royal Astronomical Society* 508.1 (2021), pp. 236–244.

[186] Thomas Woolley et al. "Proton core behaviour inside magnetic field switchbacks". In: *Monthly Notices of the Royal Astronomical Society* 498.4 (2020), pp. 5524–5531.

[187] Martin Wüest, David S Evans, and Rudolf von Steiger. *Calibration of particle instruments in space physics.* InternationaI Space Science Institute, 2007.

[188] Yohei Yamauchi et al. "Differential velocity between solar wind protons and alpha particles in pressure balance structures". In: *Journal of Geophysical Research (Space Physics)* 109.A3, A03104 (Mar. 2004), A03104. DOI: 10.1029/2003JA010274.

[189]   GP Zank et al. "The Origin of Switchbacks in the Solar Corona: Linear Theory". In: *The Astrophysical Journal* 903.1 (2020), p. 1.

[190]   L-L Zhao et al. "Identiication of Magnetic Flux Ropes from Parker Solar Probe Observations during the First Encounter". In: *The Astrophysical Journal Supplement Series* 246.2 (2020), p. 26.

[191]   Jack B Zirker. "Coronal heating". In: *Solar physics* 148.1 (1993), pp. 43–60.